



# Final Technical Report: Manufacturing and Additive Design of Electric Machines by 3D Printing (MADE3D)

Latha Sethuraman,<sup>1</sup> Parans Paranthaman,<sup>2</sup> Michael Halbig,<sup>3</sup> Mrityunjay Singh,<sup>4</sup> and Zachary Tuchfield<sup>5</sup>

*1 National Renewable Energy Laboratory*

*2 Oak Ridge National Laboratory*

*3 NASA Glenn Research Center*

*4 Ohio Aerospace Institute*

*5 Universities Space Research Association at NASA Glenn Research Center*

**NREL is a national laboratory of the U.S. Department of Energy  
Office of Energy Efficiency & Renewable Energy  
Operated by the Alliance for Sustainable Energy, LLC**

This report is available at no cost from the National Renewable Energy Laboratory (NREL) at [www.nrel.gov/publications](http://www.nrel.gov/publications).

Contract No. DE-AC36-08GO28308

**Technical Report**  
NREL/TP-5000-90537  
December 2024



# Final Technical Report: Manufacturing and Additive Design of Electric Machines by 3D Printing (MADE3D)

Latha Sethuraman,<sup>1</sup> Parans Paranthaman,<sup>2</sup> Michael Halbig,<sup>3</sup> Mrityunjay Singh,<sup>4</sup> and Zachary Tuchfield<sup>5</sup>

*1 National Renewable Energy Laboratory*

*2 Oak Ridge National Laboratory*

*3 NASA Glenn Research Center*

*4 Ohio Aerospace Institute*

*5 Universities Space Research Association at NASA Glenn Research Center*

## **Suggested Citation**

Sethuraman, Latha, Parans Paranthaman, Michael Halbig, Mrityunjay Singh, and Zachary Tuchfield. 2024. *Final Technical Report: Manufacturing and Additive Design of Electric Machines by 3D Printing (MADE3D)*. Golden, CO: National Renewable Energy Laboratory. NREL/TP-5000-90537. <https://nrel.gov/docs/fy25osti/90537.pdf>.

**NREL is a national laboratory of the U.S. Department of Energy  
Office of Energy Efficiency & Renewable Energy  
Operated by the Alliance for Sustainable Energy, LLC**

This report is available at no cost from the National Renewable Energy Laboratory (NREL) at [www.nrel.gov/publications](http://www.nrel.gov/publications).

Contract No. DE-AC36-08GO28308

**Technical Report**  
NREL/TP-5000-90537  
December 2024

National Renewable Energy Laboratory  
15013 Denver West Parkway  
Golden, CO 80401  
303-275-3000 • [www.nrel.gov](http://www.nrel.gov)

## NOTICE

This work was authored in part by the National Renewable Energy Laboratory, operated by Alliance for Sustainable Energy, LLC, for the U.S. Department of Energy (DOE) under Contract No. DE-AC36-08GO28308. Funding provided by U.S. Department of Energy Office of Energy Efficiency and Renewable Energy Wind Energy Technologies Office. The views expressed herein do not necessarily represent the views of the DOE or the U.S. Government.

This report is available at no cost from the National Renewable Energy Laboratory (NREL) at [www.nrel.gov/publications](http://www.nrel.gov/publications).

U.S. Department of Energy (DOE) reports produced after 1991 and a growing number of pre-1991 documents are available free via [www.OSTI.gov](http://www.OSTI.gov).

*Cover Photos by Dennis Schroeder: (clockwise, left to right) NREL 51934, NREL 45897, NREL 42160, NREL 45891, NREL 48097, NREL 46526.*

NREL prints on paper that contains recycled content.

## Acknowledgments

This material is based on work supported by the U.S. Department of Energy's Office of Energy Efficiency and Renewable Energy Wind Energy Technologies Office Fiscal Year 2019 Laboratory Call Program.

Many people contributed to the work in various capacities, including supporting the modeling and analysis efforts, reviewing results and providing feedback, troubleshooting software, developing codes and machine-learning algorithm toolsets and data sampling techniques, printing samples, and characterizing printed materials. The team gratefully acknowledges the contributions from the following members and organizations:

- National Renewable Energy Laboratory:
  - Latha Sethuraman
  - Ganesh Vijayakumar
  - Jonathan Keller
  - DiLea Bindel
  - Andrew Glaws
  - Lee Jay Fingersh
  - Miles Skinner
  - Hannes Labuschagne
  - Dane Randel
  - Rory Andrykowski
  
- Oak Ridge National Laboratory:
  - Parans Paranthaman
  - Tej Lamichhane
  - Willie Kemp
  - Haobo Wang
  - Kaustubh Mungale
  - Uday Vaidya
  - Brian Sales
  - Brian Post
  - Amy Elliott
  - Fred List
  
- NASA Glenn Research Center:

- Michael Halbig
  - Mrityunjay Singh
  - Zachary Tuchfield
- Bergey Windpower Co.:
  - Tod Hanley
  - Mike Bergey
- ALTAIR:
  - Lavanya Vadamodala
- Carpenter Technology Corporation:
  - Chins Chinnasamy
- Arnold Magnetic Technologies:
  - Aaron Williams
- Beehive Industries:
  - Jonaaron Jones
  - Patrick Cole
- Additive Drives:
  - Rick Ottolinger
  - Martin Bezuindehout
- Tumaker:
  - Toni Iborra
- Industry:
  - Jonas Carlsson
  - Alksandr Sedov

## List of Acronyms

2D	two-dimensional
3D	three-dimensional
BAAM	big area additive manufacturing
BJAT	binder jetting additive technology
CAD	computer-aided design
DIW	direct ink writing
EDM	electrical discharge machining
FEA	finite element analysis
FFF	fused filament fabrication
HEC	hydroxyethyl cellulose
HREE	heavy rare earth element
IACS	International Annealed Copper Standard
IEA	International Energy Agency
kW	kilowatt
LPBF	laser powder bed fusion
MADE3D	Manufacturing and Additive Design of Electric Machines by 3D Printing
MADE3D-AML™	MADE3D-Advanced Machine Learning™s
MDF	Manufacturing Demonstration Facility
MW	megawatt
NASA Glenn	National Aeronautics and Space Administration Glenn Research Center
NGO	non-grain-oriented
NOES	non-grain-oriented electrical steel
NREL	National Renewable Energy Laboratory
OEM	original equipment manufacturer
ORNL	Oak Ridge National Laboratory
REE	rare earth element
SEM	scanning electron microscopy
SLM	selective laser melting
TRL	technology readiness level

## Executive Summary

The U.S. clean energy transition hinges on the growth of the offshore wind energy sector. Therefore, offshore wind energy is expected to be a major driver for innovations in manufacturing, materials, and design to enable robust and cost-competitive wind turbines. The race to build larger and taller turbines rated 10 megawatts and beyond has intensified pressure on original equipment manufacturers in terms of the logistics of handling and transporting large wind turbine components, securing critical raw materials, and scaling up necessary domestic production infrastructure to meet the demand. There is increased interest in building lightweight, more efficient, and high-power dense drivetrains that will ease the burden on installation, minimize the raw material demand, and increase the ability to source materials domestically. Despite good efficiency and reliability, existing drivetrain technologies such as direct-drive permanent magnet generators are heavy (>300 tons) and expensive and often rely on large quantities of rare earth permanent magnets, steel, and copper. Existing design and manufacturing techniques for lightweighting are time-intensive, resulting in complex topologies that are difficult to manufacture and generate wasted material. As a result, substantial design and manufacturing innovations are needed to improve their scalability.

Manufacturing and Additive Design of Electric Machines by 3D Printing (MADE3D) is a project led by the National Renewable Energy Laboratory in partnership with Oak Ridge National Laboratory and NASA Glenn Research Center aimed at advancing next-generation lightweight wind turbine generators with the potential to reduce demand for critical materials by more than 25% and enable such designs by multimaterial additive manufacturing. As part of the project, the team developed new capabilities to design and manufacture every component of the generator, including magnetic core packs and permanent magnets with reduced rare earth content. We designed and built electrical conductors with insulation and structural and mechanical components in collaboration with a small wind turbine original equipment manufacturer, Bergey Windpower Co. Specifically:

- The National Renewable Energy Laboratory led the development of new electric machine design toolsets (topology optimization and shape optimization techniques) for the multimaterial design of magnets, electrical steel core, and conductors used in radial flux permanent magnet synchronous generators. The design methods and toolsets were used in design space exploration for lightweighting a 15-megawatt direct-drive generator and a 15-kilowatt commercial wind turbine generator.
- The Oak Ridge National Laboratory investigated the feasibility of Fe<sub>3</sub>Si and Fe<sub>6</sub>Si steel as candidate materials for electrical steel laminate and rotor by selective laser melting. A new insert molding technique was developed by extrusion-based printing processes for multimaterial printing of polymer-bonded composite magnets made from SmFeN and dysprosium-free NdFeB magnets with electrical steel.
- NASA Glenn researchers advanced a direct ink writing approach for multimaterial printing of both the electrical conductors and insulation to achieve a fill factor of more than 70% that is beneficial for achieving high power densities.

We anticipate that the design tools and manufacturing processes developed through the MADE3D project will provide new opportunities to reduce the demand for critical materials used in next-generation offshore wind turbine generators, alleviate pressures on the supply chain,

create domestic manufacturing infrastructure that will eliminate multiple manufacturing processes, and reduce production time and waste by exploring novel optimized generator designs enabled via 3D printing. The following list of publications, patents, and trademarks were acquired as part of this project:

## Publications

Sethuraman, L., A. Glaws, M. Skinner, and M. Parans Paranthaman. 2024. “Advanced Multimaterial Shape Optimization Methods as Applied to Advanced Manufacturing of Wind Turbine Generators.” *Wind Energy* 27(8): 767–796. <https://doi.org/10.1002/we.2911>.

Sethuraman, L., A. Glaws, M. Skinner, and M. P. Paranthaman. 2023. “Advanced Permanent Magnet Generator Topologies Using Multimaterial Shape Optimization and 3D Printing.” Presented at the 12th International Conference on Power Electronics, Machines and Drives (PEMD 2023), Brussels, Belgium, Oct. 26, 2023. <https://doi.org/10.1049/icp.2023.2041>.

Sethuraman, L., A. Glaws, M. Skinner, and P. Paranthaman. 2023. “Advanced Permanent Magnet Generator Topologies Using Multimaterial Shape Optimization and 3D Printing.” Golden, CO: National Renewable Energy Laboratory. NREL/PR-5000-87649. <https://www.nrel.gov/docs/fy24osti/87649.pdf>.

Labuschagne, C. J. J., L. Sethuraman, T. Hanley, M. P. Paranthaman, and L. J. Fingersh. 2023. “An Assessment of Additively Manufactured Bonded Permanent Magnets for a Distributed Wind Generator.” Presented at the 2023 IEEE International Electric Machines & Drives Conference (IEMDC), San Francisco, CA, May 15–18, 2023. <https://doi.org/10.1109/IEMDC55163.2023.10238895>.

Sethuraman, L., and G. Vijayakumar. 2022. “A New Shape Optimization Approach for Lightweighting Electric Machines Inspired by Additive Manufacturing.” Presented at the 2022 Joint MMM-Intermag Conference (INTERMAG), New Orleans, LA, Jan. 10–14, 2022. <https://doi.org/10.1109/INTERMAG39746.2022.9827714>.

Wang, H., T.N. Lamichhane, and M. P. Paranthaman. 2022. “Review of Additive Manufacturing of Permanent Magnets for Electrical Machines: A Prospective on Wind Turbine.” *Materials Today Physics* 24: 100675. <https://doi.org/10.1016/j.mtphys.2022.100675>.

Sethuraman, L., G. Vijayakumar, S. Ananthan, M. P. Paranthaman, J. Keller, and R. King. 2021. “MADE3D: Enabling the Next Generation of High-Torque Density Wind Generators by Additive Design and 3D Printing.” *Forsch Ingenieurwes* 85: 287–311. <https://doi.org/10.1007/s10010-021-00465-y>.

## Patents and Trademarks

- SWR-20-70 for MADE3D-AML™ has been asserted a software copyright.
- U.S. Patent No. 11,993,834, Issued: May 28, 2024, “INDIRECT ADDITIVE MANUFACTURING PROCESS FOR FABRICATING BONDED SOFT MAGNETS”
- M. P. Paranthaman and W. Kemp, “Novel method to fabricate a wind generator rotor can,” Invention Disclosure: 202305349, submitted on April 17, 2023.



# Table of Contents

<b>Executive Summary</b> .....	<b>vi</b>
<b>1 Introduction</b> .....	<b>1</b>
1.1 Limitations in Generator Design .....	2
1.2 Limitations in Materials .....	3
1.3 Limitations in Assembly and Manufacturing .....	4
1.4 Metal Additive Manufacturing .....	6
1.5 The MADE3D™ Project .....	9
1.6 Approach .....	9
1.6.1 Advanced Design Tools for Additive Manufacturing .....	12
1.6.2 Advanced Materials and Multimaterial Manufacturing Processes .....	13
1.6.3 Gaps and Risk Assessment in Scaling .....	15
1.6.4 Future R&D Needs .....	16
<b>2 Advanced Design Optimization for Additive Manufacturing</b> .....	<b>18</b>
2.1 Advanced Design Tools for Topology Optimization Using a Grid-Based Approach .....	18
2.1.1 Optimization Goals and Materials .....	21
2.1.2 Opportunities .....	23
2.1.3 Challenges .....	23
2.2 Development of a Grid-Free Optimization Approach .....	27
2.2.1 Bézier Curves for Shape Optimization .....	27
2.2.2 Opportunities .....	30
2.3 Design Space Exploration in a Commercial Direct-Drive Generator .....	30
2.3.1 15-kW Bergey Generator and MADE3D Targets .....	32
2.3.2 Design of Experiments Using Alternative Magnet Topologies .....	36
2.3.3 Exploring Optimization Opportunities With Printed Magnets and Shaping .....	41
2.3.4 Structural Integrity and Optimization of Rotor .....	55
2.3.5 Summary .....	56
<b>3 Advanced Processes for Multimaterial Printing of Soft and Hard Magnets and Stator Conductors</b> .....	<b>58</b>
3.1 Candidate Materials for Printing Soft Magnets and Performance Characterization .....	58
3.1.1 Fabrication of Proof-of-Concept Prototype Stator Laminates Using Fe <sub>3</sub> Si and Performance Characterization .....	60
3.1.2 Evaluation of Multimaterial Printing of Fe <sub>3</sub> Si Steel With Secondary Alloys .....	63
3.1.3 Fabrication of a Proof-of-Concept Prototype Rotor Can .....	65
3.1.4 Candidate Materials for Hard Magnets Chosen for Feasibility Study .....	66
3.1.5 Post-Magnetic Grain Alignment of Printed Magnets .....	68
3.1.6 Overmolding of Printed Magnets With Electrical Steel for a Proof-of-Concept Rotor .....	69
3.1.7 Multimaterial Printing of Stator Conductors With Insulation .....	71
3.1.8 Proof-of-Concept Prototype Conductor Printing for Bergey’s Stator Tooth .....	82
3.1.9 Summary .....	84
<b>4 Gap Analysis and Future Work</b> .....	<b>86</b>
4.1 Multimaterial Design for Wind Turbine Generators and Designing for Printability .....	86
4.1.1 Opportunities for Designs in Wind Turbines .....	86
4.1.2 Scalability of Optimized Designs .....	87
4.1.3 Gaps .....	88
4.2 Materials .....	90
4.2.1 Hard Magnet Material .....	91
4.2.2 3D Printed Electrical Conductors .....	91
4.2.3 Soft Magnet Materials .....	92
4.3 Lab-Scale Printing Demonstrations Versus State-of-the-Art Industrial 3D Printers and R&D .....	

Needs	92
4.3.1	Challenges With Scaling Lab-Scale Printing Processes for Large Generator Manufacturing ..... 93
4.3.2	The Potential for Stator Lamination Manufacturing and Rotor Core Manufacturing Using Commercial LPBF Systems..... 95
4.3.3	Using Large Commercial Cold Spray Additive Technology for Printing Both 15-kW and 15-MW Electrical Steel Cores..... 96
4.3.4	Indirect Additive Manufacturing of Rotor Core..... 97
4.3.5	Magnet Manufacturing Using Commercial FFF Printers..... 97
4.3.6	The Potential for Printing Electrical Conductors Using Commercial Printers..... 100
4.4	Multimaterial Printing and Printing Costs..... 105
4.5	Future Work ..... 108
4.5.1	Advancing Design, Materials, and Additive Manufacturing for Wind Turbine Generators ..... 108
<b>References</b>	<b>114</b>

## List of Figures

Figure 1. Volume of minerals estimated for direct-drive generators rated 15 MW and beyond .....	2
Figure 2. Winding process in a synchronous wind turbine generator.....	5
Figure 3. Magnets in an outer rotor direct-drive permanent-magnet synchronous wind turbine generator..	5
Figure 4. Research gaps and needs for next-generation wind turbine generators.....	6
Figure 5. MADE3D project approach.....	10
Figure 6. Design optimization approach.....	13
Figure 7. Approach to gap and risk assessment.....	15
Figure 8. Optimization approaches: (a) baseline pole, (b) grid-based topology optimization, (c) boundary optimization .....	18
Figure 9. Flux density contour in the 15-MW generator for rated operating conditions by transient magnetic FEA .....	19
Figure 10. Mesh definitions: (a) outer grid for geometric control of material distribution, and (b) inner mesh with FEA elements. Every rotor element in the outer grid is discretized by four triangular elements, and every magnet element in the outer grid is discretized by two triangular elements. These finite elements assume the property of the material that is assigned to each element in the outer grid (either air, or material).....	20
Figure 11. Topology optimization using surrogate models .....	21
Figure 12. Examples of rotor core designs that were infeasible .....	23
Figure 13. A few additional single-material and multimaterial designs identified using MADE3D-AML™ .....	26
Figure 14. Parameterization approaches: (a) circular boundaries and (b) Bézier curves.....	28
Figure 15. Framework and capabilities of MADE3D-AML™ software .....	29
Figure 16. Comparison of optimized rotor core patterns using grid-based approach and Bézier curve approach.....	30
Figure 17. 15-kW Bergey generator designed for Bergey’s Excel turbine.....	31
Figure 18. Turbine speed-power curves at various wind speeds .....	33
Figure 19. Bergey’s test setup of their 15-kW generator .....	33
Figure 20. A 2D model of a one-tenth sector of the 15-kW Bergey generator.....	34
Figure 21. Comparison of model predictions versus measurements.....	35
Figure 22. Decoupled multiphysics modeling .....	38
Figure 23. Results from design of experiments: (a) Crown-shaped designs and (b) V-shaped designs .....	38
Figure 24. Demagnetization curves of printed magnet.....	42
Figure 25. Different parameterization approaches for the pole .....	43
Figure 26. Sensitivities of generator performance to stator core mass .....	44
Figure 27. Optimized asymmetric pole design .....	46
Figure 28. Conductor shaping leveraging additive manufacturing: (a) Polygon layers and (b) Z-shaped conductors of varying heights.....	47
Figure 29. Parameterization of trapezoidal conductors.....	48
Figure 30. Sample Voronoi diagrams .....	48
Figure 31. Tessellated slot cavity with directional bias .....	49
Figure 32. Control point sampling .....	50
Figure 33. Sensitivity of generator performance metrics. Bottom right: Designs with lowest and highest efficiency.....	51
Figure 34. Shape metrics.....	52
Figure 35. Sensitivity of generator performance metrics to conductor shape metrics.....	52
Figure 36. Sensitivity of efficiency active parameters.....	53
Figure 37. The presence of support material when printing the insulation sleeve.....	53
Figure 38. Rotor structure parameters with magnet $B_r$ profile.....	55

Figure 39. (left) Image of the Fe <sub>3</sub> Si layer being printed during the SLM process and (right) completed build of the seven Fe <sub>3</sub> Si stator samples in a single run .....	60
Figure 40. (a) ORNL SS-3 standard sample specification with a thickness of 0.762 mm. for the dog bone samples shown in the inset of (b), and (b) tensile properties of SLM-printed Fe <sub>3</sub> Si.....	61
Figure 41. (a) Image of Bergey generator stator; (b) tensile properties of Bergey generator stator with ORNL SS-3 standard sample specification with a thickness of 0.0185 in. for the dog bone samples.....	64
Figure 42. SLM multimaterial printed Fe <sub>3</sub> Si premixed with Al alloy using the 15-kW Bergey generator stator design. ....	64
Figure 43. (left) SLM multimaterial printed Fe <sub>3</sub> Si stator laminate annealed at different temperatures and atmospheres (argon (Ar), hydrogen (H <sub>2</sub> ), and wet gas) and (right) the corresponding change in resistivity.....	65
Figure 44. SLM printed 6-in. reduced version of Bergey rotor can.....	66
Figure 45. The hardness properties of SLM printed dog bone samples.....	66
Figure 46. Permanent magnets suitable for use in wind turbine generators with saturation magnetization, M <sub>s</sub> (kG) and Curie temperature, T <sub>c</sub> (K). Energy product, BH <sub>max</sub> is represented in circle size. ....	67
Figure 47. Magnetic properties of NdFeB with zero Dy-SmFeN PPS bonded magnets .....	68
Figure 48. (left) Image of the Al block that was used for post-magnetic-field annealing with inserted BAAM magnets and (right) superconducting magnet .....	69
Figure 49. Schematic flowchart of fabricating insert/overmolding of the SLM printed Fe <sub>3</sub> Si rotor.....	70
Figure 50. SEM images of overmolded rotor .....	71
Figure 51. (a) Cast coils by Fraunhofer Institute with the potential to achieve 90% fill factor, (b) coils produced by Additive Drives, (c) ceramic insulated copper coils produced by extrusion, and (d) direct-ink write by NASA .....	72
Figure 52. An example serpentine pattern trace imaged on profilometer: (left) optical and (middle) topological images. (right) A cross section of the printed trace taken along the cyan line has been used for the calculation of the resistivity.....	74
Figure 53. The cross-sectional trace profiles taken of serpentine prints of various pastes. The height and width are in mm. ....	77
Figure 54. SEM images of the silver-coated copper powder. Note the small bimodal particle sizes, ideal for the condensed packing of particles.....	78
Figure 55. Insulating sleeve insert: (a) the crucial cross section of the insert design. The outlined area in red indicates the space available for the sleeve such that neighboring sleeves could be inserted on the 18-mm-wide laminate extensions without intersection. The angle of the horizontal red lines is owed to the increasing space surrounding the laminate as it expands outward radially. (b), (c), and (d) Final stator sleeve design from different angles.....	80
Figure 56. Three traditional stator geometries versus the new proposed stator geometry. The area of conductor is calculated at the displayed cross section of each stator. ....	81
Figure 57. (a–d) Four possible print configurations that were considered for FFF .....	82
Figure 58. Sleeve holder for printing. A sketch depicting printing (a) without the sleeve holder and (b) with the sleeve holder. (c–e) Optical images of the sleeve holder. ....	83
Figure 59. A sleeve (ULTEM 1010, two-part FFF option) partially filled with the AgCu0204-12 paste..	84
Figure 60. Shaped, segmented magnets that can be printed to realize larger dimensions in larger generators .....	87
Figure 61. 3D model of shape-optimized conductors .....	89
Figure 62. New features that can be introduced for further lightweighting.....	90
Figure 63. Optimized rotor can and reach possible by internal spray coating.....	97
Figure 64. (a) Small-scale pellet printer with exploded view of the print head extruder assembly. Print head has two heater zones, one close to the feed throat and the other close to the nozzle. (b)	

Sample magnet printed by Tumaker: 2-in. (50.8 mm) outer diameter, 0.75-in. (19.5 mm) inner diameter, and 4-mm thickness .....	99
Figure 65. (a) Hysteresis loop of as-printed (300 K as-printed) using Tumaker printer and post-aligned (300 K aligned) small-scale hybrid NdFeB SmFeN PA12 magnets and (b) hysteresis loop of BAAM-printed magnets of the same composition.....	100
Figure 66. (a) Sample coil printed by Additive Drives, (b) samples machined from printed coil, and (c) dog bone specimen being tested using ULVAC ZEM-3.....	101
Figure 67. SEM images of the microstructure of printed coils: (a) surface and (b) coil side .....	102
Figure 68. Stress versus strain measurements on machined samples .....	102

## List of Tables

Table 1. Comparison of Material Properties Between Additively Manufactured Metals and Traditionally Manufactured Materials Used in Electric Machines .....	7
Table 2. MADE3D Multiyear Program Timeline and Targets .....	11
Table 3. Baseline Generator Specifications and Optimization Targets .....	12
Table 4. Design, Materials, and Processes Advanced as Part of MADE3D and Their TRLs.....	15
Table 5. Material Combinations Used in Topology Optimization.....	22
Table 6. Optimized Results for Rotor Core From Regression Model and MADE3D-AML™ .....	24
Table 7. Optimized Results for Magnets from Regression Model and MADE3D-AML™ .....	25
Table 8. Materials and Manufacturing Methods for the Different Parts of the Bergey Generator .....	32
Table 9. Target Performance Metrics for Advanced Design Space Exploration .....	36
Table 10. Parameterization for Crown-Shaped and V-Shaped Magnets .....	37
Table 11. Comparison of Optimized Interior Permanent Magnet Designs Against the Baseline Generator .....	39
Table 12. Comparison of Optimized Crown-Shaped Permanent-Magnet Designs Against the Baseline Generator.....	40
Table 13. Properties of Baseline Sintered Magnets and Printed Magnets .....	41
Table 14. Results of Optimized Designs.....	45
Table 15. Printed Materials Considered in This Study .....	50
Table 16. Optimized Designs From Using Tessellations.....	54
Table 17. Results From Structural Mass Optimization.....	56
Table 18. List of Soft Magnetic Materials With Saturation Magnetization and Relative Permeability and 3D Printing Methods.....	59
Table 19. Nominal Process Parameters for Printing Fe3Si Stators Using Renishaw AM250 .....	60
Table 20. Mechanical Properties of the Fe-3Si Alloy Using ORNL SS-3 Standard Samples.....	62
Table 21. Comparison of Magnetic and Electrical Properties of Conventionally Processed Electrical Steel and SLM Fe3Si Laminates.....	62
Table 22. Magnetic Properties of BJAM Fe-3Si With and Without Al <sub>2</sub> O <sub>3</sub> Composites Compared With SLM Printed Fe3Si.....	63
Table 23. Magnetic Properties of NdFeB With Zero Dy-SmFeN PPS Bonded Magnets.....	68
Table 24. Conductors and Insulation in Baseline Generator.....	73
Table 25. Conductive Pastes, Curing Conditions, Electrical Resistance, Cross-Sectional Area, and Resistivity for the Samples Explored in This Work.....	75
Table 26. Dimensions of Main Components in 15-kW and 15-MW Direct-Drive Generators .....	93
Table 27. Optimized Print Parameters and Results on the Magnetic Strength Measurements .....	99
Table 28. Tensile Strength Measurements on Machined Samples.....	102
Table 29. A Summary of State-of-the-Art Commercial Printers .....	103
Table 30. Challenges in Reducing Printing Costs for Some of the Investigated Technologies.....	106

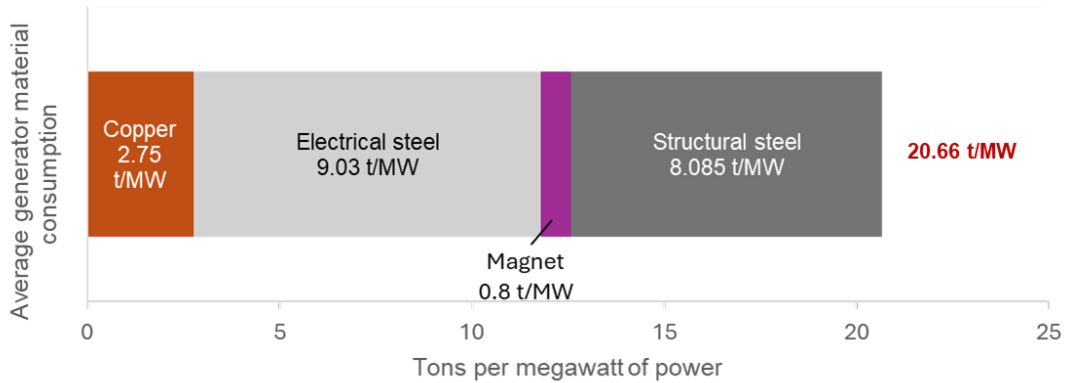
# 1 Introduction

In recent years, the offshore wind turbine industry has witnessed significant growth in the scale and size of turbines to 10 megawatts (MW) and beyond to lower the costs of energy by leveraging better wind resources with larger rotors and fewer wind turbines per wind farm. The United States also has ambitious targets of deploying up to 30 gigawatts of offshore wind energy by 2030, which can only be possible with large turbines rated 10 MW and beyond. One of the critical balancing acts faced by the offshore wind energy industry is achieving high power densities to maximize energy production while simultaneously limiting the weight of wind turbine components such as the nacelle, blades, and tower and reducing the need for critical raw materials, considering their soaring prices and supply chain shortages. Specific details on these challenges include:

- **Weight and transportability.** For example, a direct-drive wind turbine generator alone can weigh over 300 metric tons (t) and span more than 10 meters (m) in diameter, which introduces challenges for transportation by shipping vessels. Limitations in lifting operations<sup>1</sup> for generators that weigh more than 200 t are forcing many manufacturers to move their factories to port locations and resort to new manufacturing methods (Vries 2023).
- **Raw materials demand and prices.** With many of the emerging large wind turbine technologies employing either direct-drive or medium-speed drivetrains, they also place a huge strain on critical raw materials such as zinc, copper, nickel, chromium, silicon, and rare earth elements (REEs) that are needed for the different magnetic and structural components of the generator, including the rotor and stator. For direct-drive generators rated 15 MW and beyond (National Renewable Energy Laboratory [NREL] n.d.) (Barter, et al. 2023), the average mineral consumption is estimated at 20 t/MW (see Figure 1). Of this estimate, the demand for rare earth magnets alone is estimated to be up to 0.8 t/MW with a heavy reliance on Chinese sources (Global Wind Energy Council and Boston Consulting Group 2023). Direct-drive generators have high reliability, but their widespread adoption is challenged by the rising costs for materials beyond REEs, including the electric steel and copper needed to make them. The price of steel, magnets, and copper continue to soar, disrupting the manufacture and sourcing of raw materials needed for large machine manufacturing (McKinsey & Company 2023) (Ferris 2023).

---

<sup>1</sup> The maximum lifting capacity of a large, currently available Liebherr crane (HLC 295000) is 200 t for a 150-m lifting height (Bensalah, Barakat and Amara 2022).



**Figure 1. Volume of minerals estimated for direct-drive generators rated 15 MW and beyond**

- Manufacturing infrastructure.** Currently, the United States lacks established magnet production infrastructure. The limited capacities of existing manufacturing infrastructure for electrical steel and copper wire cannot meet the critical raw material demand for next-generation generators (Williams, Zhao and Lee 2022) (Shields, et al. 2023). A growing emphasis has been on designing with reduced demand for critical raw materials and on manufacturing innovations (Wooley and Matos 2023) aimed at pushing the power densities using new alternative materials that can ensure sustainable sourcing and bolster production capabilities.

Yet, existing design methods, materials, and manufacturing for reducing the material requirements (or lightweighting), particularly for wind turbine generators, have limitations.

## 1.1 Limitations in Generator Design

The traditional and most popular design choice of wind turbine generators are radial flux permanent magnet generators with surface-mounted magnets. Traditional design methods use parameter optimization techniques that assume standard geometries for rotor, stator, and magnets and that leverage conventional high-volume manufacturing but result in suboptimal use of both an active electromagnetic and inactive support structure. Several commercial magnetic optimization software programs offer a limited library of parameterizable geometries (arcs and line segments) that have few geometric variables to limit realizing designs that may be more applicable for wind turbines but are not discoverable in the normal process of design space exploration. While topology optimization techniques are emerging in some commercial software, they are time-consuming and computationally expensive, which limits their practicality. The following limitations exist in reducing the amount of critical raw materials using innovative designs:

- Reducing the amount of electrical and structural steel used in the generator is a trade-off between choosing excellent magnetic properties that achieve low-torque pulsations and maintaining structural integrity and stiffness against deformations under high-torque loads experienced in wind turbines. Electrical steel has good machinability properties; however, designing with very thin sheet laminations in the stator to minimize eddy current losses and introducing complex shapes in the stator or cast rotor construction require expensive molds and tooling assembly and result in excessive waste. Advanced

optimization methods have made lightweighting strategies for support structures possible, but the resulting geometries require advanced manufacturing.

- Reducing the amount of copper used in generators has necessitated the use of double-layer concentrated winding layouts along with tooth optimization to achieve high current densities and potentially using less copper for the same power output. However, these layouts can create challenges with heat dissipation. Further, finding the optimal balance between the slot fill factor and magnetic performance has also been difficult. As a result, designers resort to using alternate-shaped conductors instead of round wires, such as preformed hairpin coils for tighter packing within the slots, to achieve a higher fill factor. However, that can be a more complex and potentially more expensive manufacturing process. Stator slot skewing and magnet shape profiling have shown the ability to mitigate cogging torque, a phenomenon that can cause undesirable torque pulsations; however, these methods can complicate manufacturing.
- **Reducing REE content in generators** often entails using powerful magnets with a high intrinsic energy product that can help achieve the necessary overall magnetic field strength. Newer, much larger machines employ interior permanent-magnet machines that use field focusing to achieve higher torque densities. More than 25 t of magnets are needed, especially at higher power ratings (Barter, et al. 2023). Some wind original equipment manufacturers (OEMs) are resorting to dysprosium (Dy)-free magnets, but using these magnets requires improved cooling systems to compensate for their low-temperature capabilities (De Vries 2019). Designing with lower-grade magnets or magnets without REEs requires complex topologies such as axial flux machines (GreenSpur n.d.) that increase manufacturing complexity. Although most magnet geometries used in wind turbine generators are traditionally bar-shaped or cylindrical ring-type structures featuring minor changes to their profile, limited performance improvements in terms of efficiency and cogging torque reduction have been possible using special profiling of magnets and skewing that often increase tooling and manufacturing costs and are counterproductive. These include introducing an inverse cosine function on specific sections of the magnet's pole face to achieve a more sinusoidal air-gap flux density waveform and improve torque characteristics (minimize cogging torque and torque ripple). Any other changes in the magnet shape have been challenging to realize and increase the difficulty in manufacturing and costs.

## 1.2 Limitations in Materials

Most offshore wind turbine generators employ materials that can withstand a corrosive environment and high operating temperatures. With rising prices, OEMs are constantly researching the best trade-offs among performance, cost, and supply chain concerns through new materials.

- Non-grain-oriented electrical steel (NOES) is often used in these generators for flux concentration. However, it has lower magnetic permeability and higher core losses from high resistivity. NOES is low-alloy steel made with 95%–98% iron, < 4% silicon, and trace amounts of carbon, manganese, and sulfur. Increasing silicon content or adding alloying elements can improve resistivity and grain structure; however, NOES undergoes a specific cold-rolling process that influences the final grain structure and magnetic properties of the steel and often introduces internal stresses within the steel, potentially



leading to higher hysteresis losses in the core during operation. To compensate for the lower permeability of NOES and maintain the desired magnetic flux for power generation, the core designs need to be larger.

- In terms of permanent magnets, most modern wind turbine generators use high-grade sintered NdFeB magnets (N45—high coercivity grade or higher) that contain more than 30% of REEs by weight (e.g., neodymium [Nd], dysprosium [Dy], terbium [Tb], and praseodymium [Pr]) and 2% heavy rare earth element (HREE) Dy. Eliminating HREEs used in wind turbine generators remains a continuing research and development (R&D) goal with new technologies such as grain boundary diffusion coming to the forefront (BDT magnets n.d.). Reducing REE content with sintered magnets of more complex shapes makes material design challenging because the magnetic field density and force are not linear relative to distance. As a result, some wind OEMs are resorting to partial substitution of HREE with other elements such as terbium or gadolinium (Gd), or non-HREE materials such as praseodymium. However, significant adjustments in the manufacturing process are needed and may not yet achieve the desired temperature performance.
- Multimegawatt generators require up to 20 t of multistrand copper wires, (Barter, et al. 2023), the prices of which have risen recently. Higher copper prices have driven some manufacturers to consider aluminum; however, aluminum wires require a 50% larger cross-sectional area to achieve similar levels of electrical resistivity and conductivity (McKenzie 2019).

### 1.3 Limitations in Assembly and Manufacturing

Manufacturing a near-net-shape lightweight stator or rotor core often entails a multistage forming process that employs special molds and punching and stamping tools. Because of the rolling and punching process steps, the standard thickness of laminations is limited to 0.2–0.65 millimeters (mm). This limitation means the ohmic power loss by circulating eddy current losses in the core and magnets can be significant and the heat produced in a solid rotor yoke can increase magnet temperatures. Further, up to 50% of material offcuts occur when forming the near-net-shape laminations that need to be recycled.

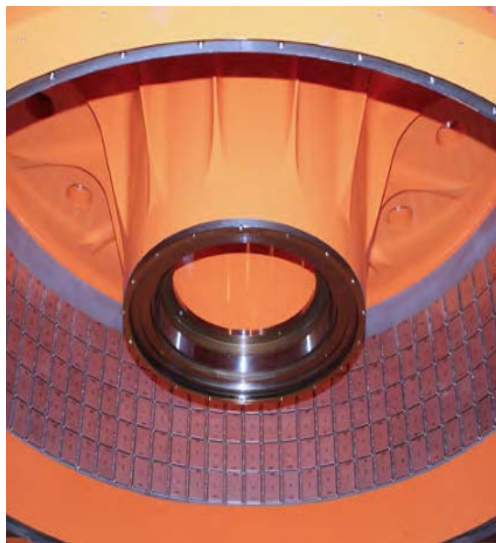
- In terms of winding insertion methods, existing methods use preformed stranded (see Figure 2) coils that limit the maximum slot-filling factor (in the range of 0.45–0.65), which greatly limits the opportunities for achieving high power densities.



**Figure 2. Winding process in a synchronous wind turbine generator.**

Photo from (Africa 2019)

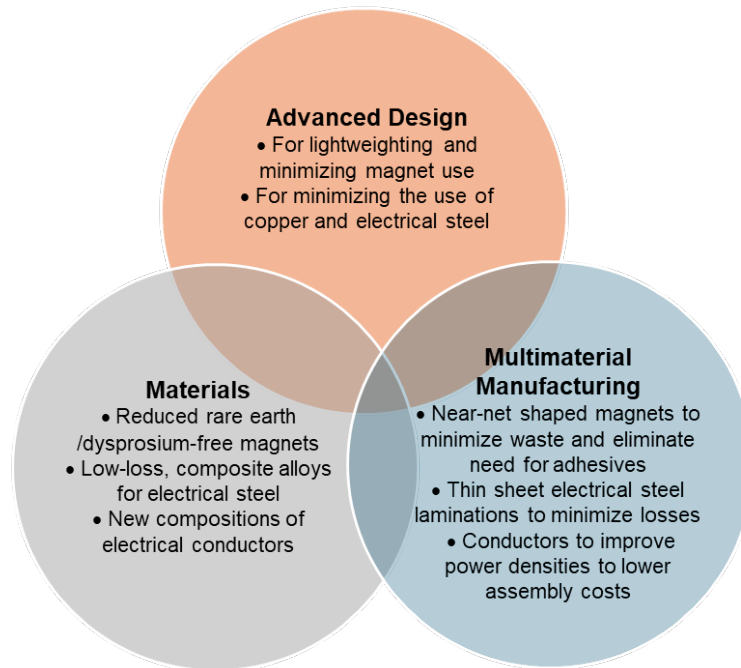
- In terms of magnets, high-power generators typically require magnet dimensions of 60 mm by 128 mm and axial length exceeding 1 m; however, commercially available magnets are shorter and must be axially arranged as segments. In some cases, the magnets are magnetized and retained in position by glue and hermetically sealed module construction. Manufacturing complex shapes to minimize magnet material using even simple machining is extremely difficult on a magnet, requiring significant expertise and specialized equipment (see Figure 3). For example, magnets are brittle, fragile, and can easily shatter, and can become demagnetized by the heat of the drill or power tool. Additionally, because these permanent magnets are extremely powerful and assembled in repelling positions by gluing or mechanical fastening techniques, manufacturing and safety issues impose serious design restrictions.



**Figure 3. Magnets in an outer rotor direct-drive permanent-magnet synchronous wind turbine generator.**

Photo from (YASKAWA 2024)

Considering these limitations, a multipronged approach (see Figure 4) is needed to integrate new methods for design, materials, and production that can help overcome the challenges in weight reduction and material demand and transform U.S. manufacturing that can help improve and promote domestic sourcing of raw materials and promote innovations to address material shortages.



**Figure 4. Research gaps and needs for next-generation wind turbine generators**

## 1.4 Metal Additive Manufacturing

Additive manufacturing presents a new opportunity to realize these goals by overcoming several shortcomings from materials, design, and manufacturing perspectives. In recent years, new capabilities and high-performing materials have emerged to additively manufacture every part of the generator, including magnetic core packs (Selema, Beretta, et al. 2023), permanent magnets, coils/windings (Additive drives GmbH n.d.), electrical insulation, and thermal management component cooling channels. These new capabilities include extrusion-based printing technologies (fused filament fabrication [FFF]) for permanent magnets with low REE content (Gandha, Paranthaman, et al. 2022) and selective laser melting (SLM) and binder jetting additive technology (BJAT) for electrical and structural steel and copper. These technologies are in various stages of development. Considerable effort and research are also being undertaken to improve printability of materials to help create advanced metals and composites (Elementum n.d.) (VTT Research 2021). In addition, wind turbine OEMs and commercial three-dimensional (3D) printer manufacturers have recently been collaborating on large-scale 3D printer technologies to enable on-site manufacturing of metallic near-net-shape components ranging from 10 to over 60 t and to produce molds up to 9.5 m in diameter (Sher 2021).

As the metal additive manufacturing technology for functional magnetic materials continues to mature, and properties of printed magnetic materials show promise, new design freedom helps explore complex geometries that were never explored for electric machines (see Table 1).

**Table 1. Comparison of Material Properties Between Additively Manufactured Metals and Traditionally Manufactured Materials Used in Electric Machines**

The values are as of 2020 and adapted from (Tiismus, et al. 2022)

Material	Property	3D-Printed Material	Commercial-Grade Material Used in Wind Turbines
<b>Electrical Steel</b>	Saturation magnetization Core loss measured at 1 T and 60 Hz	$B_{sat} = 1.5$ T (non-grain-oriented [NGO] Fe3Si) using SLM W10/60 Hz – 1.34 W/kg (NGO Fe3Si) with a minimum thickness of 0.4-mm sheets printed using SLM (Plotkowski, et al. 2019). $B_{sat} = 1.83$ T (NGO Fe6Si using BJAT W1 T/60 Hz – 14.99 W/kg (NGO Fe6Si) with a minimum thickness of ~1.02 mm on a ring sample (Cramer, et al. 2019) Electrical discharge machining slicing can achieve thinner laminations as week as a stacking factor of ~90%	<ul style="list-style-type: none"> <li><math>B_{sat} &gt; 2.0</math> T (NGO Fe3Si)</li> <li>W10/60 – 0.7 W/kg (NGO Fe3Si, 0.35 mm)</li> </ul> Fill/stacking of commercial laminations is typically 90%–96%, depending on the stamping thickness and quality.
<b>Permanent Magnet</b>	Maximum energy product ( $BH_{max}$ ) Remanence ( $B_r$ ) Intrinsic coercivity ( $H_{ci}$ ) Resistivity ( $\rho$ )	<ul style="list-style-type: none"> <li><math>BH_{max} = 45</math> kJ/m<sup>3</sup> (isotropic 63.37 vol% NdFeB-PPS bonded magnet (Paranthaman, et al. 2020))</li> <li><math>B_r = 0.5</math> T</li> <li><math>H_{ci} \sim 915</math> kA/m</li> <li><math>\rho \sim 0.02</math> <math>\Omega \cdot m</math></li> </ul>	<ul style="list-style-type: none"> <li><math>BH_{max} \sim 400</math> kJ/m<sup>3</sup> (typical N48 grade, sintered anisotropic 99 vol% NdFeB magnet)</li> <li><math>B_r = 1.35</math> T</li> <li><math>H_{ci} = 1,480</math> kA/m</li> <li><math>\rho = 1.5 \times 10^{-6}</math> <math>\Omega \cdot m</math></li> </ul>
<b>Electrical Conductor</b>	Electrical conductivity	<ul style="list-style-type: none"> <li>% International Annealed Copper Standard (IACS) conductivity – 71% (multimaterial extrusion of copper and ceramic (Lorenz, Rudolph and Wemer 2018))</li> </ul>	<ul style="list-style-type: none"> <li>% IACS conductivity – 102% (copper-oxygen free)</li> </ul>

Units used in table: Hz = hertz; kA = kiloampere; kg = kilogram; kJ = kilojoule; T = tesla; W = watts

Although a fully printed electric machine is a goal for large-scale industrial manufacturing, several unknowns and limitations remain, including scalability of build envelope, printing speeds, structural imperfections in printed parts, and multimaterial printing capabilities. Additive manufacturing of hard magnetic materials is predominantly limited by the low magnet fraction loadability in some commercial FFF printers and still requires process optimization. This has greatly limited the possible maximum energy product and coercivity (resistance to demagnetization). Furthermore, their demagnetization strengths at higher temperatures are unknown. In terms of electrical steel, laser powder bed fusion (LPBF) processes have so far yielded the best saturation flux densities of up to 1.85 T; however, higher polarization fields are still achievable. Achieving laminate thicknesses lower than 0.35 mm remains an important R&D goal and may be possible by multimaterial printing of interlaminar insulation and metal at the same time. In terms of electrically conductive materials, multimaterial printing capabilities are not yet available for forming interturn insulations; the maximum achievable slot-fill factor with

minimum insulation thickness with some of the methods is unknown. While some performance gaps exist, mapping an electric machine with such 3D-printed materials and the performance of such designs have been largely limited to individual components at a small scale, especially electrical cores in reluctance machines.

While conventional design optimization techniques aim for optimizing geometries within traditional manufacturing constraints, new, advanced design methods such as topology optimization and shape optimization have emerged and are finding applications in lightweighting electric machines (Gangl 2018), including active and inactive materials of the generator (Jaen-Sola 2020). Limited research has been conducted using these methods for magnet optimization in wind turbine generators (McGarry, McDonald and Alotaibi 2019). A traditional approach to design relies on the experience of the designer to come up with the parameterization of geometries as allowed by traditional manufacturing, and it is susceptible to designer bias. Topology optimization uses material distribution as the main variable with final geometry or shape only determined by the function of the structure and the underlying physics. While several mathematical techniques are available for performing such advanced design optimization (Ma 2020), they result in very complex geometries. Because of conventional manufacturing limitations, limited design freedom has been explored, even with such advanced topology optimization methods. Further, the multidisciplinary nature of the design problem causes such design methods to experience computational inefficiencies. New design tools that are computationally more efficient are needed, along with the successful integration of new materials through additive manufacturing. These advances would help address several of the challenges and limitations identified earlier in the following ways:

- **Design tools for lightweighting.** Because some additive manufacturing processes can handle more than one material, a generator design can be improved for optimal performance, reduced weight, and reduced material using a combination of more than one material for one component. New optimization techniques that allow for better control of material placement can be explored along with the design freedom allowed by additive manufacturing. For example, for magnets, it may be possible to use a lower-grade material along with a higher-grade material to use less critical material. Because additive manufacturing also allows for complex shapes, it will be possible to simultaneously optimize the design of magnets with electrical steel or electrical conductors with insulation. As a result, various conductor shapes can be realized, and a high fill factor may be possible that can help reduce the dimensions of the machine.
- **Materials.** While printed materials have performance gaps, new powder processing technologies are emerging, and the capabilities of printers are evolving to handle new materials. Printing processes for reduced rare earth magnets can be optimized to improve magnet fraction loadability along with dedicated magnetic field measurements at higher temperatures to improve their coercivity. In addition, new low-alloy steel composites can be explored to realize higher saturation flux densities in the core. Furthermore, new compositions for electrical conductors, including hybrid alloys of copper, silver, or aluminum, can be tailored to improve their conductivities.
- **Manufacturing.** Some progress has been made with printed electrical steel, polymer-bonded magnets, and conductors, which have been investigated for use in small-scale (kilowatt-scale) electric machines. Investigating their scalability and feasibility for larger-scale machines such as direct-drive generators can offer new opportunities for wind

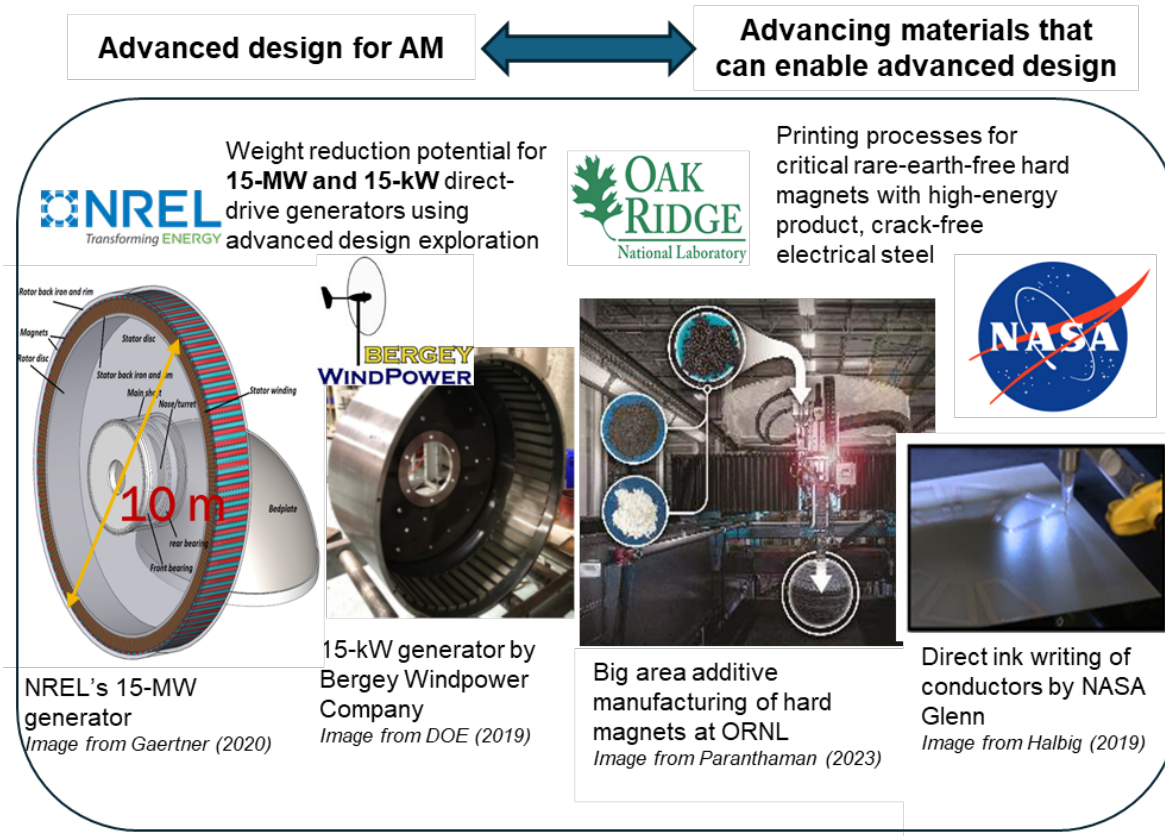
turbine generator manufacturing. For example, multimaterial printing of near-net-shape magnets with rotor core can help tailor properties of different materials in the print and independently optimize materials within a component to minimize the use of magnets and adhesives as well as help minimize material waste that otherwise comes from machining. Permanent magnets can be used for high strength, whereas the core can be made from a soft magnetic material with low coercivity for efficient magnetic flux channeling. Conductors with insulation and electrical steel laminations with interlaminar coating can eliminate multiple steps in electric machine manufacturing.

## 1.5 The MADE3D™ Project

Inspired by these developments and challenges, the Manufacturing and Additive Design of Electric Machines enabled by 3D Printing (MADE3D) project is a \$3.525 million multiyear research project sponsored by the U.S. Department of Energy Wind Energy Technologies Office through a merit review application process in Fiscal Year (FY) 2018 and awarded in FY 2020. Led by the National Renewable Energy Laboratory (NREL), the program spanned 5 years from FY 2020 through FY 2024. It focused on developing and advancing new computationally efficient design tools for lightweighting wind turbine generators (minimizing critical material usage) by leveraging artificial-intelligence-based generative optimization techniques and new high-performance printed materials developed by Oak Ridge National Laboratory (ORNL), the National Aeronautics and Space Administration Glenn Research Center (NASA Glenn), and industry subcontractors, namely Renishaw, ExOne, Volunteer Aerospace, and Bergey Windpower Company (Bergey). New capabilities with multidisciplinary expertise across NREL and ORNL in advanced electric machine design and manufacturing were developed with a focus on advancing the technology readiness levels (TRLs) for printed permanent magnets, electrical steel, and electrical conductors to TRL 4 and TRL 5. The team identified several new opportunities, risks, and challenges in scaling the developed technologies for large-scale manufacturing of next-generation wind turbine generators.

## 1.6 Approach

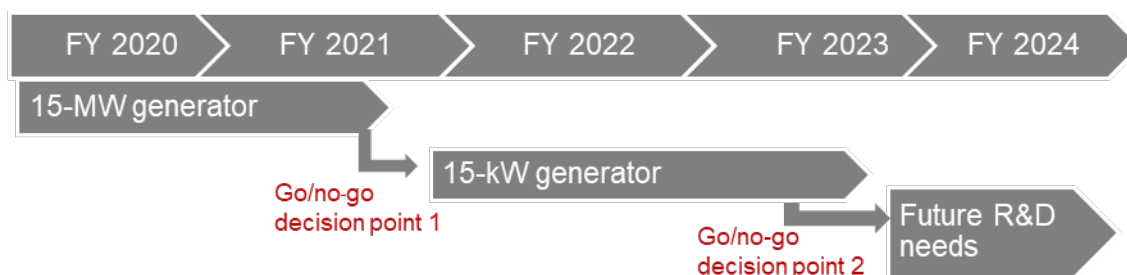
As shown in Figure 5, we developed a two-pronged approach to advance the design and manufacturing technologies from TRL 3 to TRL 4 and TRL 5, respectively, over a period of 4 years from 2020 to 2024. Table 2 lists the activities by year.



**Figure 5. MADE3D project approach**

NREL led the development of new design toolsets to help identify how to reduce the mass of active materials in generators used in two different classes of wind turbines. The emphasis has been on reducing the critical rare earth magnets, electrical steel mass, and electrical conductor mass from these generators, as they account for the highest costs and supply chain challenges. Initial efforts focused on developing the electromagnetic topology optimization toolsets using the International Energy Agency (IEA) 15-MW offshore direct-drive wind turbine generator as the baseline design (Gaertner, et al. 2020). The developed toolsets were extended and applied to a small-scale, commercial wind turbine generator by Bergey Windpower Co, modeled around a 15-kilowatt (kW) wind turbine (EERE Office of Energy Efficiency & Renewable Energy 2019). ORNL led the development of multimaterial printing processes needed to enable the new, lightweight magnet designs developed by NREL. These processes included identifying and advancing high-energy candidate rare-earth-free magnets and low-loss electrical steel with 3.0% and 6% silicon content. Composite materials for both hard and soft magnets were also explored. NASA Glenn led the development of multimaterial printing processes for conductors and insulation. Table 2 provides the targets and deliverables from the project. The project had two go/no-go decision points and was merit reviewed in FY 2021. An expert review panel was formed in October 2021, with panelists from diverse backgrounds, including electric machine designers from OEMs GE Vernova, Siemens Technology Corporation, and ABB, and magnet supplier Arnold Magnetics. Feedback was used to determine the feasibility of developed methods for a small-scale proof-of-concept generator and to identify future R&D needs, risks, and opportunities.

**Table 2. MADE3D Multiyear Program Timeline and Targets**



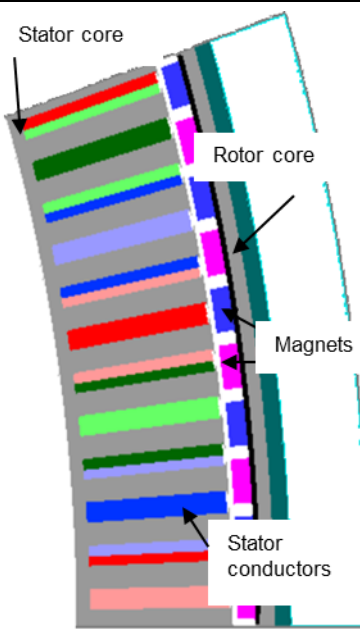
FY 2020 Activities	FY 2021 Activities	FY2022 Activities	FY2023 Activities	FY2024 Activities
<p>Develop new topology optimization tools for electromagnetic design for a baseline direct-drive generator</p> <p><b>Deliverable/Outcomes:</b> New electromagnetic topology optimization toolset - MADE3D Advanced Machine Learning™</p> <p>Evaluate feasibility of printing processes for low-loss electrical steel and rare-earth-free magnets</p>	<p>Use new toolsets to complete optimization of electromagnetically active parts of the 15-MW generator rotor</p> <p><b>Deliverable/Outcomes:</b> Optimization potential for 15-MW generator</p> <p>Advance multimaterial processing of soft magnet composites</p>	<p>Advance toolsets for multiphysics topology optimization for the 15-MW generator</p> <p><b>Deliverable/Outcomes:</b> New toolset and advanced lightweight designs for 15-MW generator rotor</p> <p>Advance 3D printing methods for Dy-free magnet with increased magnetic loading</p> <p>Develop multimaterial manufacturing of magnets with iron</p> <p>Compare material properties and processes for the baseline 15-kW generator with printing materials and processes</p>	<p>Apply design tools (MADE3D Advanced Machine Learning™) with multiphysics capability to optimize a 15-kW proof-of-concept prototype; this involves optimizing the rotor core with magnets and stator core and structural steel</p> <p><b>Deliverable/Outcomes:</b> Optimization potential for 15-kW generator and advanced lightweight design</p> <p>Advance printing processes for stator conductors</p> <p>Conduct an industry survey on the most feasible advanced manufacturing processes for rotor and stator of 15-kW and scaling up to megawatt-class generators</p> <p>Conduct a gap analysis to identify opportunities, challenges, and risks in scaling up printing processes</p>	<p>Design tools for optimizing stator conductors</p> <p><b>Deliverable/Outcomes:</b> Lightweight optimized conductor design</p> <p>Conduct a gap analysis to identify opportunities, challenges, and risks in scaling up printing processes for stator laminates and conductors</p>



### 1.6.1 Advanced Design Tools for Additive Manufacturing

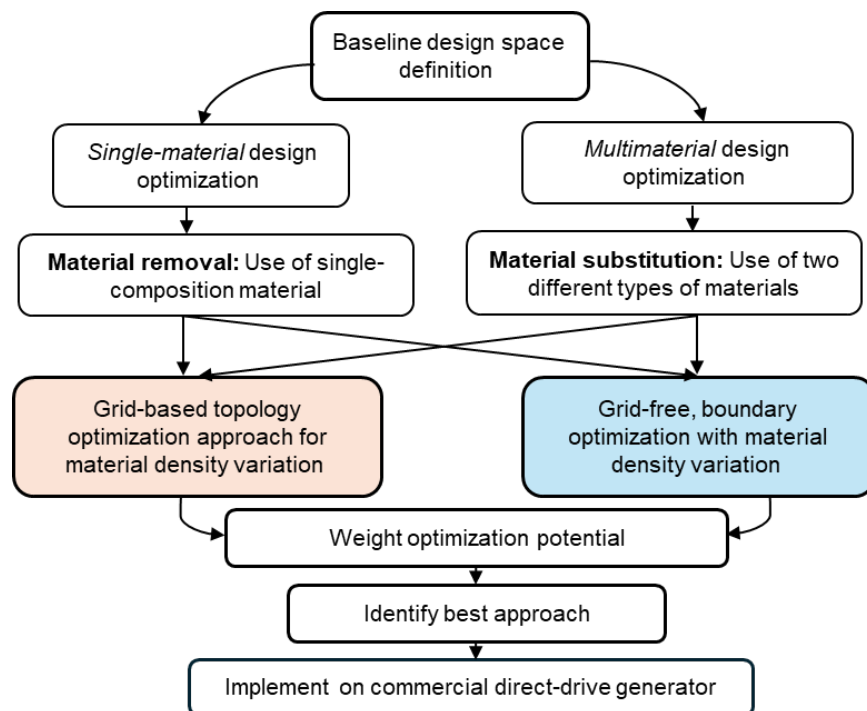
To develop an advanced electromagnetic topology optimization toolset, we identified a baseline direct-drive generator as a first step. We chose to model the IEA 15-MW, direct-drive radial-flux permanent-magnet generator (Gaertner, et al. 2020) that was originally optimized using a traditional design approach with conventionally manufactured materials. The generator is an outer rotor/inner stator, radial-flux, permanent-magnet machine with a rated torque of 20.48 meganewton-meter (MNm) and rated speed of 7.58 revolutions per minute (rpm). The rotor active mass including the magnets and electrical steel was 58 t, whereas the stator active mass was 147.26 t. The baseline magnets were of N40 grade with 3% Dy content, and baseline stator laminations used M-36 grade steel.

**Table 3. Baseline Generator Specifications and Optimization Targets**

Baseline Generator	Parameter	Units	15-MW Baseline	Optimization Targets
 <p>The diagram shows a cross-section of a generator. On the left is the stator core with stator conductors. On the right is the rotor core with magnets. Labels include: Stator core, Rotor core, Magnets, and Stator conductors.</p>	Air gap diameter	m	10.16	Same as baseline
	Core length	m	2.17	Same as baseline
	Pole pairs	-	100	Same as baseline
	Generator output phase voltage	V	4770.3	Same as baseline
	Efficiency at full load	%	96.55	Same as baseline
	Structural mass	t	157.3	Same as baseline
	Rotor core mass	t	34.00	Total reduction of up to 20 tons in active mass from rotor and stator core and magnets with zero Dy
	Magnet mass	t	24.01	
	Stator core mass	t	147.26	
	Copper mass	t	9.01	Same as baseline
	Torque	MNm	20.48	Same as baseline
	<b>Total Mass</b>	<b>t</b>	<b>371.57</b>	<b>~350</b>

As a second step, we identified design domains and performance optimization targets (see Table 3). We targeted a 20-t reduction in active mass from electrical steel and magnets. Because magnets are the most expensive component in the generator, this would directly translate to cost savings from reduced material usage. We performed an initial topology optimization using a conventional method and then identified more opportunities for lightweighting using advanced topology optimization techniques. We investigated two optimization approaches to better explore

the available design space (see Figure 6). The first approach investigated the use of single-composition material for each part that was optimized by careful removal of material in unnecessary regions, and the second approach used two materials and identified their optimal distribution for a single part. We treated both problems separately using a grid-based topology optimization and a free-form boundary optimization technique, and we identified the best optimization technique for achieving lightweight designs that met the performance targets. The details of the optimization approach and results are discussed later in Section 2. We developed the initial two-dimensional (2D) model for the baseline generator design using commercial finite element analysis (FEA) software, ALTAIR-FLUX, which served as the starting point for further analysis and optimization. Initial performance targets were based on transient magnetic FEA that was later extended for a multiphysics evaluation including thermal and structural analysis. After we identified the best approach, it was implemented on the 15-kW Bergey wind turbine generator.



**Figure 6. Design optimization approach**

### 1.6.2 Advanced Materials and Multimaterial Manufacturing Processes

Additive manufacturing, which creates parts layer by layer, opens new venues of improvements for industrial manufacturing of electric machines via near-net-shape production of complex geometries, potentially a reduction of part count and lead time, and conservation of nanocrystalline and amorphous soft magnetic composites. The magnetic, electrical, thermal, and mechanical properties of the magnetic materials are also greatly influenced by the selection of the additive manufacturing method. During the scoping studies of identifying the potential 3D printing methods for the MADE3D project, SLM, FFF, and BJAT methods dominated the additive manufacturing processing of soft magnetic materials and their integration in electric machines. ORNL worked with several material suppliers for sourcing the raw materials. These include Neo Magnequench, Aichi Steel, Nichia Corporation, Bunting Magnetics, Arnold

Magnetic Technologies, and Carpenter Technologies. While most of the printing trials and performance characterizations have been carried out at ORNL's Manufacturing Demonstration Facility (MDF), a few selected materials and printing were outsourced. For example, multimaterial LPBF printing was done at Beehive Technologies (formerly Volunteer Aerospace) for Fe<sub>3</sub>Si premixed with Al alloy powders; and extrusion-compression molding for bonded magnets was carried out at the University of Tennessee, Knoxville. Ames National Laboratory performed magnetic property measurements on the 3D printed magnets. ExOne's (X1-Lab) Binderjet printer and Renishaw's AM 250 both at ORNL's MDF were used for printing and testing electrical steel. Big area additive manufacturing (BAAM) was used for extrusion printing of polymer-bonded magnets. Based on ORNL's prior research efforts on composite electrical steel (Plotkowski, et al. 2019) and printer availability, the team selected SLM and BJAT methods to print soft magnetic materials. The NASA Glenn team was specifically focused on investigating multimaterial printing of a few candidate electrical conductors with insulation material by leveraging their prior research on direct ink writing (DIW). In addition, based on the initial materials selection and optimization of print parameters, the following materials and processes were advanced for generator components.

- Stator lamination: Fe<sub>6.5</sub>Si; Fe<sub>3</sub>Si (Binderjet; SLM) (FY 2020–2021); Fe<sub>6.5</sub>Si and Fe<sub>3</sub>Si with 1 wt.% Al<sub>2</sub>O<sub>3</sub> (Binderjet) (multimaterial printing) (FY 2022–2023); Fe-Co (SLM) (FY 2023); and Fe<sub>3</sub>Si with Al alloy (SLM) (multimaterial printing) (FY 2023–2024).
- Electrical conductors: copper, silver, silver-coated copper, and silver-copper hybrid paste formulations using the nScrypt 3dn-300 system.
- Electrical insulation: ULTEM 1010, Accura 25 (stereolithography) and Somos PerFORM (selective laser sintering).
- Rotor structural and magnetic core: Ti-V alloy (SLM) (FY 2021–2022); and stainless steel and carbon steel (SLM) (FY 2023–2024).
- Magnets: Anisotropic NdFeB bonded with nylon polymers (BAAM) (FY 2020–2021); NdFeB (Dy-free) with polyphenylene sulfide (PPS) polymers (BAAM) (FY 2021–2022); NdFeB (Dy-free) and SmFeN with nylon (BAAM) (FY 2022–2023); SmFeN Extrusion compression molding (FY 2024).

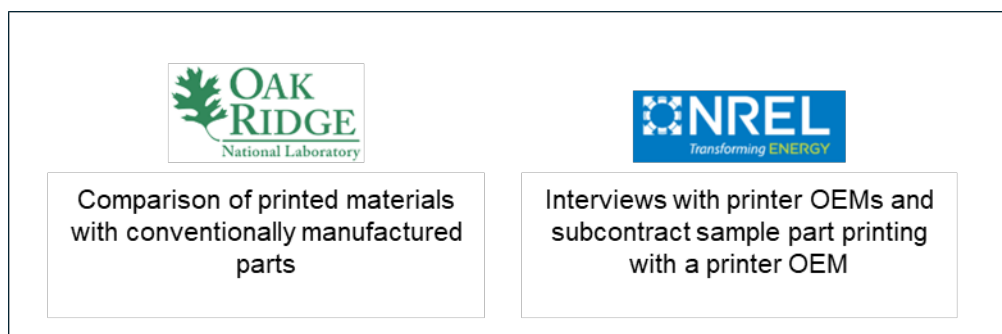
Materials, parts, and processes developed as part of MADE3D project are discussed in detail in Section 3, and their TRLs are shown in Table 4.

**Table 4. Design, Materials, and Processes Advanced as Part of MADE3D and Their TRLs**

Component/ Capability	Processes Investigated	Materials Investigated	TRL/Commercial Readiness							
			3	4	5	6	7	8	9	
Advanced design	Shape optimization	Polymer-bonded printed magnets coupled with printed Fe3Si; printed conductors		X						
Stator laminations	LPBF, BJAT	Al alloys and Al2O3	X							
Electrical conductors	DIW	Copper, silver-coated copper, silver, silver + copper		X						
Insulation sleeve for electrical conductors	FFF	ULTEM and stereolithography		X						
Rotor electrical steel	LPBF, BJAT	Fe3Si, Fe6Si, FeCo			X					
Reduced rare earth permanent magnets	FFF	AlNiCo, SmCo, Dy-free NdFeB, SmFeN+NdFeB+Nylon 12			X					
Multimaterial manufacturing of magnets and electrical steel	Insert molding	SmFeN+NdFeB+Nylon 12 with Fe3Si		X						

### 1.6.3 Gaps and Risk Assessment in Scaling

The NREL and ORNL teams undertook a bifurcated approach (see Figure 7) in assessing the gaps and risks in scaling the methods developed as part of the project. The ORNL team compared the functional properties of printed magnets, electrical steel, and copper conductors using the methods they developed in-house to those of conventionally manufactured parts of the 15-kW Bergey generator. The NREL team interviewed 15 state-of-the-art printer OEMs, both domestic and international, that specialized in various printing processes including SLM, BJAT printing, sand printing, and FFF. A discussion was held with each manufacturer to assess the technical capabilities of their printers, material handling, economic costs and benefits, and interest. Statements from each discussion were recorded and sorted to assess the broad state of industry capabilities and to identify gaps and risks in scaling different processes as well as their commercial readiness.



**Figure 7. Approach to gap and risk assessment**

**Stator laminations:** The ORNL team investigated the feasibility of manufacturing near-net-shaped stator laminate for the 15-kW Bergey generator using SLM on Renishaw’s AM250 machine. These laminates corresponded to the original dimensions of the generator. The electrical and mechanical characteristics of the printed laminate were compared against state-of-the-art conventionally manufactured stator laminate by Bergey. The difference in performance was used to identify risks and gaps in printing and their scalability for larger generators.

**Stator conductors:** ORNL worked with Beehive Industries to conduct printing trials on copper alloy conductors. NREL also worked with NASA Glenn to assess the feasibility of multimaterial printing of conductors with insulation for the Bergey machine. They investigated several compositions of silver and copper conductors. NREL worked with Additive Drives GmbH to print sample copper conductors for the Bergey machine. ORNL characterized some of the printed copper samples and used the differences in properties to assess the print quality and scalability of printing copper conductors for larger generators.

**Rotor core:** ORNL investigated the feasibility of printing a scaled version of the 15-kW Bergey rotor can using SLM at MDF on Renishaw’s AM250 machine. The rotor dimensions are 6 inches (in.) in diameter and approximately one-fourth the size of the original baseline generator—ORNL compared the mechanical properties with the Bergey rotor can and also identified risks and opportunities to scale to larger machines.

For assessing the feasibility of printing both rotor core and stator laminations using commercial printers, the NREL team contacted multiple printer OEMs that specialized in LPBF (Renishaw, Addman), direct energy deposition, and indirect additive manufacturing techniques such as sand printing of a mold followed by traditional casting in a foundry. For indirect additive manufacturing, the team reached out to Humtown Additive, ICC, and Trumbull Foundry and Alloy. The interviews helped identify limitations with materials and printing processes.

**Magnets:** ORNL had primarily worked with Cincinnati Inc. for process parameter optimization for printing critical rare-earth-free and reduced rare earth bonded permanent magnets on the BAAM printer. In addition, for printing higher loads of magnets (>75 vol%), extrusion followed by compression methods have been used. Printed magnets have been post-magnetic-field aligned to achieve high energy products with >95% or higher alignment. Based on this experience, ORNL contacted another commercial printer OEM, Tumaker, to investigate the transferability of the developed approach to their benchtop FFF printer. The team identified gaps and challenges in printing magnets on a commercial scale for both the Bergey machine as well as larger generators. The NREL team interviewed two of the largest FFF printer manufacturers specializing in pellet-based feedstock. These included Colorado-based 3D Systems and a Swedish company, Industry Inc. A sample magnet feedstock was shipped to Industry Inc. for assessing the feasibility of printing magnets. The team also spoke with an Australian OEM, Titomic, that focuses on spray-based printing. The details of the risks are reported in Section 4.

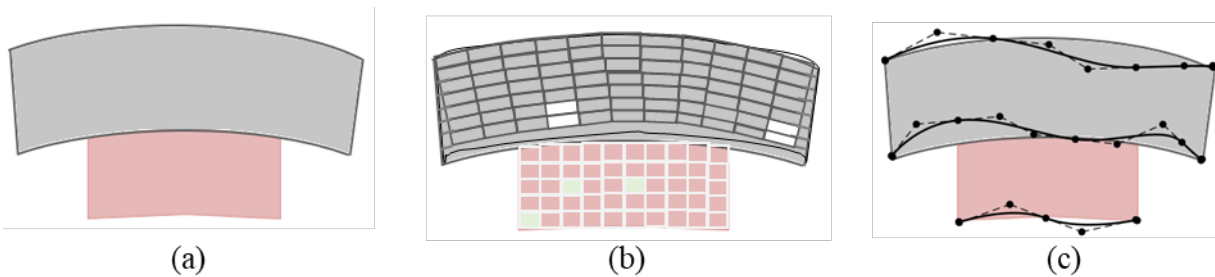
#### **1.6.4 Future R&D Needs**

To identify future R&D needs, the team assessed the progress made by the project in all three areas of design, materials, and manufacturing along with the industry survey to identify the limitations and what they saw as the primary needs to address the challenges of producing generator components by additive manufacturing. The details are available in Section 4. In terms

of additive manufacturing, the discussion focused on two key areas: technical challenges and economic challenges. Technical challenges encompass topics such as limitations in dimensional accuracy, surface finish quality, material selection, and material properties. The economic challenges encompass topics such as raw material and finished part costs and the business niche for this technology. Given the diversity of additive manufacturing techniques, it was necessary to categorize these discussions quite broadly. Future needs were identified by recording statements from the manufacturers and sorting them into either technical or economic challenges and then further into one or more subcategories as needed.

## 2 Advanced Design Optimization for Additive Manufacturing

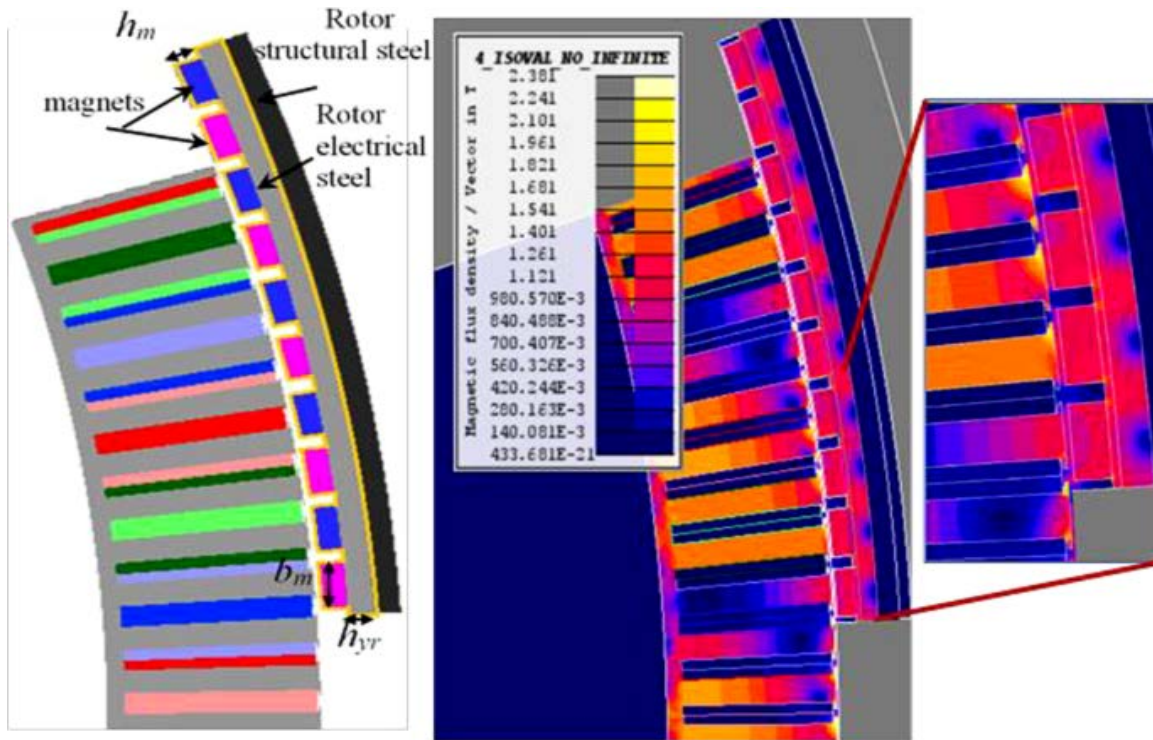
The main goal of advanced design optimization was mass reduction from four specific components including electrical steel in the rotor and stator, permanent magnets, and electrical conductors used in wind turbine generators while maintaining similar or better performance when compared to the baseline state-of-the-art generator. Using the IEA 15-MW generator design as the baseline, a 20-t weight reduction was targeted in magnets and electrical steel in the rotor and stator (see Section 1.6.1). The NREL team developed two separate workflows for advanced design optimization for additive manufacturing (see Figure 8). The first approach required defining a grid in the design domain, and the second approach used a parametric free-form optimization where the material boundaries were altered. A summary of these approaches and a new design tool are provided here. More details on these methods and results are available in (Sethuraman, Vijayakumar and Ananthan, et al. 2021) and (Sethuraman and Vijayakumar 2022). The best design approach was identified and implemented on a commercial direct-drive generator where in addition to magnet and electrical steel mass reduction, novel shape optimization for conductors was implemented using Voronoi tessellations that helped identify new lightweight conductor designs.



**Figure 8. Optimization approaches: (a) baseline pole, (b) grid-based topology optimization, (c) boundary optimization**

### 2.1 Advanced Design Tools for Topology Optimization Using a Grid-Based Approach

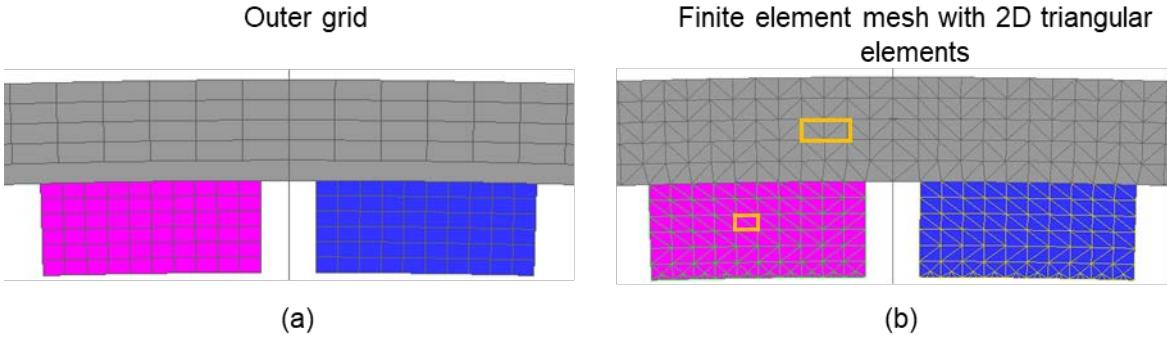
To develop design tools for optimizing magnetic design with a target reduction of 20 t, we first needed to understand the nature of magnetic loading in the different parts of a generator. We did this to ensure that any topology optimization can find the best possible design with minimal material and only remove material in regions of low magnetic loading and retain material in the most critical regions of high magnetic loading. We ran a 2D transient magnetic FEA simulation in ALTAIR-FLUX. This analysis helped identify regions of low magnetic loading in the rotor core and stator core regions (the dark blue regions in Figure 9) suggesting opportunities for material removal.



**Figure 7. Flux density contour in the 15-MW generator for rated operating conditions by transient magnetic FEA**

With this information, we chose to use a nonparametric topology optimization approach, where no geometric information was used as the variable; instead, a grid controlled the material distribution. This grid is overlaid on a finite element mesh such that each grid element corresponds to a subset of cells of the finite element mesh (see Figure 10). For the rotor, we used a 60-by-4 grid that resulted in 240 elements equally distributed in the radial and circumferential direction. For the magnet pole region, we used a 10-by-6 grid that resulted in 60 elements per pole. Each element had an area of  $0.125E-03 \text{ m}^2$ . Each element within the grid was assumed to either have material or air in the case of a *single-material* design or a second material in the case of a *multimaterial* design.





**Figure 8. Mesh definitions: (a) outer grid for geometric control of material distribution, and (b) inner mesh with FEA elements. Every rotor element in the outer grid is discretized by four triangular elements, and every magnet element in the outer grid is discretized by two triangular elements. These finite elements assume the property of the material that is assigned to each element in the outer grid (either air, or material).**

Any change in material distribution within one pole pair was then patterned around the circumference. We chose to first optimize the rotor core to determine the minimum required electrical steel to guide the flux behind the pole region, and then we optimized the magnet pole. Figure 11 shows the overall approach. A conventional approach to optimization was first performed where an initial design of experiments was done by Latin-hypercube sampling for different material combinations in an Altair Hyperstudy (ALTAIR, Design of experiments with hyperstudy—a study guide. n.d.). Each design resembled a pixel image with each pixel representing a specific material. For each of the designs, transient magnetic FEA simulations were run with the rotor sector traversing  $3.6^\circ$ . Responses for air-gap torque and rotor flux loading were measured. Rotor flux density was extracted from sensors located at each of the 48 mesh elements that guided material removal from rotor the core (single-material design) or material substitution (multimaterial design).

Because of the large number of pixels and designs, we needed surrogate models that approximated the performance of the generator for a given design and quickly predicted the performance without the need for FEAs. We constructed a regression-based surrogate model and determined the fitness functions for torque and rotor flux loading against the pixel elements that were then used to predict the performance and optimize a design using a response-surface-based optimization. This helped identify a single optimal design that met the performance targets (see Section 2.1.1). However, this process was computationally very expensive, requiring up to 17 hours of simulation to find an optimal design. We therefore developed new machine learning based on surrogate models: MADE3D-Advanced Machine Learning<sup>TM</sup>(AML) to significantly accelerate the design space exploration. MADE3D-AML<sup>TM</sup> is NREL’s proprietary software tool for topology optimization of various parts of an electric machine. Built using deep-learning networks, the networks are trained and tuned with design of experiments design information (pixel images or shape changes and responses). The target design specifications for torque, maximum rotor flux loading, and mass are user-defined inputs to optimize an objective function. The generated designs were then validated by FEA to verify the accuracy. Section 2.2.1 summarizes the overall capabilities of the software toolset.

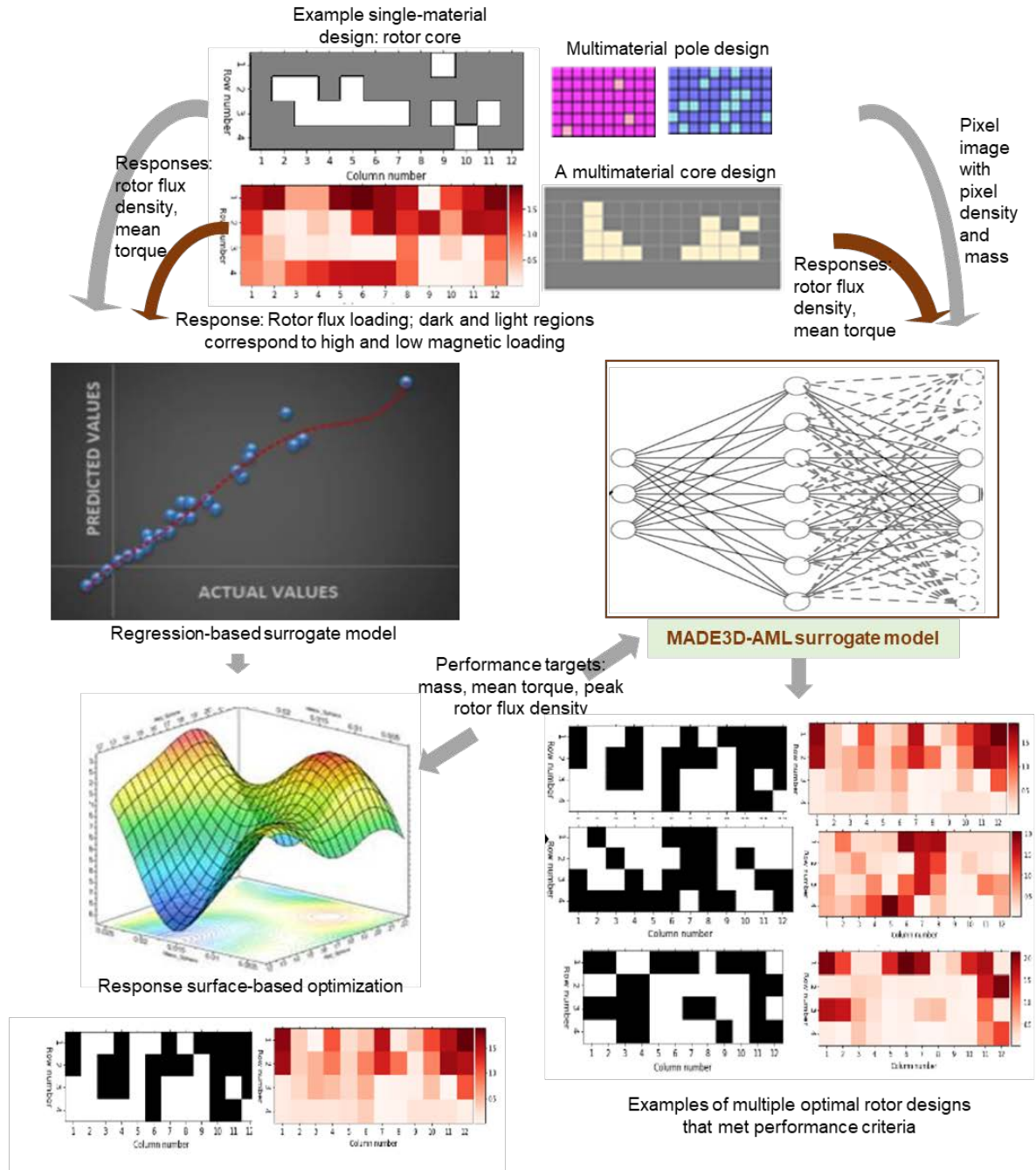


Figure 9. Topology optimization using surrogate models

### 2.1.1 Optimization Goals and Materials

Both approaches aimed to identify rotor core and magnet designs that can satisfy the target constraints on torque ( $\geq 20.48$  MNm) and maximum rotor flux density ( $\leq 2.03$  T) while also maximizing the torque per rotor active mass (Equation 2.1). Three formulations were used to achieve this both directly and indirectly by minimizing mass and maximizing mean torque. Each cell in the outer grid was controlled using a density-based scaling of the properties using a baseline material (Fe3Si steel for rotor core) and N40-grade sintered magnet for the magnets.

The mass for each design was calculated considering the material density for all the outer grid elements within one periodicity (18°) and then multiplied by 20 to get the overall mass for the full machine. The main properties for the materials are listed in Table 5 and were sourced from Altair’s material library (ALTAIR 2024). For printed electrical steel and soft magnetic composite, references were made to (Lamichhane, et al. 2023) and (Fluxtrol n.d.). In the case of multimaterial design magnets, we considered both sintered and polymer-bonded magnets (with zero Dy). The properties for printed polymer bonded magnets were taken from the work done by ORNL in 2020 (Gandha, et al. 2020) and those for N40 grade magnets were chosen from Altair’s material library.

$$\max f(x_{ij}) = \frac{T_{mean}}{20(5 \sum_{i=1, j=1}^{60,4} Mass(x_{ij}) + M_{const})} \begin{cases} T_{mean} \geq 20.48 \text{ MNm} \\ B_{max-rotor} \leq 2.03 \text{ T} \end{cases} \quad (2.1)$$

**Table 5. Material Combinations Used in Topology Optimization**

Region	Units	Rotor Core				Magnets	
Design		Single-Material Design		Multimaterial Design		Multimaterial Design	
Material		Baseline Material 1	Material 2	Baseline Material 1	Material 2	Baseline Magnet 1	Material 2
		Fe3Si	Air	Fe3Si	Soft magnetic composite	Sintered magnet, N40 grade	Polymer-bonded, zero Dy
Saturation flux density, $B_{sat}$	T	2.03	0.001	2.03	1.71	-	-
Mass density	Kg/m <sup>3</sup>	7650	1.225	7650	6810	7400	5150
Relative permeability	-	16615.3	4pE-07	16615.3	80	1.066	1.11
Remanence, $B_r$	T	-	0.001	-	-	1.28	0.98
Resistivity	Wm	4.4E-07	1.5E+13	4.4E-07	125	1.6E-6	1.6E-6
$x_{ij}$	-	1	0	1	0.88	1	0.695

Table 6 and Table 7 present the main results of optimization from MADE3D-AML™, which took substantially less time than the conventional approach to optimization. *Single-material optimization* for the rotor core resulted in a double-staircase pattern with lesser material in regions of very low magnetic flux loading with up to 14-t reduction in mass. The rotor flux loading was found to increase with the potential to increase the core loss and heating, which can be circumvented by the new airways introduced by the cavities. *Multimaterial designs* for the rotor core using a combination of soft magnetic composite and Fe3Si steel presented a new way to benefit from both low-loss and higher saturation flux density, although the extent of weight reduction from the rotor was limited to 2 t because of a relatively small reduction in mass density with soft magnetic composites. The hybrid combination of sintered magnet and printed Dy-free polymer-bonded magnet showed marginal weight reductions up to 1.1 t. Assuming that the baseline magnet costs \$60/kg, and Dy-free printed polymer-bonded magnets cost \$36.6/kg, a partial substitution of the baseline magnets with Dy-free magnets will help save magnet material costs by up to 8.75%. With the highest total mass reduction of 15.1 t from the rotor core and magnets, several new optimized rotor core designs were also identified as part of the

optimization using MADE3D-AML™ for the given optimization targets (see Table 5). However, at the same time, several designs were also identified to be practically infeasible (see Figure 12).

### 2.1.2 Opportunities

The following new opportunities were identified through MADE3D-AML™

- MADE3D-AML™ was up to ~400 times faster than conventional regression-based approaches to training, fitness evaluations, and optimization. The performance predictions from MADE3D-AML bore a close resemblance to results from FEA, precluding the need for FEA for future design, which is expected to greatly accelerate the design and materials discovery process.
- Although the extent of weight reduction potential was similar between MADE3D-AML™ and the conventional approach, MADE3D-AML™ was able to identify several optimal designs (see Figure 13) for a given performance target through advanced design space exploration. Thus, machine learning was able to significantly expand the design space.
- Multimaterial designs using a combination of high-saturation Fe<sub>3</sub>Si and soft magnetic composites present a new opportunity to realize low-loss rotor cores. Considering the lower costs of polymer-bonded magnets, the possibility of combining sintered magnets with printed magnets can help use the different magnets in the most optimal regions within the pole and also save material costs by up to 8.75%.
- The rapid evolution of 3D printing technologies with multipowder deposition capabilities can inspire new combinations of magnets that were previously unexplored for direct-drive generators.

### 2.1.3 Challenges

The grid-based approach can result in checkerboard patterns with corner contact (Figure 12) that can be structurally inefficient and practically infeasible to manufacture, even using 3D printing. Further, several drawbacks remain, including the appearance of intermediate material states, jagged boundaries that require extraneous processing before fabrication.

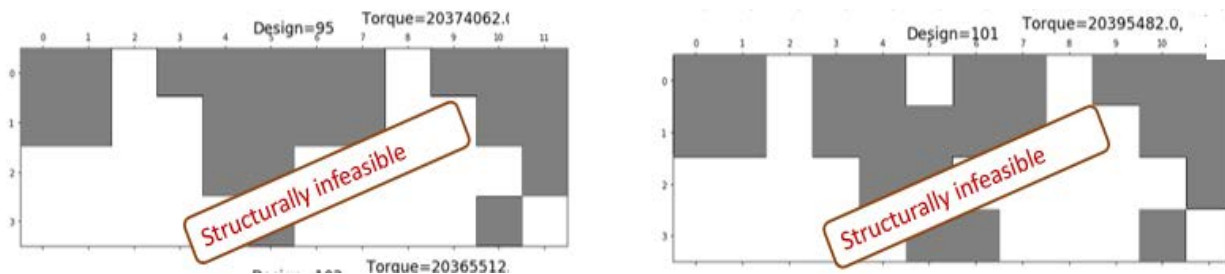
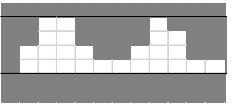
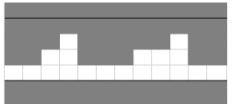

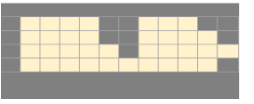
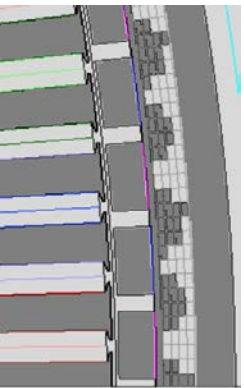
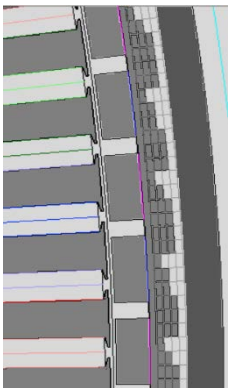

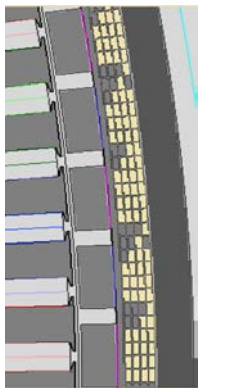
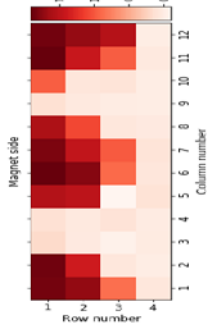
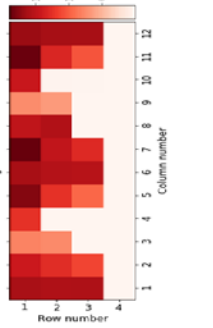
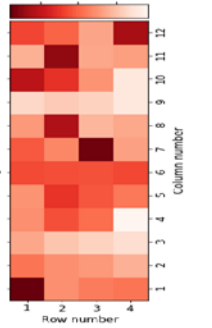
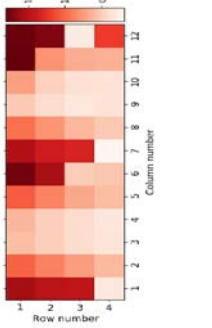




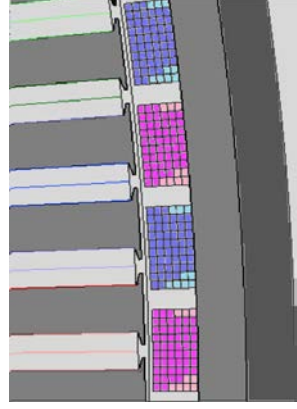
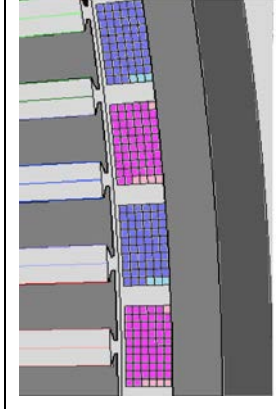
Figure 10. Examples of rotor core designs that were infeasible

**Table 6. Optimized Results for Rotor Core From Regression Model and MADE3D-AML™**

Optimization Region	Rotor Core Single Material		Rotor Core Single Material		Rotor Core Multimaterial		Rotor Core Multimaterial	
Optimization approach	Regression model (RM)		MADE3D-AML™		Regression model (RM)		MADE3D-AML™	
Region								
Representation in the machine								
Rotor flux density contour from MADE3D-AML								
	FEA	RM	FEA	AML	FEA	RM	FEA	AML
B <sub>rotor-max</sub> (T)	1.817	1.903	1.98	1.93	1.88	1.89	1.90	1.922
Torque (MNm)	20.448	20.374	20.469	20.499	20.432	20.45	20.44	20.44

Optimization Region	Rotor Core Single Material	Rotor Core Single Material	Rotor Core Multimaterial	Rotor Core Multimaterial
Time to optimization	5 hours	< 5 minutes	16.4 hours	< 5 minutes
Total rotor core mass (tons)	25	25	25	25

Table 7. Optimized Results for Magnets from Regression Model and MADE3D-AML™

Magnet region				
Pattern representation inside the machine				
$M_{mag}$ (t)	22.98		23.59	
$M_{mag-mat1}$ (t)	20.46		22.476	
$M_{mag-mat2}$ (t)	2.51		1.115	
Material cost savings (%)	8.75		3.88	
Torque estimates (MNm)	FEA	MADE3D-AML™	FEA	MADE3D-AML™
	20.25	20.49	20.49	20.37
Time to optimization	32 hours		<5 minutes	

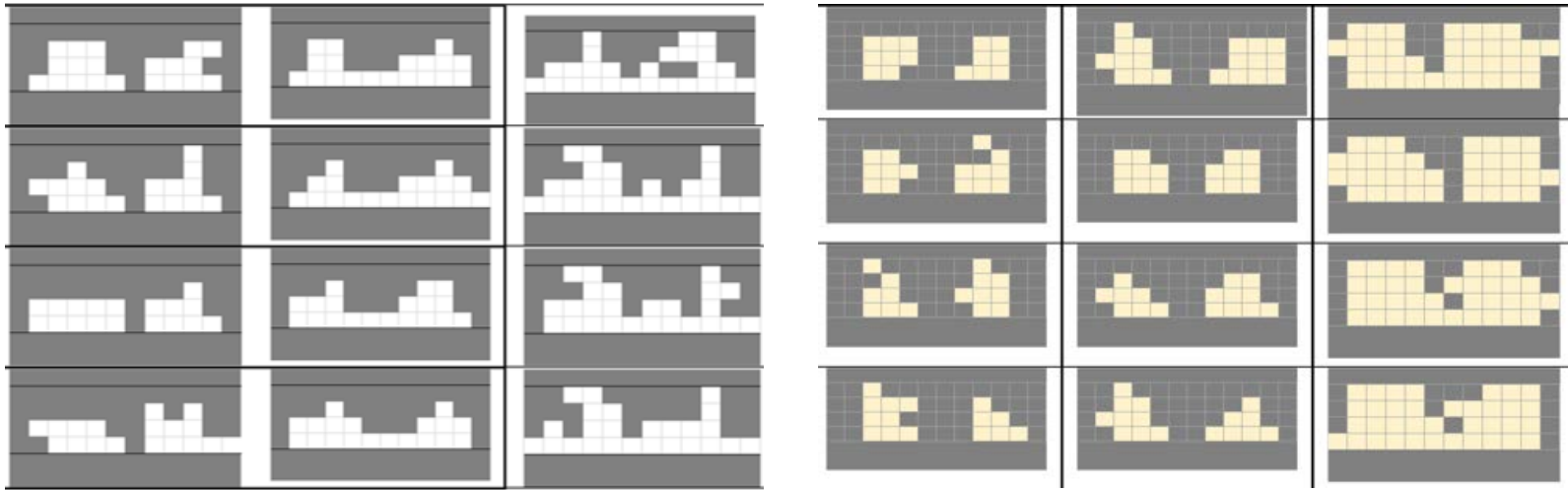


Figure 11. A few additional single-material and multimaterial designs identified using MADE3D-AML™

## 2.2 Development of a Grid-Free Optimization Approach

To overcome some of the drawbacks from the grid-based approach, we investigated a grid-independent boundary optimization where the outer shape of the regions representing different materials were altered using parametric curves. We chose parametric curves because they offer more degrees of freedom for controlling the shapes of geometries when compared to lines and arc segments that are mostly used in designing steel laminations and magnets. However, manufacturing such new shapes using conventional manufacturing can increase the tooling costs and the scrap rate because of the subtractive nature of specialized punching dies and stamping machines. By leveraging SLM printing, it is possible to introduce complex curved geometries in electrical steel manufacturing with substantially reduced waste.

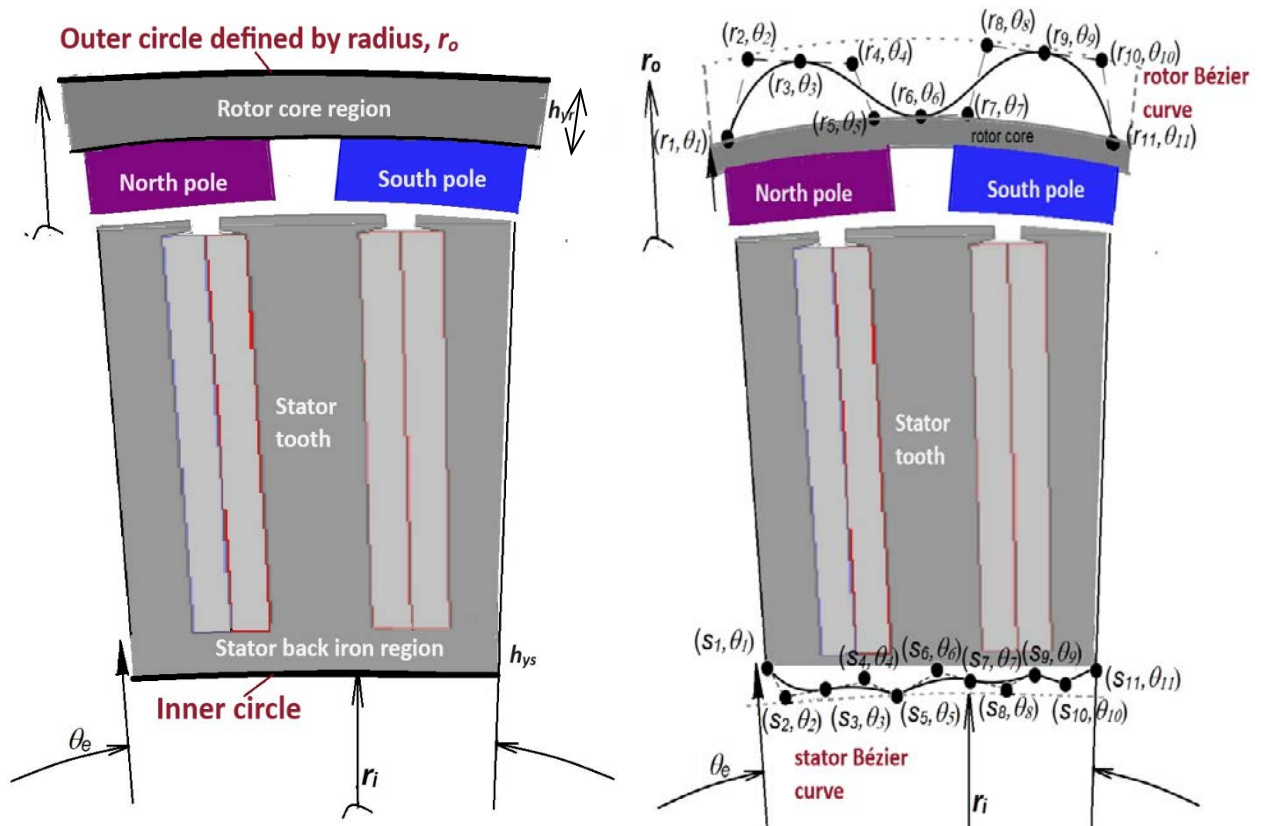
For this effort, we chose to optimize both the stator core and the rotor core for the 15-MW generator. The main design domains for the optimization were the thicknesses of the rotor and stator yoke  $h_{yr}$  and  $h_{ys}$ , and the new results were compared against the grid-based approach. Details of the approach are available in (Sethuraman and Vijayakumar 2022), and a summary is provided here. Similar to the grid-based approach, we considered parameterizing the back iron regions within one pole-pitch ( $\theta_e = 3.6^\circ$ ) using Bézier curves. This included the back iron region behind two poles, and two stator slots for the optimization. The resulting shapes were patterned throughout the circumference.

### 2.2.1 Bézier Curves for Shape Optimization

Bézier curves are a popular class of free-form parametric curves used in 2D graphic applications that allow for easy generation and control of complex shapes. They can be used for shape optimization of geometries featuring complex curvatures such as those used in the design of wind turbine and propeller blades, car bodies, ship hulls, and aircrafts. However, they have not yet been used in the design of electric machines. Considering the advantages of fewer control parameters, mesh independence, and better local control when compared to B-splines or nonuniform B-splines, shapes obtained by Bézier parameterization can be easily manufactured by transferring control points to commercial computer-aided design (CAD) software or 3D printers and can therefore be used in the design of electric machines. Because they present opportunities to integrate parametric CAD-based design, shape optimization, and 3D printing, we investigated the Bézier parameterization for shape optimization of electrical steel in the IEA 15-MW generator.

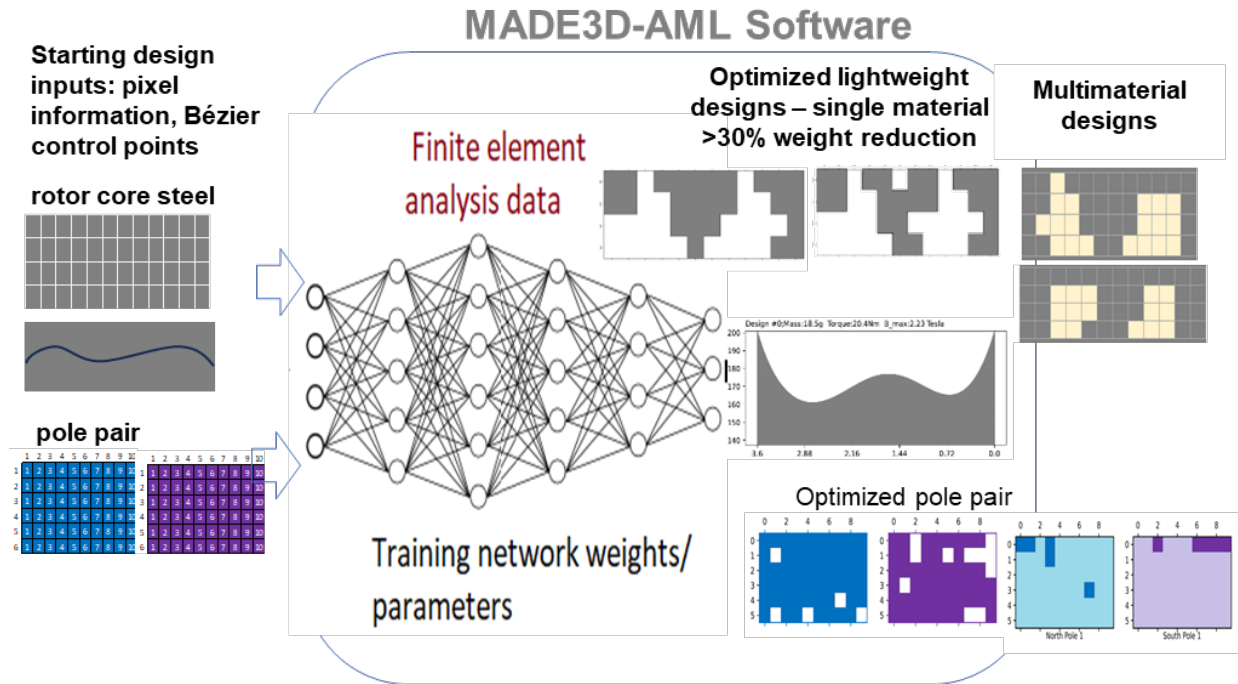
As shown in Figure 14, the boundaries of rotor and stator core regions in the baseline generator model were originally defined using an outer and inner circle of certain radius  $r_o$  and  $r_i$ , respectively. These boundaries were reparameterized using two sets of Bézier curves, each with a certain number of control points. The outer boundary of the rotor and inner boundary of the stator were defined using two separate equations. Each control point represented the radius at a certain angular position. The region within one pole pitch ( $3.6^\circ$ ) was discretized using 11 control points at 11 angular increments such that  $\delta\theta=0.36^\circ$ .





**Figure 12. Parameterization approaches: (a) circular boundaries and (b) Bézier curves**

We first parameterized the rotor boundary using 11 control points with their radius ranging between  $r_o \geq B_1(t) \geq r_g + h_m + 12.00$  over an interval  $t$  in  $[0, 1]$ . These were then transformed to polar coordinates by scaling the position using  $\frac{\pi \theta_e t}{180}$  (where  $\theta_e$  is the electrical angle) and the new radius as  $t = r \cdot \cos \theta$ . Using the bounds, we generated a set of at least 1,000 random Bézier curves using the Latin hypercube-sampling technique available in the PyDOE2 package and constructed the rotor CAD models using the application programming interface capabilities of OpenCASCADE and data exchange features from the pythonOCC project (Paviot 2022). Each resulting CAD model was imported into ALTAIR-FLUX (ALTAIR 2024), assigned the material for rotor region, and then meshed and analyzed by transient magnetic FEA. The design data and results for maximum average air-gap torque and maximum flux density in the core region were used to train a machine-learning-based surrogate model for predicting designs meeting target torque and flux densities in Equation 2.1. MADE3D-AML™ tools (see Figure 15) were augmented to include a separate framework for optimization using Bézier curves. The control points of Bézier curves together with the mass of the resulting geometry and the performance parameters of interest (e.g., torque and maximum flux density) serve as the data on which the machine learning models are trained, and the fitness functions are estimated.



**Figure 13. Framework and capabilities of MADE3D-AML™ software**

Figure 16 compares the results from a single-material optimized design using the grid-based approach with the Bézier-curve-shaped rotor core. Notice that the Bézier curve approach resulted in a similar mass reduction when compared to the baseline but resulted in a smoother, wave-shaped structure. The location of crests and troughs were slightly different from the grid-based design. The process was repeated for the stator back iron, which helped identify a total reduction of up to 20 t from electrical steel alone in the stator and rotor.

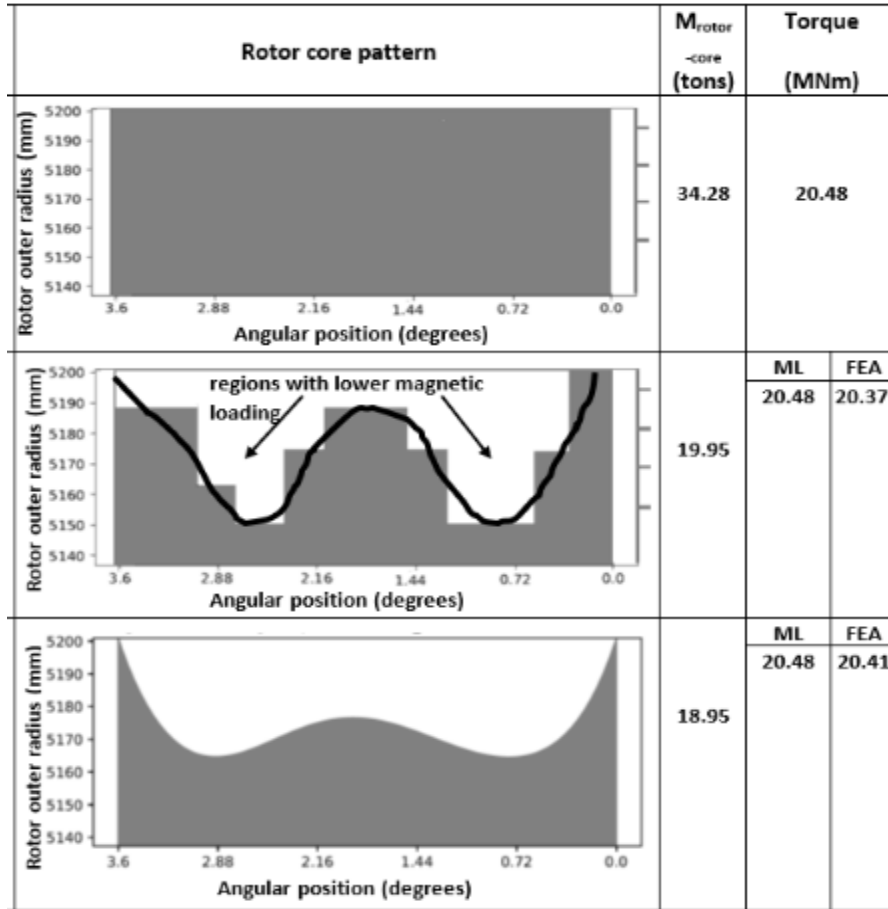


Figure 16. Comparison of optimized rotor core patterns using grid-based approach and Bézier curve approach

Image from Sethuraman and Vijayakumar (2022)

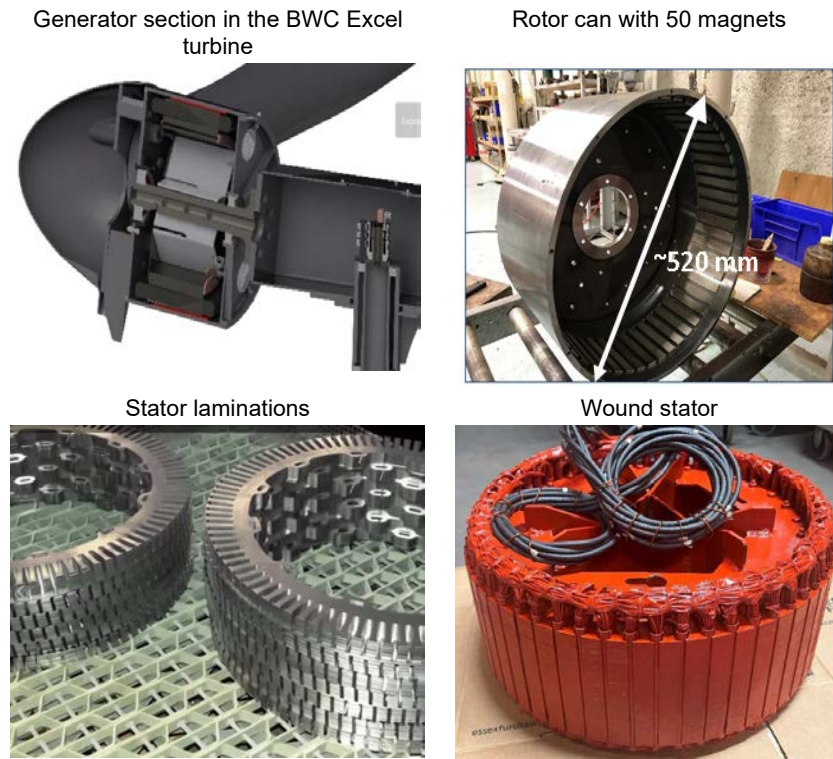
### 2.2.2 Opportunities

Bézier curve parameterization allows for greater flexibility in material placement and can act as intrinsic filters to smooth out jagged and zigzag shapes. They are also convenient to use, especially with integrating complex geometries and different materials, and can be easily applied for multimaterial designs that can be read by commercial 3D printing software for fabrication. The method can be extended to multiple elements, including magnets and stator teeth as well as structural parts, considering thermal and structural domains of the problem as well, which had not been investigated thus far.

## 2.3 Design Space Exploration in a Commercial Direct-Drive Generator

Considering the new opportunities in exploring design freedom identified by shape optimization, we chose to implement the method using a multiphysics approach for a 15-kW commercial direct-drive machine to do a full exploratory search. The goal of the design space exploration was to identify new, better-performing designs that used less magnetically active material and were thermally and structurally feasible at the same time. We sourced the design specifications for a commercial 15-kW generator from Bergey's prototype design borne out of the

Competitiveness Improvement Project<sup>2</sup> (Bergey 2021), see Figure 17 and Table 8. The generator features an outer rotor–inner stator configuration with 50 surface-mounted poles and 60 slots. It has a double layer of concentrated windings and N48H grade sintered magnets with no dysprosium, and the magnetic circuit design was updated to reduce cogging (for startup and vibration), improve efficiency, and reduce steel and copper.



**Figure 17. 15-kW Bergey generator designed for Bergey's Excel turbine**

---

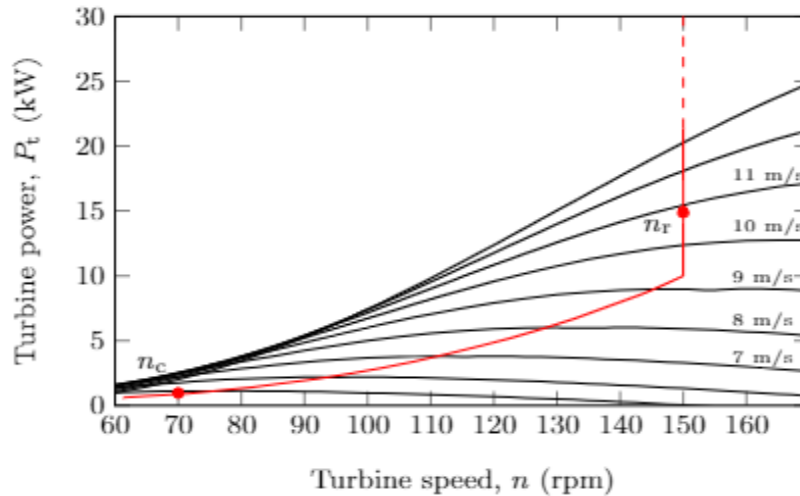
<sup>2</sup> Managed by NREL on behalf of the U.S. Department of Energy Wind Energy Technologies Office, the Competitive Improvement Project awards cost-shared subcontracts and technical support to manufacturers of small and medium-sized wind turbines.

**Table 8. Materials and Manufacturing Methods for the Different Parts of the Bergey Generator**

Baseline Generator	Material	Existing Fabrication Method
<b>Rotor</b>	AISI 1020 grade, 24 in. steel pipe	Bergey fabricated this generator prototype in their production facility in Norman, Oklahoma, using a repurposed large-diameter pipe.
<b>Stator</b>	ASTM A677, M-15 grade steel laminations, laser cut (Fe1-3.0%Si)	Bergey worked with a computer numerical control sheet metal punching vendor to fabricate a custom punch for the slot and make segmented laminations. A stator stacking fixture is designed to allow the stator segment blocks to be assembled and attached, using bolts, to the stator support structure. This fixture assures that the tight roundness or radii tolerance required because of the small air gap (~ 0.050 in.) is maintained.
<b>Magnets</b>	N48H magnets with 0% Dy	Magnets are purchased from China, sintered, pre-magnetized, and attached to rotor by 2-part epoxy.
<b>Copper windings</b>	Total of 60 coils. Each coil has 14 turns of 14 AWG wires with dimensions: 180 mm x 20 mm wide with 3 parallel wires.	Bergey winds the coils using a hand-winding machine in 6 coil strings. Each string has 10 coils with 3 x 14 = 42 individual wires whose ends are taped to keep them together and then are removed from the winding machine. Individual wires are stacked randomly to achieve up to a 50% slot fill factor. Square conductors had been tested conceptually to achieve up to a 75% slot fill.

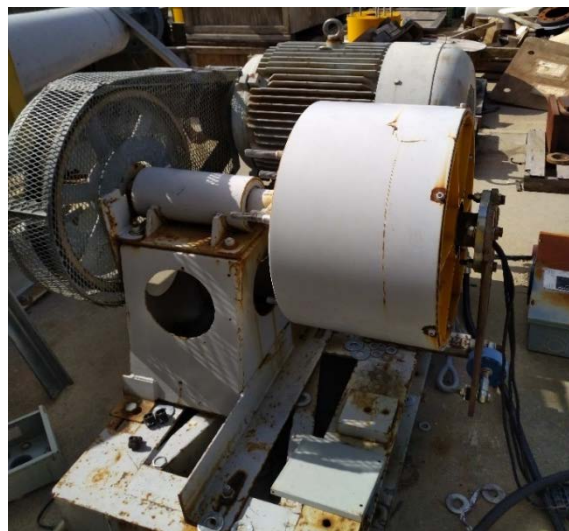
### 2.3.1 15-kW Bergey Generator and MADE3D Targets

Bergey’s Competitiveness Improvement Project generator was designed to generate 15 kW at rated speed and 40 kW for electromagnetic braking during stalling (when the wind speeds are excessively high, the generator creates resistance against the rotation of the shaft by converting kinetic energy into electricity and dissipating it). The generator is connected to a three-phase, diode bridge rectifier with a grid-tie converter. The wind turbine power versus speed curves at various wind speeds are shown along with the generator’s mechanical power curve in Figure 18.



**Figure 18. Turbine speed-power curves at various wind speeds**

Bergey designed the generator using basic parameter optimization to alter the magnet width, alter the tooth geometry to reduce cogging (for startup and vibration), improve efficiency (by minimizing eddy current losses), and reduce steel and copper. They initially tested this prototype value-engineered alternator in their facility on their data acquisition system and a 75-kW dynamometer driven by a variable frequency drive (see Figure 19). They used a resistive load bank and shared their measurements for cogging torque and back-electromotive force with the NREL team. Bergey used a load cell to measure torque and a power meter to measure real power. AC measurements included generator terminal voltage and phase currents during loaded and no-load conditions.

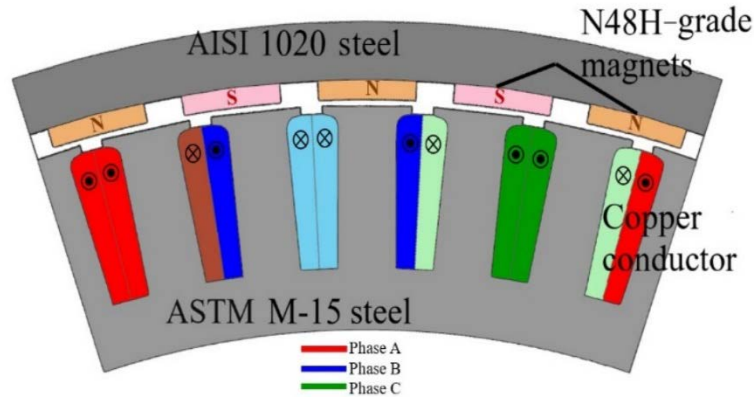


**Figure 19. Bergey's test setup of their 15-kW generator**

Photo from Tod Hanley, Bergey

We used the design specifications, material data and dimensions for the different parts, and test data to develop a 2D model of the machine in ALTAIR-FLUX. As a first step, we verified the accuracy of the 2D model using measurements on back-electromotive force, root-mean-square

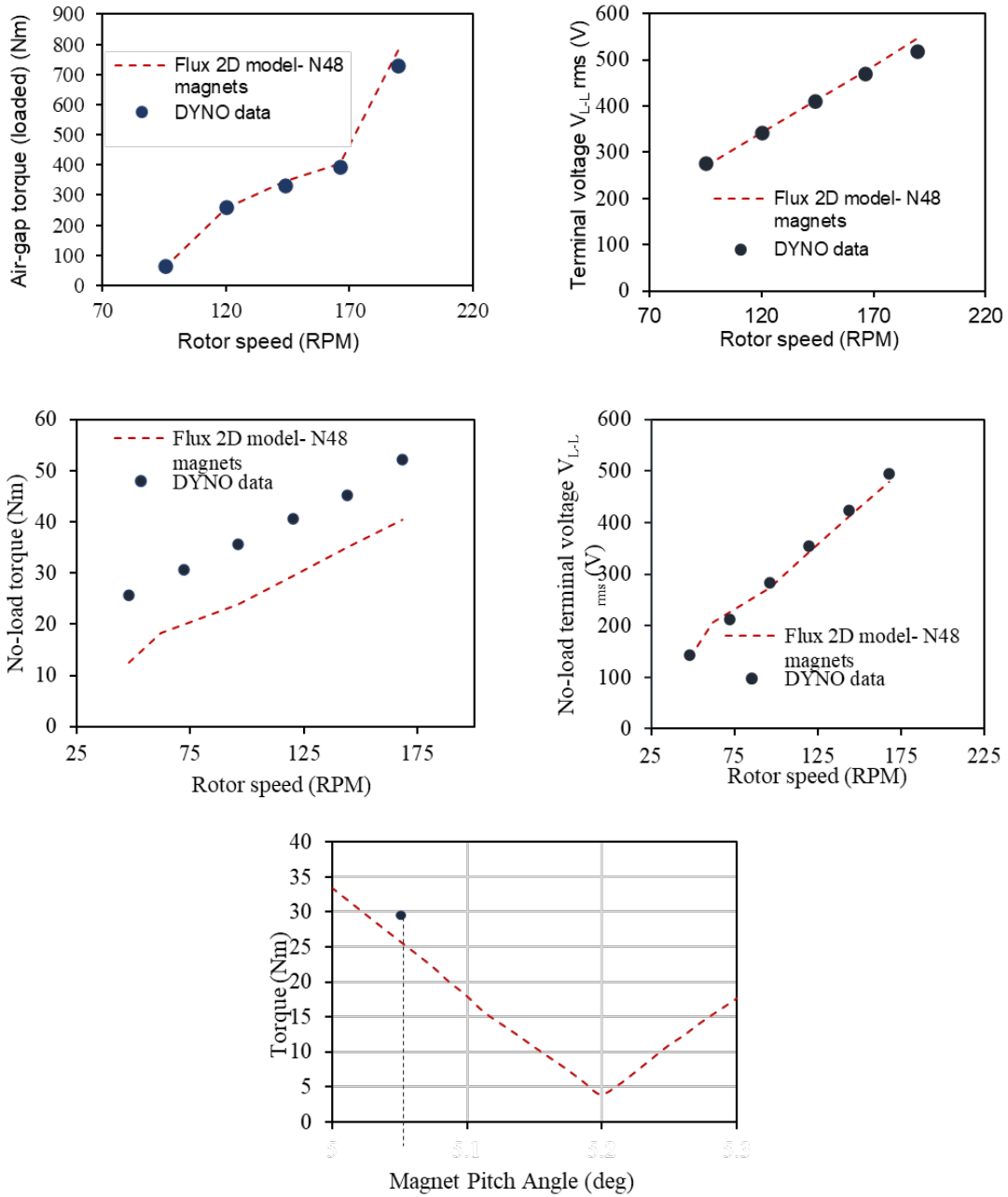
value of phase currents, and the cogging torque and efficiency estimated from Bergey’s tests. Figure 20 shows a one-tenth sector of the generator model in ALTAIR-FLUX.



**Figure 20. A 2D model of a one-tenth sector of the 15-kW Bergey generator**

We performed a transient magnetic FEA analysis to simulate  $3.6^\circ$  rotation of the rotor for a range of speeds from 95 rpm to 195 rpm. Three-phase sinusoidal currents were commutated through the windings, and we extracted air-gap torque predictions and compared them against measured data for the loaded case (see Figure 21). The case was repeated for the no-load case with no currents in the windings, and we also compared the no-load torques against measurements. Overall, the difference between model predictions and measurements was found to be within 10%. The greatest difference was in cogging torque predictions, which we anticipated because friction losses were not accounted for in the model, and this led to a difference of 6–7 Nm. Finally, we compared dynamometer measurements for cogging torque against model predictions for a span of magnet pitch angles. This range is intentionally withheld because the design is proprietary. Measured cogging torque for the designed generator was 33 Nm, whereas model predictions were close to 25 Nm. The model predicted lower cogging torques for higher magnet pitch angles. This was therefore identified as an important opportunity for performance improvement with newer designs.

We chose to retain the targets for design space exploration that were similar to Bergey’s Competitiveness Improvement Project, as shown in Table 9, albeit with less rare earth material (realized using alternate magnet shapes or magnet topologies and printed polymer bonded magnets), less electrical steel, and less conductor material. To begin this design space exploration, we first investigated ideal placement for magnets for the 15-kW generator design that would have a higher potential for optimization using the Bézier curve approach that we developed earlier for the 15-MW generator. At the same time, we implemented a de-coupled multiphysics approach that evaluated the designs from magnetic, thermal, and structural points of view.



**Figure 21. Comparison of model predictions versus measurements**



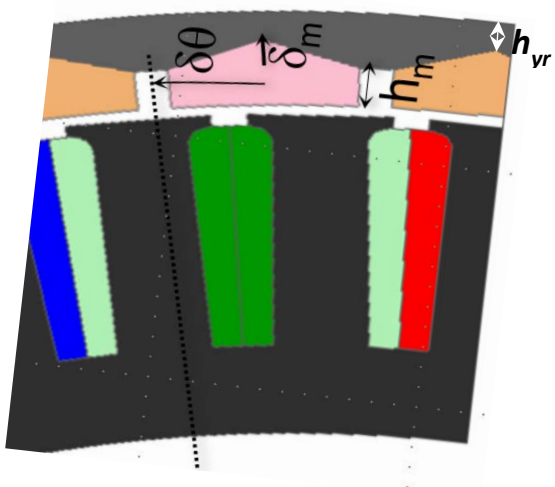
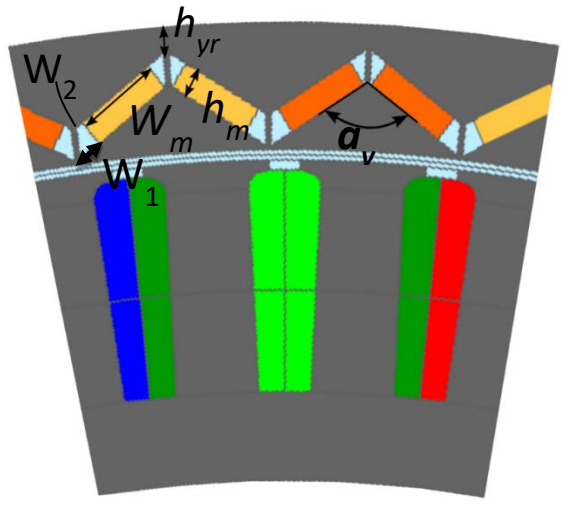
**Table 9. Target Performance Metrics for Advanced Design Space Exploration**

Performance Metric	Target Value
Power output at 150 rpm	15 kW
Power output during stall	40 kW
Target voltage	$\leq 575$ V
Efficiency	95%
Active mass reduction target	At least 10% lighter
Cost reduction target	30% or greater
Maximum magnet temperature	$< 60^\circ\text{C}$
Demagnetization risk	low
Cogging torque	$< 25$ Nm

### 2.3.2 Design of Experiments Using Alternative Magnet Topologies

We investigated two different design variants for the design space exploration: a crown-shaped surface-mounted permanent magnet and V-shaped bar magnets used in interior permanent magnet (IPM) topology. Table 10 shows the parameterization of crown-shaped and V-shaped magnets with simple geometric dimensions and their design bounds. The crown-shaped permanent magnet has a variable thickness controlled using two parameters,  $h_m$  and  $\delta_m$ . The width is controlled by a certain angle,  $\delta\theta$ . The shape of the inner surface of the rotor is controlled consequently in addition to adjusting the thickness of the yoke using  $h_{yr}$ . In the case of V-shaped magnets, the V-angle,  $\alpha_w$ , the magnet thickness, and the width are varied.

Table 10. Parameterization for Crown-Shaped and V-Shaped Magnets

Crown-shaped magnet				V-shaped bar magnet			
							
	Lower limit	Upper limit			Lower limit	Upper limit	
$h_m$ (mm)	2	7		$h_m$ (mm)	3.75	18.75	
$\delta\theta$ (deg)	-0.6	1.0		$\alpha_v$ (deg)	90	175	
$\delta_m$ (mm)	-0.25	3		$h_{yr}$ (mm)	2	20	

### 2.3.2.1 Approach

We used a Latin-hypercube sampling approach for generating the different rotor designs. For this study, we assumed that the generator was connected to a diode-bridge rectifier, and we used an LTSpice model to derive the currents that had to be commutated through the windings. We used a decoupled approach beginning with a transient magnetic FEA, extracting the performance outputs, including efficiency and losses in different regions (heat load) and Maxwell pressure loads in the rotor surface (see Figure 22). We imported the same geometry into a thermal FEA environment along with the losses in the different parts of the machine and estimated the temperature rise. We used the information to estimate demagnetization risk. We also used Maxwell pressure loading to estimate deformation of the rotor ring through structural analysis using Optistruct. We conducted a design of experiments by varying the parameters for each design and analyzed a trade-off between generator efficiency, magnet mass, and magnet temperature, as shown in Figure 23. We applied filters to the results of the design of experiments and extracted rotor designs that lower magnet mass when compared to the baseline generator. We examined three categories of lighter magnet designs: Case I with magnet mass  $< 7$  kg, Case II with magnet mass  $\leq 6$  kg, and Case III with magnet mass  $< 5$  kg. We compared these against the baseline design. We also constrained the cogging torque to be lower than 25 Nm, load torque to be greater than 980 Nm, and magnet temperatures to be lower than 60°C. Both design approaches resulted in designs that met these targets (see Table 11 and Table 12).

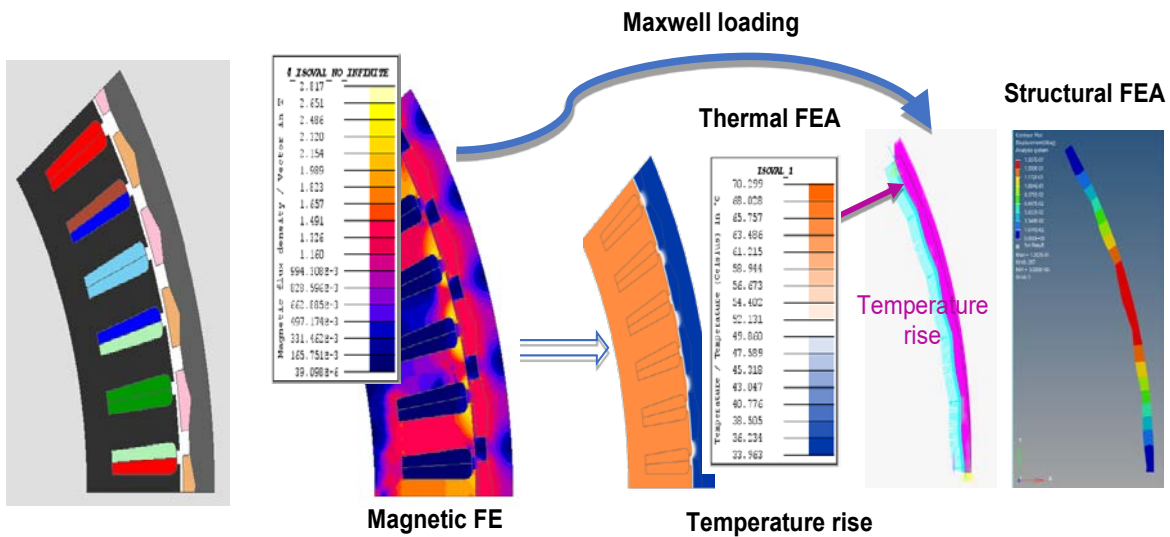


Figure 22. Decoupled multiphysics modeling

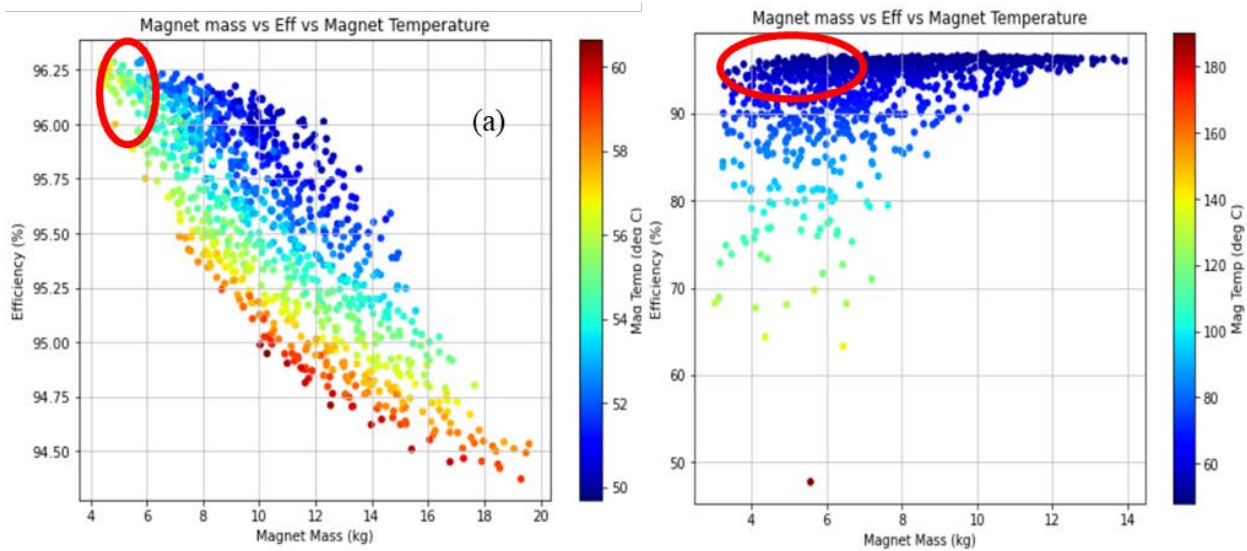
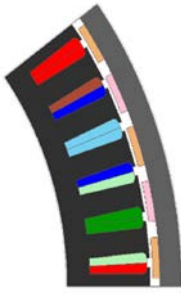
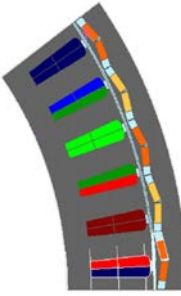
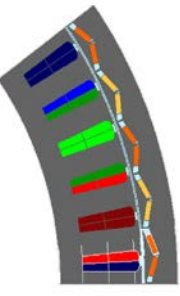
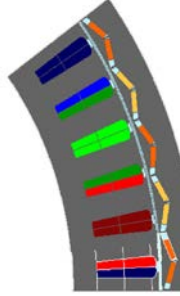


Figure 23. Results from design of experiments: (a) Crown-shaped designs and (b) V-shaped designs

However, the IPM topology had several disadvantages that rendered it less promising for further optimization. The case with a reduction of more than 5 kg in magnet mass did not converge to a meaningful solution, and so no results are reported. We chose the surface-mounted permanent-magnet topology for further exploration using Bézier curves with printed magnets. The results of this subsequent study are presented in three publications (Labuschagne, et al. 2023), (Sethuraman, Glaws, et al., Advanced permanent magnet generator topologies using multimaterial shape optimization and 3D printing 2023) (Sethuraman, Glaws, et al., Advanced multimaterial shape optimization methods as applied to advanced manufacturing of wind turbine generators 2024).

### 2.3.2.2 Advantages and Disadvantages of V-shaped IPM Topology for the 15-kW Generator

**Table 11. Comparison of Optimized Interior Permanent Magnet Designs Against the Baseline Generator**

Quantities of Interest	Units				
		Baseline	I	II	III
Magnet mass	kg	7.381	6% lighter	20% lighter	40% lighter
Core mass	kg	25.32	32.65	41.42	27.67
Power	kW	15.33	14.94	15.0	No solution
Efficiency	%	94.4	96.3	95.6	No solution
Cogging torque	Nm	19.6	6.7	3.8	12.9
Min B <sub>r</sub> (demagnetization)	T	0.714	0.653	0.291*	No solution
Max magnet temperature	°C	58.5	50.0	53.2	No solution
Stator inductance	Millihenries	6.5	13.0	15.0	22.0
Power factor	-	0.7	<0.5	<0.5	<0.5
Radial deformation	mm	0.008379	0.00115	0.002156	No solution
Maximum von Mises stresses	MPa	139.0725	82.656	100.1764	No solution

#### Advantages

- Marginal reduction in magnet mass was possible (up to 6% when compared to baseline).
- The designs resulted in inherently thicker yokes to accommodate the magnets and were structurally stiffer.
- The designs had superior efficiency.
- Substantially lower cogging torques were possible.

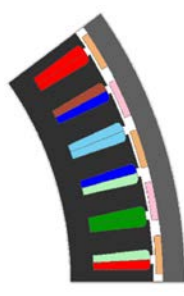
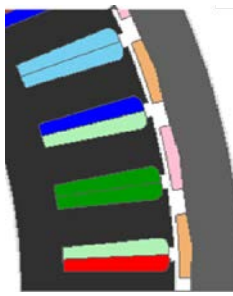
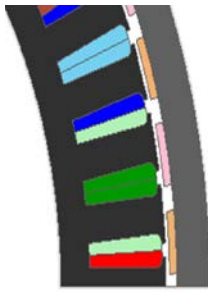
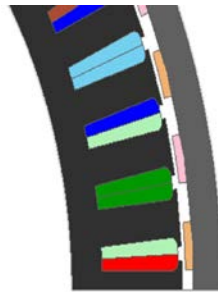
#### Disadvantages

- Requires alterations to stator winding design to achieve similar terminal voltage as baseline. (Number of turns per coil increased from 14 to 18).

- Magnet mass reduction was limited by risk of demagnetization (confined to magnet corners).
- Terminal voltages for all designs exceeded 600 V.
- A reduction of more than 40% in magnet mass results in a substantial increase in stator inductance (the solution may not be feasible to implement on a real system without major changes to the commutation circuit).
- All designs had very low power factors.

### 2.3.2.3 Advantages and Disadvantages of Crown-Shaped Magnets for the 15-kW Generator

**Table 12. Comparison of Optimized Crown-Shaped Permanent-Magnet Designs Against the Baseline Generator**

Performance Metrics of Interest	Units				
		Baseline	Crown 1	Crown 2	Crown 3
Magnet mass	kg	7.38	6% lighter	20% lighter	40% lighter
Core mass	kg	25.32	40.12	25.46	31.86
Power	kW	15.33	14.75	15.36	14.88
Efficiency	%	94.4	94.9	94.5	95.3
Cogging torque	Nm	19.6	8.2	23.97	13.13
Min $B_r$ (demagnetization)	T	0.714	0.691	0.659	0.667
Max Magnet Temperature in °C	°C	58.5	58.9	57.3	58.8
Structural deformation of can (mm)	mm	0.008379	0.01044	0.00676	0.00839
Maximum von Mises stresses	MPa	139.0725	151.289	126.90	138.206
Stator inductance	Millihenries	6.5	6.7	6.7	9.0
Power factor	-	0.7	>0.7	>0.7	>0.7

## Advantages

- Up to 20% reduction in magnet mass possible at comparable performances
- Structurally stiff rotor can
- Similar efficiencies attainable with thinner magnets
- Lower risk of demagnetization
- Possible lower cogging torques
- Power factor  $\sim 0.7$ – $0.8$  (baseline power factor  $\sim 0.7$ ).

## Opportunities

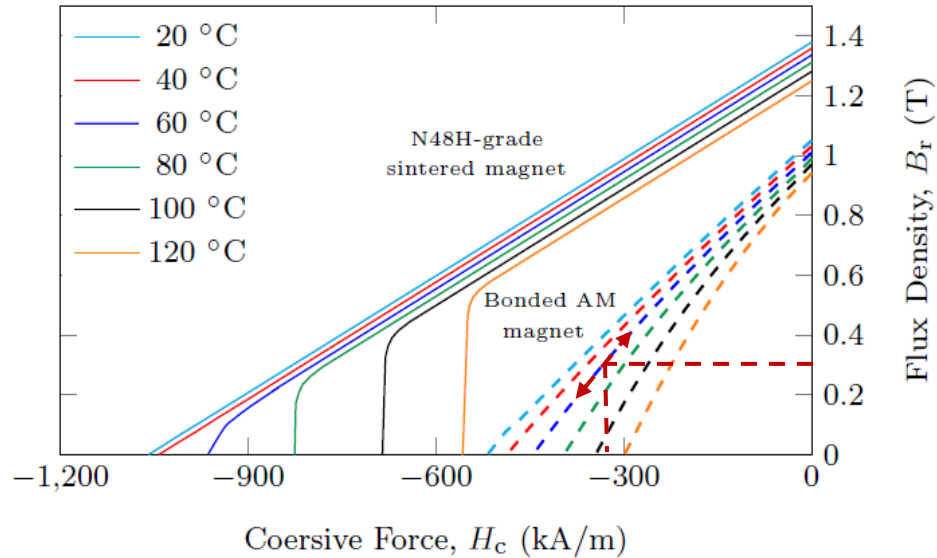
- Required minor change to stator winding design.
- Further shaping by Bézier parameterization can open up new opportunities to preserve the stator design.

### 2.3.3 Exploring Optimization Opportunities With Printed Magnets and Shaping

We first explored the option of replacing the arc-shaped N48H grade sintered NdFeB magnets with printed polymer-bonded magnets assuming a crown shape. We then explored boundary optimization for rotor core, magnets, and stator back iron using novel multimaterial design approaches including asymmetry. An asymmetric approach to designing electric machines is an emerging trend that has the potential to identify new opportunities for improving performance with better use of materials (Lee 2022). As a first step, ORNL measured the magnetic characteristics of printed magnets made from composite powder (NdFeB + SmFeN + Nylon 12) on a variety of samples that ranged from 70 vol% to 81 vol% at temperatures from 300–400 K. We chose a median 75-vol% magnet and linearly extrapolated the characteristics from measurements from 70-vol% samples. We compared these properties against those of N48H grade sintered NdFeB magnets (see Table 13) as well as commercially available injection-molded magnets made from a similar composition of polymer and composite magnets (Sethuraman, Glaws, et al., Advanced multimaterial shape optimization methods as applied to advanced manufacturing of wind turbine generators 2024). The printed magnet has a lower mass density, remanence, and coercivity when compared to the N48H grade sintered magnet. Printed magnets had no clear knee point with the possibility of occurrence in the third quadrant as shown in their demagnetization characteristics (see Figure 24).

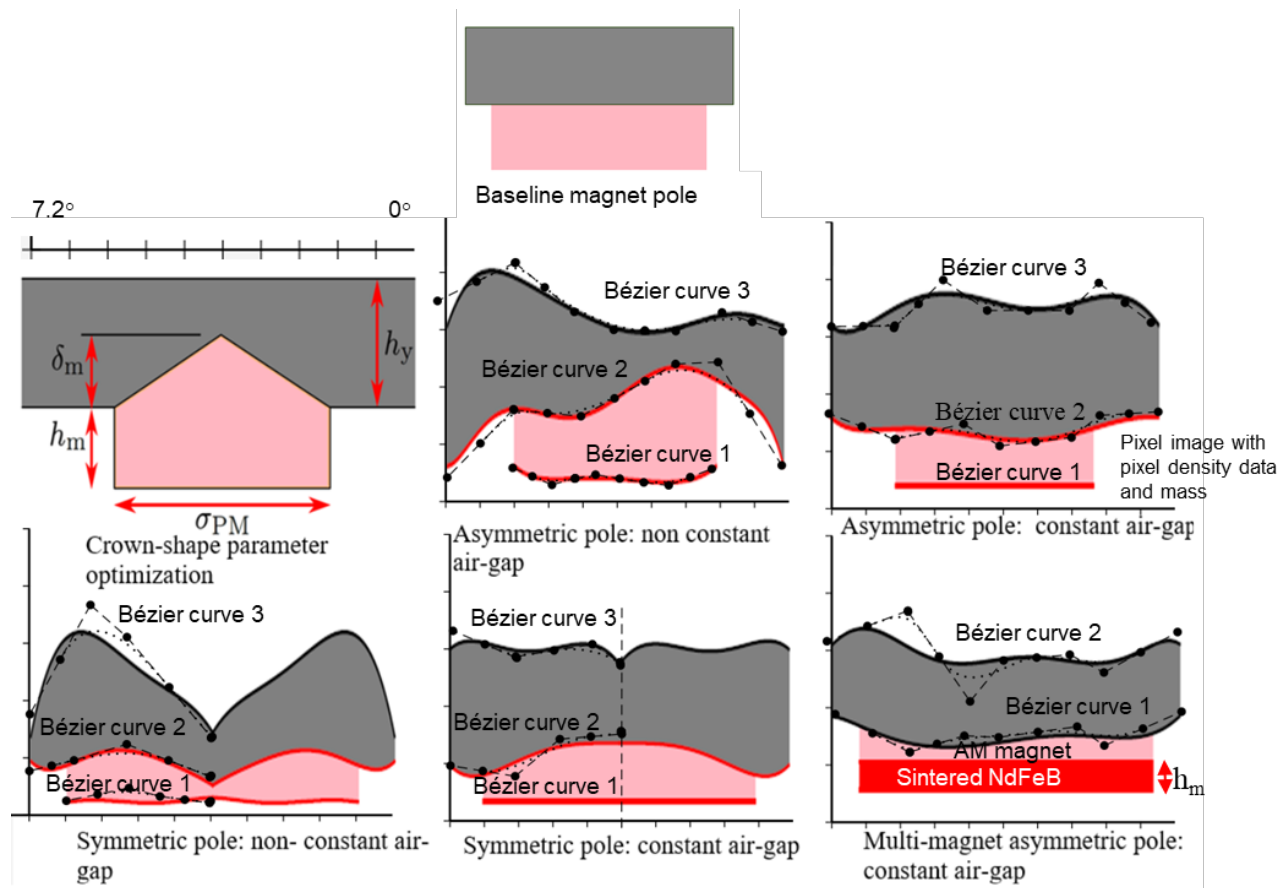
**Table 13. Properties of Baseline Sintered Magnets and Printed Magnets**

Property	Sintered N48H NdFeB	3D Printed 75 vol% MF15P-SmFeN+PA12
Remanence, $B_r$ (T)	1.36	1.03
Intrinsic coercivity, $H_{ci}$ (kA/m)	1041.7	684.2
Energy product, $BH_{max}$ (MGOe)	45	20
Density, $\rho_{mag}$ (kg/m <sup>3</sup> )	7600	6150
Temperature coefficient of $H_c$ (%/°C)	-0.58	-0.61
Electrical resistivity ( $\Omega \cdot m$ )	150E-4	0.170



**Figure 24. Demagnetization curves of printed magnet**

Further, the printed magnets’ near-linear demagnetization characteristics and high electrical resistivity would allow the machine and magnets to operate with lower magnetization at temperatures up to 176.85°C without the demagnetization risk observed with sintered magnets. With an expected operating temperature of 60°C and no clear knee point for the printed magnet, we looked at a range of 0.2–0.4 T and chose 0.3 T as the minimum allowed magnetization. We used these properties to model printed magnets in ALTAIR-FLUX. For the back iron in the rotor, we assumed sand printing of a mold followed by wrought carbon B-grade steel (e.g., A216-grade steel) so that the properties are comparable with AISI 1020 steel used in the baseline generator. The rotor core is functionally both magnetic and structural; therefore, we first focused the optimization on minimizing the magnetic materials, while ensuring that thermal design limits are not violated, and then on verifying structural integrity. We implemented a decoupled multiphysics approach to analyze and optimize the designs in a step-by-step-approach. We ran transient magnetic FEA simulations to verify if the designs generated the target power at the rated speed (150 rpm), and we extracted the losses in the different parts to compute efficiency and heat load. For simplicity, we assumed sinusoidal commutation of the windings. We assumed a fill factor of 75%. Then we simulated two different scenarios: an overload case (that generated 40 kW during stalling), and a symmetric three-phase fault. Both these scenarios were specifically targeted to verify the demagnetization risks for the designs. We used the losses (heat loads) to verify temperature rises in the magnets and conductor regions by transient thermal FEA. Finally, we performed a static structural analysis on an optimized rotor design to verify its structural integrity.

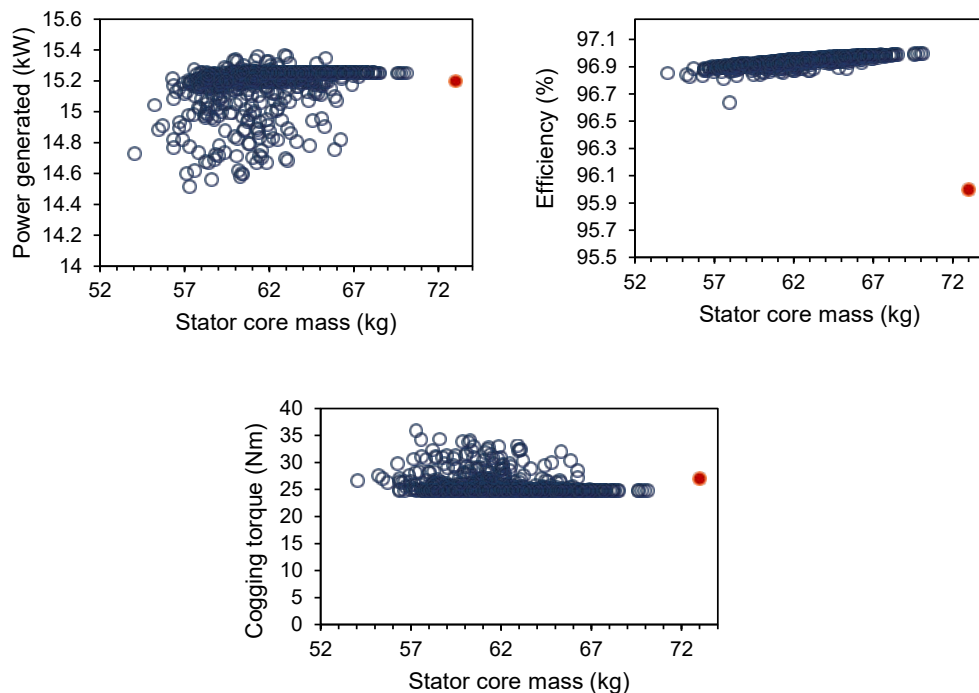


**Figure 25. Different parameterization approaches for the pole**

For the Bézier parameterization approach, we identified five different techniques that allowed for simultaneous control of boundaries of both hard and soft magnets by multimaterial design (see Figure 25). We used the pole pitch angle ( $7.2^\circ$ ) to control the width and shape of the pole using asymmetric and symmetric definitions. As shown in Figure 25, both sides of the magnet—the air-gap side and rear side of the magnet attached to the rotor core—are changed using two sets of Bézier curves (Bézier curve 1 and Bézier curve 2) while the sides of the magnet remained flat. This simultaneously altered the inner boundary of the rotor core while a third Bézier curve (Bézier curve 3) altered the outer boundary. In the case of a symmetric pole design, only one-half of the magnet is controlled using fifth-order Bézier curves (six control points) while the other half is a mirror image. Asymmetric pole design assumed a free-form shape for the entire pole-pitch controlled by three sets of tenth-order Bézier curves, each with 11 control points. Additionally, we chose to keep the air-gap side of the magnet unchanged to explore designs that reduced cogging torque. For the multimaterial magnet pole, polymer-bonded magnets are assumed to be directly printed over a layer of sintered magnet of constant thickness, identified by the variable,  $h_m$ . Two Bézier curves helped alter the shapes of the rotor core as well as the printed magnet. The implementation of these methods along with the mathematical representations in polar coordinates are described in greater detail in (Sethuraman, Glaws, et al., *Advanced multimaterial shape optimization methods as applied to advanced manufacturing of wind turbine generators* 2024). Additionally, we parameterized the stator back iron region using another Bézier curve to explore additional opportunities for mass reduction. We performed multiple



designs of experiments on the rotor designs and identified the most optimal designs for each category after understanding shape sensitivity. We picked the most optimal rotor designs from the design of experiments and used them to further optimize the stator and evaluate the structural integrity of the designs. Figure 26 shows the sensitivity of power, efficiency, and cogging torque to different designs whose stator core mass was varied by Bézier parameterization. The red marker points to baseline design. Back iron shape optimization had the most impact on power and cogging torque; it had minor impact on efficiencies. As a result, we applied filters to constrain these metrics to their thresholds at 15 kW, < 25 Nm, and > 96%, respectively, and identified the most optimal symmetric and asymmetric rotor and stator designs. Table 14 shows the optimized results for the different parameterization approaches, and Figure 27 shows a sector of a machine with asymmetric pole design.

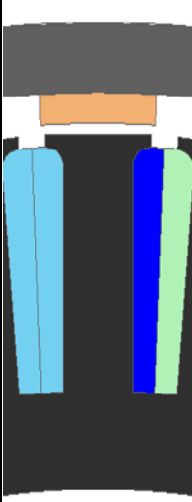

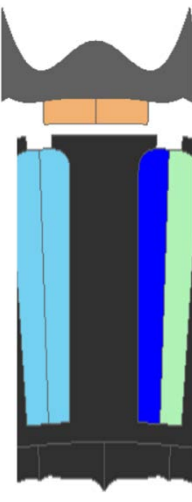
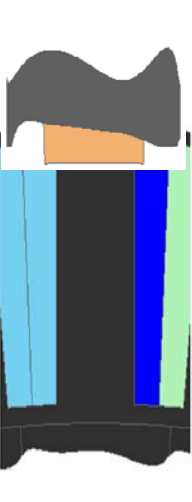



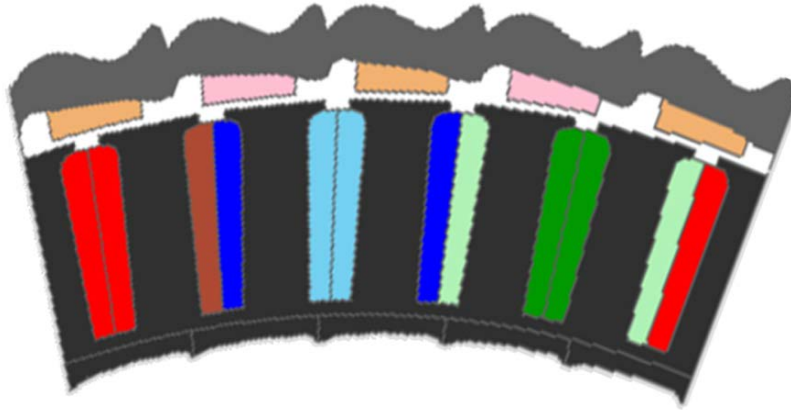
**Figure 26. Sensitivities of generator performance to stator core mass**

Asymmetry allowed for the greatest design flexibility resulting in a 1.94–2.54-kg reduction in magnet mass, whereas the symmetric design approach required more magnet materials for a unidirectional application, such as in wind turbines. This has been possible because of higher reluctance torque because of increased saliency with asymmetry and the use of multiple layers of magnets in a sandwich pattern. The magnet design employing a sintered magnet for the lower layer and a printed magnet for the upper layer leverage the advantages of higher coercivity of sintered magnets and lower eddy current losses in printed magnets. Back iron shaping using symmetric and asymmetric poles helped reduce the electrical steel mass in the stator by 14.62 kg, which was 20% lighter than the baseline stator. The nature of Maxwell’s pressure loading from magnets in an asymmetric pole design is expected to follow the  $B_r$  distribution of the magnet that directly corresponds to the thickness of the trapezoidal magnet. However, because the magnet profile repeats itself on every pole, any asymmetry in pressure loading from a pole will be

counterbalanced by a pole that is diametrically opposite, so there is no net effect due to asymmetric pressure loading.

**Table 14. Results of Optimized Designs**

Parameters	Baseline design	Crown-shaped pole	Symmetric pole	Asymmetric pole	Multimaterial magnet
Design					
Magnet mass (kg)	7.31	6.14	6.00	5.37	4.77
Rotor core mass (kg)	25.32	~26.32	23.08	22.9	26.82
Stator back iron mass (kg)	73.1	73.1	60.16	59.11	73.1
Cogging torque (Nm)	27	24.0	24.28	23.18	24.105
Efficiency (%)	96.1	97.1	96.99	96.88	97.05
$B_{min}$ (T)	0.453	0.3	0.302	0.31	0.5
ratio	71.62	65.8	60.64	60.23	68.97
% magnet mass reduction	-	16	17.95	26.5	24.75

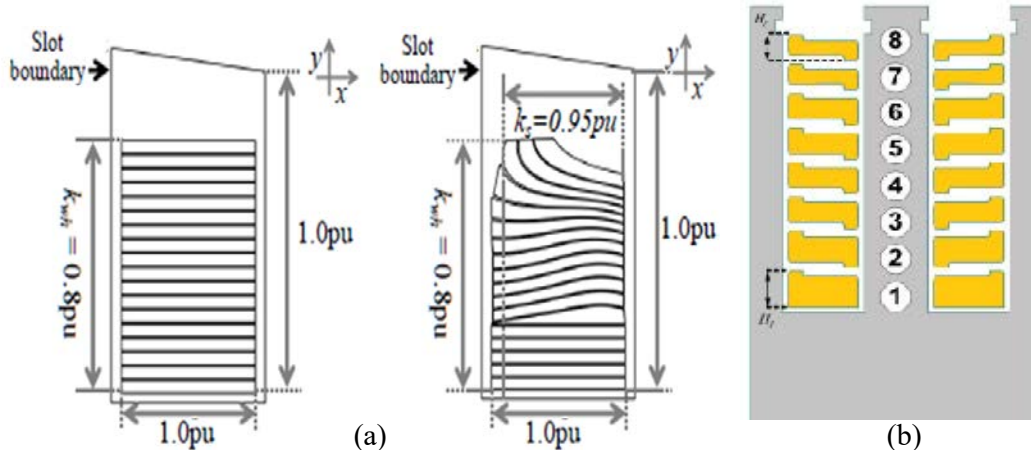


**Figure 27. Optimized asymmetric pole design**

### **2.3.3.1 Stator Conductor Optimization**

We picked the optimized asymmetric, single-magnet pole design (as shown in Figure 27) for exploring further opportunities for weight reduction from magnetically active materials, this time by shaping conductors. The baseline design used 14 turns of three-phase coils wound in a double-layered configuration. Although individual turns were not modeled, each of the individual red, blue, and green regions represented a solid conductor region with a fill factor of 75%. This was assumed to be possible with square conductors. The mass of windings was 28.54 kg. Practically, a very high slot fill (theoretically, 100% fill) would result in the maximum possible output torque of the generator, but such a design has so far been difficult to realize using conventional winding techniques because slot liners and wedges within the slot generally tend to consume some portion of the available space, and winding insulation further reduces the amount of cross-sectional area that can be used for the conductive material. Round wires always leave gaps regardless of their arrangement. With round copper wires, 50%–65% of total slot fill is achievable. Square conductors can achieve higher slot fill, up to 75%, by allowing more conductor material in the same slot and allowing for higher current-carrying capacity. A higher fill factor also implies that less overall material is needed for the same current rating without wasted space, and it helps achieve higher power density. However, square conductors are more challenging to manufacture and have slightly less uniform current distribution compared to round wires.

Multimaterial printing of conductors and insulation offers a new opportunity to overcome these challenges and achieve high slot fills through carefully shaped conductors. However, the effectiveness of high slot filling by printing directly depends on the practically achievable density of conductor material within the slots. This density directly translates to electrical conductivity. With several methods of printing being investigated for printing conductors, efforts to improve electrical conductivities of up to 100% International Annealed Copper Standard (IACS) with copper and aluminum alloys are underway by SLM and extrusion-based techniques such as FFF. SLM-based methods often entail printing conductors first, followed by a separate post-processing step to apply insulation.

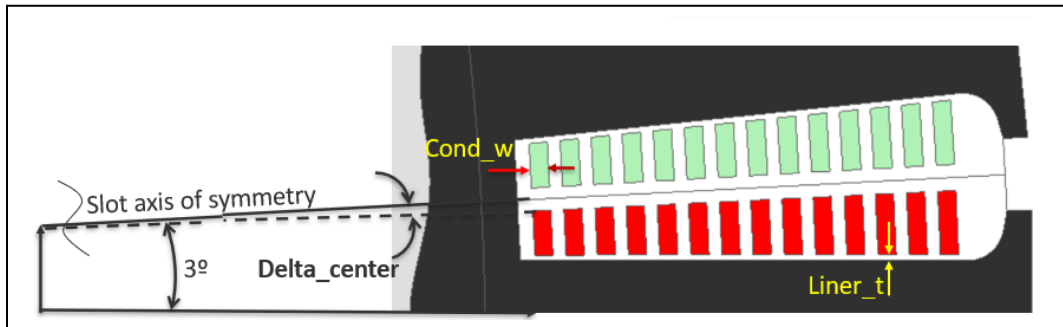


**Figure 28. Conductor shaping leveraging additive manufacturing: (a) Polygon layers and (b) Z-shaped conductors of varying heights.**

Image (a) adapted from Simpson, North, and Collins (2020). Image (b) from Selema, Ibrahim, and Sergeant (2022).

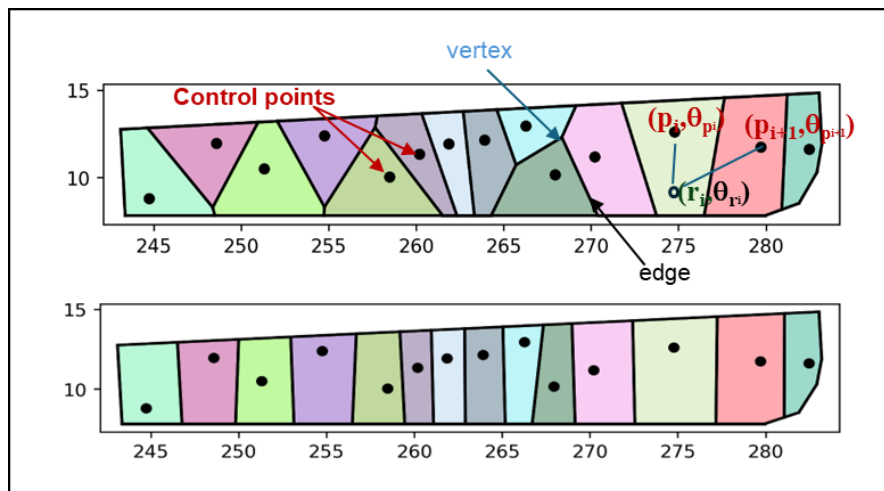
Previous studies have leveraged SLM with conductor shaping to achieve fill factors of up to 78% along with improved thermal conductivity of the windings (ceramics and copper material), reducing AC losses, winding hot spots, and average temperatures in electric machines. Conductor cross sections of each turn have been optimized to reduce the generated losses, allowing for more material to be used in the slot, which reduces the low speed and DC resistance. Figure 28 shows examples of the shape-profiled conductors. A team of UK researchers (Simpson, North and Collins 2020) leveraged SLM-printed copper conductors and a polygon-based shaping algorithm to optimize both single-layered as well as double-layered windings to increase slot fill and minimize AC losses. They used a copper-chromium-zirconium (CuCr1Zr) alloy that had an electrical conductivity of 68% IACS. However, these have been possible with open-slot geometries where the coils in the top layer (near slot opening) were shaped to be parallel with the flux path in the slot geometry to minimize the conductor cross-sectional area exposed to the magnetic flux and minimize losses caused by slot leakage flux. This resulted in a radially asymmetric shape within the slot. The performance of such a design was not verified over a wider range of operating points, and the current density distribution was not uniform because of proximity effects. Selema, Ibrahim, and Sergeant (2022) investigated the use of SLM-produced Z-shaped conductors made of AlSi10Mg with a conductivity of 31.6% IACS. The Z-shape design resulted in 62.4% slot fill factor and featured unequal and asymmetric layer heights to mitigate cross-slot leakage flux and ensure more uniform current densities in the windings. The optimal design featured thicker cross sections in the bottom of the slot and thinner conductors near the slot opening. A comparison of performance of Z-shaped printed conductors with nonshaped, conventional magnet wires with flat conductors (made from commercial-grade copper and aluminum) showed substantially lower AC losses with significantly lower conductor mass. The goal of this effort was to use the full freedom of multimaterial printing and explore better ways of conductor filling in the slots that will also allow for efficient material use, improved efficiency, and lower conductor mass. NREL developed two new approaches to parameterization of stator conductors. Considering each half of the slot cavity as a polygon with rounded edges near the slot opening and gradually tapering thickness at the bottom, we came up with two approaches:

1. Trapezoidal conductors: This approach aimed at achieving  $>70\%$  slot fill using standard geometry—rectangle and trapezium (with majority of fillable area being a trapezium). Each turn in one-half of the slot was parameterized using the trapezoidal region in which the area was controlled using conductor width (Cond\_w), slot liner thickness (liner\_t), and angular distance from center of the slot (Delta\_center). This parameterization is shown in Figure 29. The spacing between the turns was automatically adjusted by dividing the overall fillable length of the cavity by the number of turns. Note that each turn was allowed to be thicker than the neighboring turns, so it was not a uniform change in the conductor cross section. The other half of the slot cavity assumed a mirror image of the turns. We sampled 500 designs that resulted in a range of fill factors from 45% to 72%.



**Figure 29. Parameterization of trapezoidal conductors**

2. Voronoi tessellations: As an alternative to trapezoidal conductors and to achieve higher slot fill, we used the Voronoi tessellation approach that allowed far more variability in the shape of the conductor instead of limiting it to simple geometric variables such as height and thickness of each turn. This was based on the approach designed by the NASA Glenn team for printing insulation sleeves and filling the sleeves by DIW that is discussed in Section 3. The design approach involved a process of subdividing the stator slot cavity according to a Voronoi diagram (see Figure 30). Each subdivision represents a conductor cross section, and the area is based on the distance to a set of control points called seeds, denoted by  $S$ .



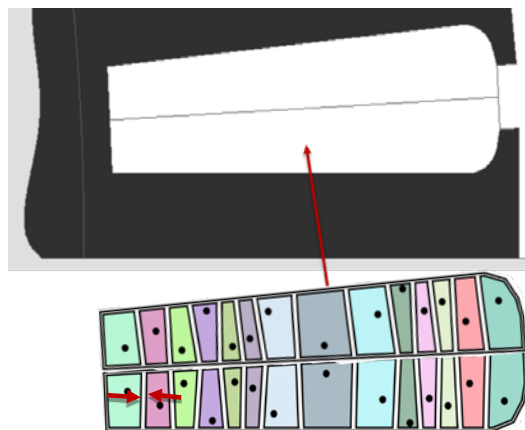
**Figure 30. Sample Voronoi diagrams**

The definition of the distance metric impacts the resulting tessellation and can be used to introduce directional bias. Changing the control points results in different tessellations. The Voronoi diagram can result in more than one region per layer, making the designs difficult to print. Although tessellation fills the space entirely, it is possible to shrink each polygon to add a gap between shapes by either setting a gap size between subregions or target-specified fill factors for design. It is further possible to convert the edges into partitions for insulating medium. The Voronoi region for each seed point,  $s = \{p_i, \theta_{p_i}\} \in S$ , represents a set of all points in the plane closer to  $s$  than any other seed point in  $S$ . Mathematically, the Voronoi region for each seed point,  $V(s)$ , in a given boundary  $B$  satisfies a distance criterion (Equation 2.2) such that for any generic point  $(x, y)$ , the distance between the point and the control point (represented by  $d((r_i, \theta_{r_i}), (p_i, \theta_{p_i}))$ ) is less than or equal to the distance between  $(r_i, \theta_{r_i})$  and any other control, for e.g.,  $s_{i+1} = (p_{i+1}, \theta_{p_{i+1}})$  in the set  $S$  (represented by  $d((r_i, \theta_{r_i}), (p_{i+1}, \theta_{p_{i+1}}))$ ).

$$V(s) = \left\{ (r_i, \theta_{r_i}) \in B \mid d\left((r_i, \theta_{r_i}), (p_i, \theta_{p_i})\right) \leq d\left((r_i, \theta_{r_i}), (p_{i+1}, \theta_{p_{i+1}})\right) \right. \\ \left. \text{for all } s \in S, s_i \neq s_{i+1} \right\} \quad (2.2)$$

Considering these possibilities, we used half the area of slot cavity to define the main outer boundary and used 14 control points (representing 14 turns) to construct Voronoi tessellations. We used the following approach to sample the control points:

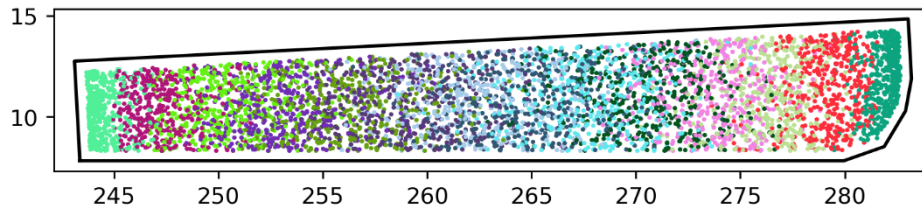
- Sample horizontal distribution of points from exponential distribution
- Locate points vertically within cavity with uniform probability
- Apply variable thickness gaps for insulation that determine cavity fill factor.



**Figure 31. Tessellated slot cavity with directional bias**

Note that it is possible to apply different distance metrics to induce directional bias (i.e., elongated shapes) to achieve a more meaningful arrangement of layers as shown in Figure 31. To sample the control points within the slot cavity, we used a truncated exponential distribution to first obtain the  $x$ -coordinates (see Figure 32). We then normalized the widths against length of cavity. For each  $x$ -coordinate, we uniformly sampled the  $y$ -coordinate by rejecting those that lay outside the cavity. This covered the full range of possible variation in tessellation designs better.

We generated 100 unique tessellations and then reduced them to three different fill factors: 65%, 75%, and 85%.



**Figure 32. Control point sampling**

### 2.3.3.2 Shape and Material Sensitivity by Design of Experiments

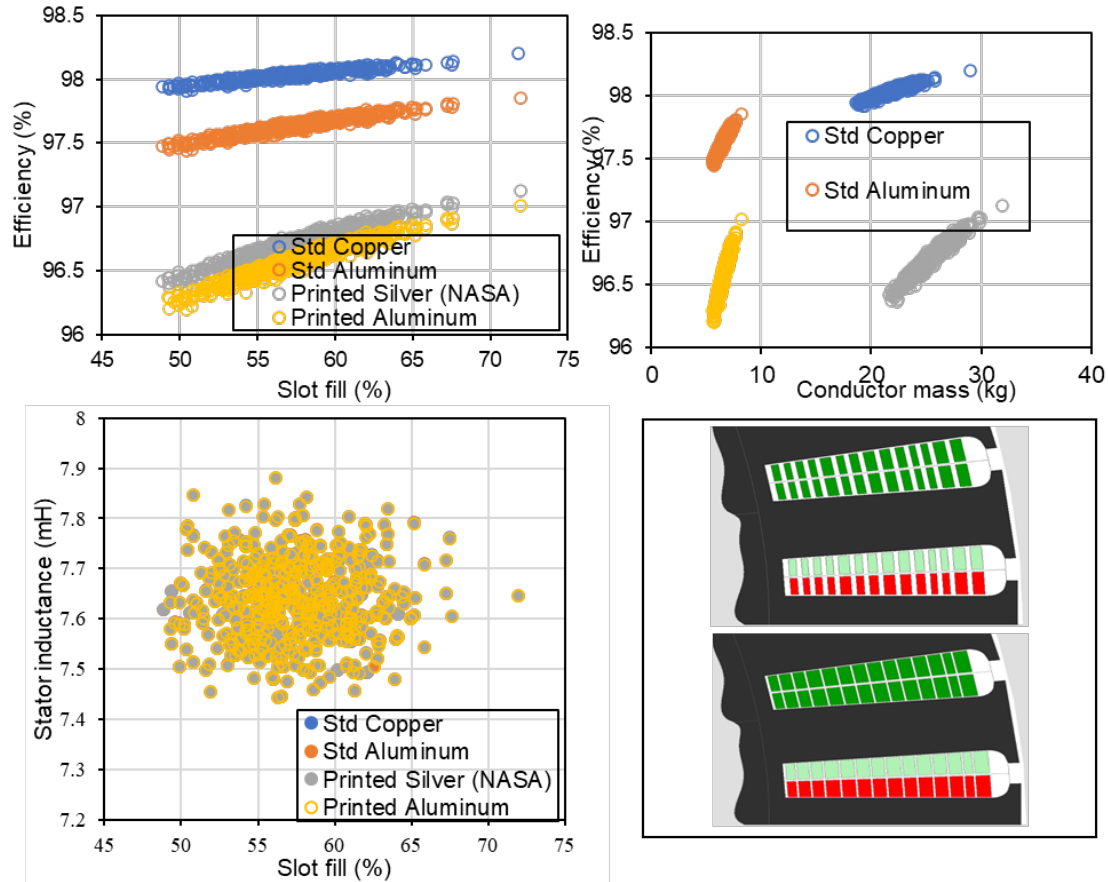
We performed a design of experiments with four different materials (as shown in Table 15), and we analyzed performance sensitivities in terms of efficiency, mass, stall power, and stator inductance variation (see Figure 33). We generated 500 designs. We tested a given design (slot fill) with a certain material by transient magnetic and thermal FEA and extracted the results. We reran the same design with a different material and repeated the process.

**Table 15. Printed Materials Considered in This Study**

Adapted from Selema, Ibrahim and Sergeant (2022) and NASA Glenn’s work on printed silver (Section 3)

Material	Electrical conductivity (% of IACS)	Thermal conductivity (W/m/deg)	Mass density Kg/m <sup>3</sup>	Volumetric heat capacity J/m <sup>3</sup> /deg
Printed copper	100%	394	8,960	3,518,000
Printed silver	33.84%	250.5	10,400	200
Printed aluminum	31.55%	237	2,670	2,429,700
Aluminum	59.4%	200	2,670	2,429,700

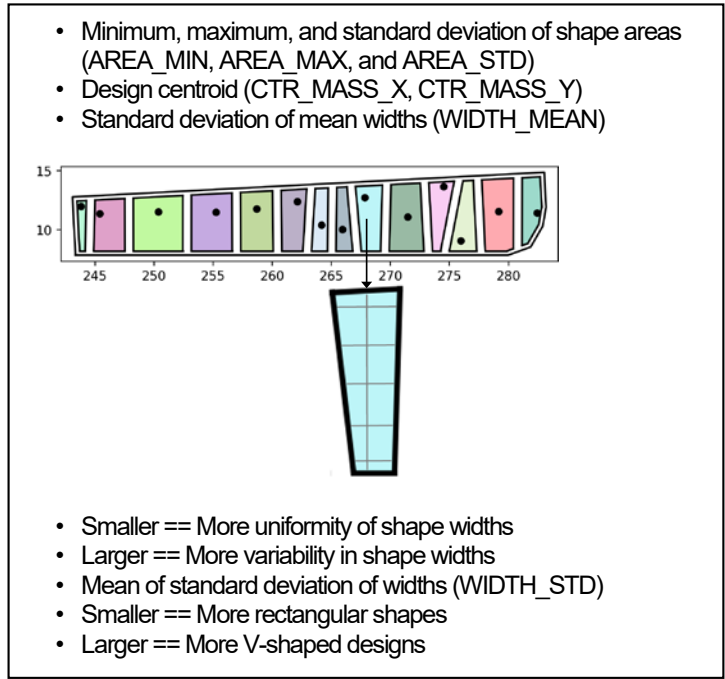
With trapezoidal conductors, fewer different designs with the same fill factor were generated, and we found that the efficiency linearly increased with slot fill factor. Aluminum conductors resulted in the lightest designs. Printed silver designs performed marginally better than aluminum designs. We found no significant variation with stator inductances. Achieving higher slot fills (more than 72%) required additional effort to shape the conductors closer to the slot opening where the geometry included a taper and rounded edges.



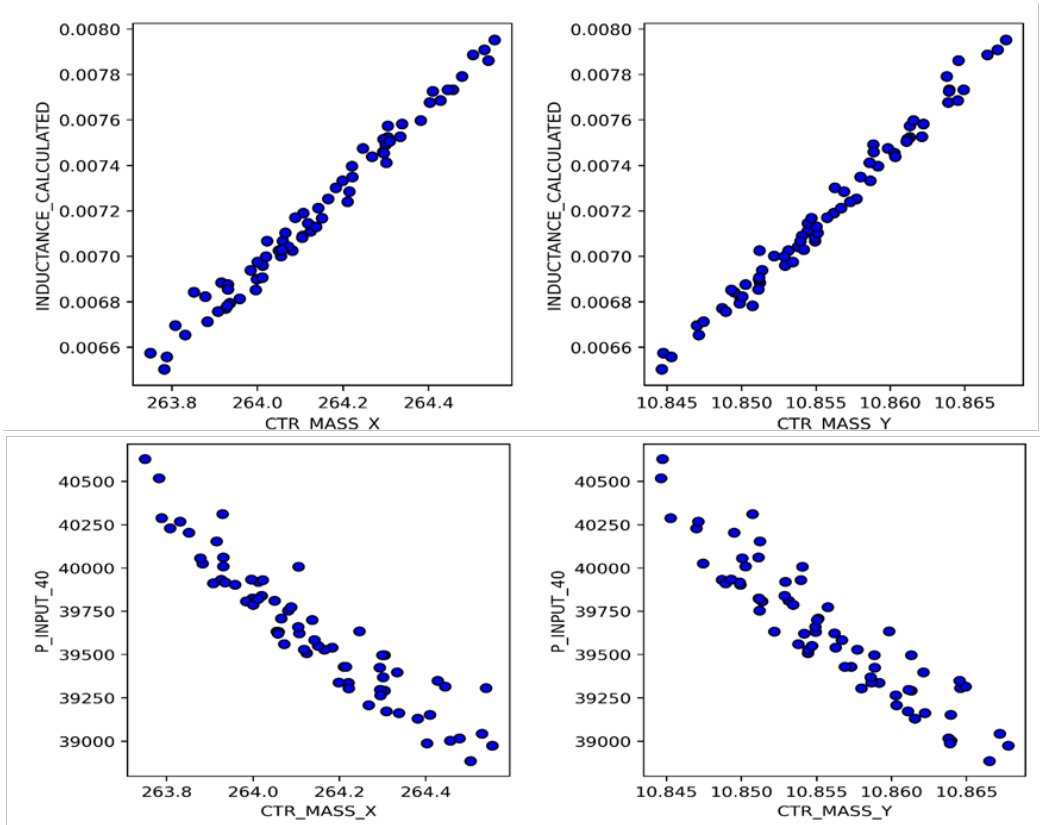
**Figure 33. Sensitivity of generator performance metrics. Bottom right: Designs with lowest and highest efficiency**

The design with highest efficiency was thicker in the middle of the slot. The design with the lowest efficiency had several thin conductors along the slot cavity and fewer thicker ones. With tessellated conductors, several designs were generated for a given slot fill, and each design assumed a different shape distribution for the turns. We identified shape metrics (see Figure 34) to help quantify shape and the influence it had on the generator performance. We partitioned an area vertically and used the distance between the left and right edges to analyze the shape variability. We found that the calculated stator inductance had a strong correlation to the center of mass ( $x$  and  $y$ ) coordinates (see Figure 35). The thicker and more rectangular conductors on the bottom end of the cavity resulted in the highest stator inductances. On the other hand, stall power tended to drop significantly for a similar trend in the center of mass (see Figure 36). Reducing the number of variables to better understand the sensitivities, we generated an active parameter that represented a collective quantification of the metric most responsible for driving changes in performance. We found that higher efficiency needed a higher CTR\_MASS\_X and a smaller standard deviation of areas.

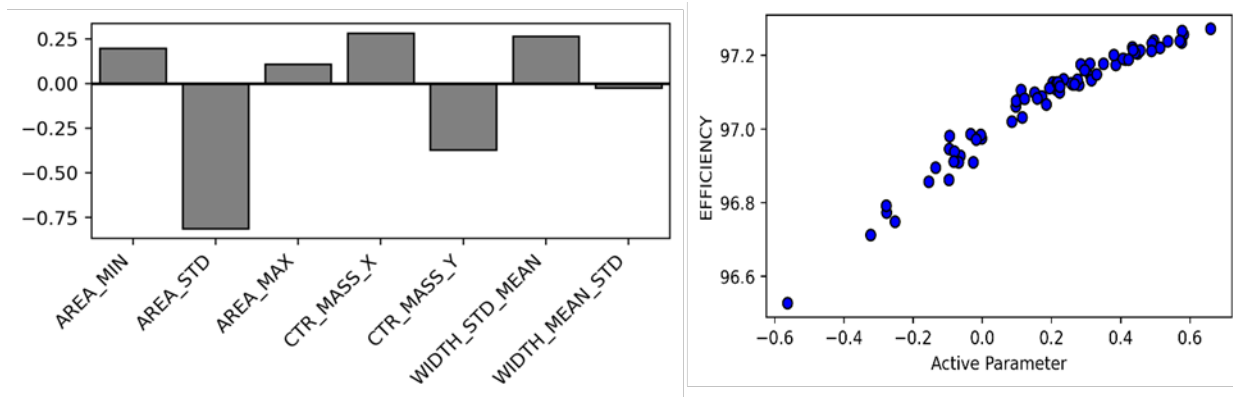




**Figure 34. Shape metrics**



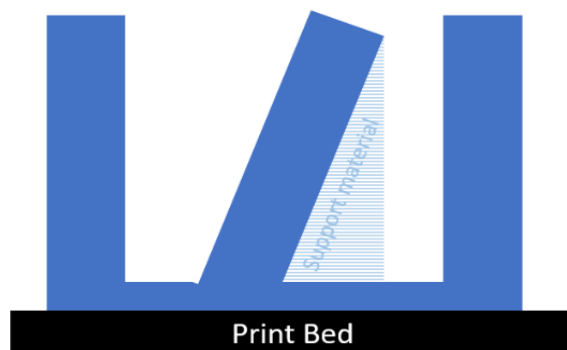
**Figure 35. Sensitivity of generator performance metrics to conductor shape metrics**



**Figure 36. Sensitivity of efficiency active parameters**

Table 16 presents the main results from the conductor-shaping process. The conductors with variable cross sections marginally improved the efficiency of the design. We identified more efficient designs that were lighter than the baseline design for similar fill factor. This suggested that greater standard deviation of cross-sectional areas was needed. The best designs also featured thicker conductors at the bottom and thinner and more uniform conductors at the top. Overall, with printed aluminum, conductor mass was reduced by up to 18.89 kg, which was 66% lighter than the baseline design with copper conductors.

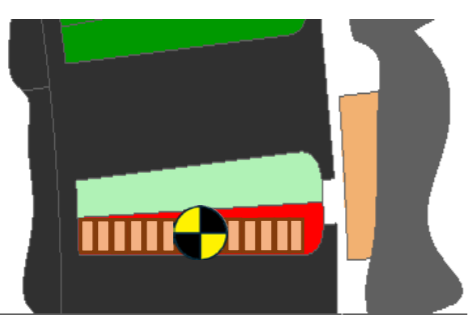
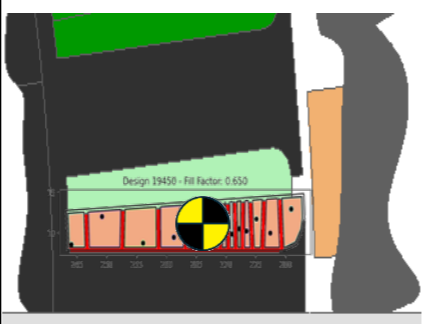
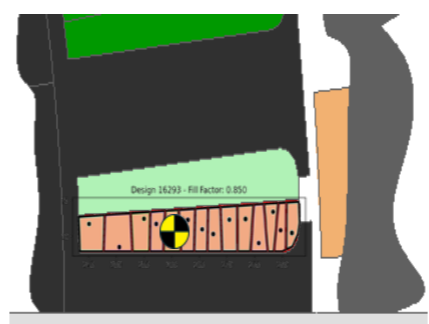
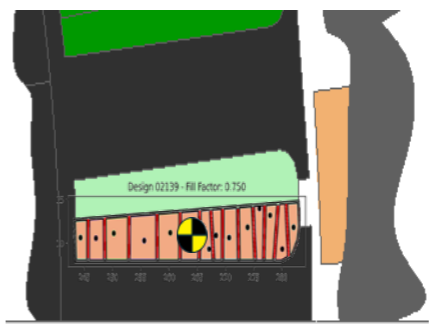
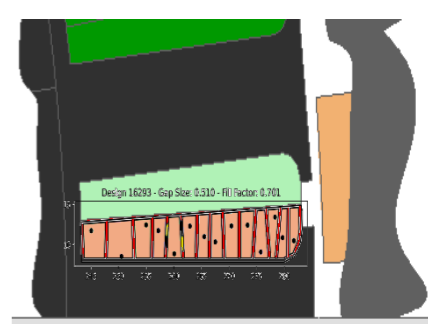
When printing these designs using DIW, the layer walls need to be within the tolerance of the additive manufacturing material and method being used (for example, the insulation layer needs to be <0.02 in. for FFF of polyetherimide (brand name ULTEM)). Also, another consideration is introducing support material to print features that are not vertically touching the bed (Figure 37); while not always needed, support material in FFF can potentially be hard to remove, and the maximum angle of inclination needs to be controlled. Therefore, as a final exercise, we adjusted the best-performing aluminum conductor design for a minimum insulation thickness of 0.51 mm and extracted the performance parameters. This gave 70% fill with a further reduction in conductor mass. The stall power was slightly below 40 kW.



**Figure 37. The presence of support material when printing the insulation sleeve**

Image from NASA

Table 16. Optimized Designs From Using Tessellations

Design metrics					
	<b>Baseline design (magnet optimized) Standard copper</b>	<b>Printed copper 100% IACS</b>	<b>Printed aluminum 31.55% IACS</b>	<b>Printed silver 33% IACS</b>	<b>Printed aluminum 31.55% IACS</b>
Conductor mass (kg)	28.54	24.76	9.65	33.159	7.96
Efficiency (%)	96.8	97.62	97.287	97.10	97.79
Fill factor (%)	75%	64.87	84.83	74.85	<b>70.47</b>
P <sub>stall</sub> (kW)	39.95	39.8	40.00	40.15	39.358
X center of mass (mm)	264.11	263.121	263.85	263.675	263.64
Standard deviation of areas (mm <sup>2</sup> )	0	7.9381	3.5885	4.59265	3.277

### 2.3.4 Structural Integrity and Optimization of Rotor

To verify the structural integrity of a magnetically optimized rotor can, we chose to extrude the 2D geometry of the asymmetric pole design into a 3D equivalent and then analyzed it against the loads it is susceptible to in SolidWorks. The extrusion length was more than the active length of the magnets to provide overhang allowance for the end windings, and the wave-shaped profile on the outer surface was retained for the full extrusion length. With standard disk-type supports used to mount the rotor onto a shaft by bearings, the overhang surface on the inner side was made smoother, and no profiling was considered. Figure 38 shows a section of the generator support structure. We tried to minimize the weight of the rotor structure by varying certain dimensions while also maintaining the necessary stiffness-to-weight ratio to support the blade loads as well as internal forces from the magnets. To minimize impact on maintenance and operation, we did not perform any additional shape profiling or topology optimization on the support structures. We explored the structural design space for the rotor by developing a series of features for the rotor can designed to either reduce mass or increase stiffness and limit the maximum deformations for radial direction, tangential direction, and axial direction to 0.38 mm and 6.35 mm, respectively. The main design variables included the front- and back-plate thickness, radial wall thickness in the overhang region, and the use of radially distributed fins.

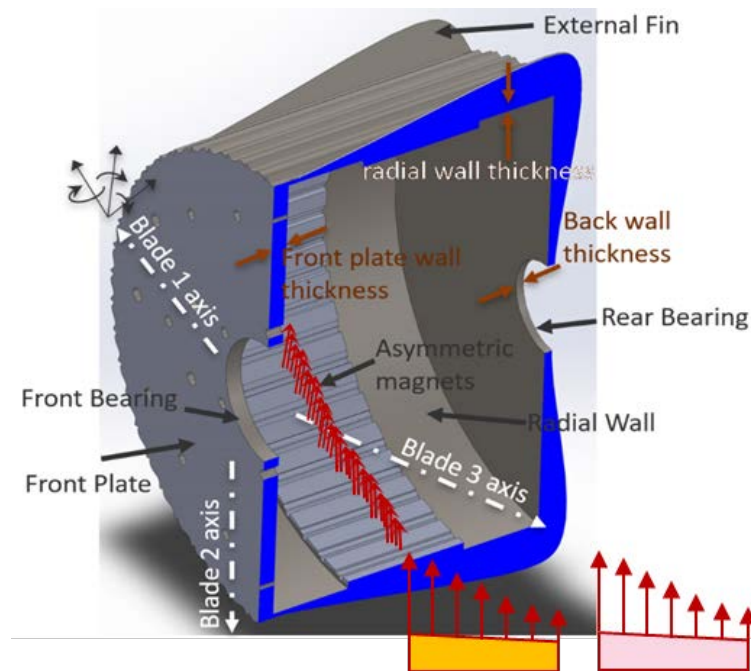


Figure 38. Rotor structure parameters with magnet B, profile

We sampled the values for these variables using a two-level full factorial design of experiments and used the results for mass and deformation to generate a linear regression model that we used to optimize the stiffness-to-weight ratio. Despite the asymmetric nature of pressure loads from magnets, we ignored their effect owing to the repetitive nature of the asymmetry that cancels any imbalance in forces. The support structure design was enforced to be more symmetric because of the asymmetric nature of loading from the blades. Because very little material was removed from the back of the rotor core, and we found that the radial wall thickness had little impact on radial stiffness, minimal weight reduction was possible from the radial wall. Further, the fins did not

significantly increase stiffness; however, they increased the overall weight, and that was counterproductive. The backplate thickness was found to influence the radial stiffness-to-weight ratio as well as the axial stiffness against wind thrust loading. No holes or cavities were introduced in the back plate from the optimization to ensure ingress protection. Table 17 shows the main results from the optimization. No significant material was removed from the active length of rotor core, and up to 13 kg of mass was removed from the front plate, the back plate, and the overhang regions of the rotor. This represented 13% of overall structural mass reduction.

**Table 17. Results From Structural Mass Optimization**

Parameter	Units	Baseline	Realistic	Optimal
<b>Front plate thickness</b>	mm	19.05	12.07	3.75
<b>Back plate thickness</b>	mm	9.525	3.175	3.75
<b>Radial wall thickness</b>	mm	10.312	3.175	3.75
<b>Total structural mass</b>	kg	108.83	95.16	77.4
<b>Radial stiffness-to-weight</b>	—	2,028	1,617.2	1,063.5

### 2.3.5 Summary

We developed three advanced design approaches—a grid-based topology optimization, shape optimization using Bézier curves, and Voronoi tessellations—that leveraged the full design freedom from 3D printed materials using NREL’s newly developed software MADE3D-AML™. The grid-based topology optimization identified up to 15.1 t in mass reduction from electrical steel and magnets in the rotor of the IEA 15-MW reference generator. Shape optimization using Bézier curves for the same generator helped identify an additional weight reduction of 5 t from the stator, thereby meeting the overall optimization target of 20 t from the 15-MW generator. Bézier curves were shown to be a powerful design exploratory tool that resulted in novel, first-of-their kind asymmetric, multimaterial designs with substantial lightweighting potential for a 15-kW direct-drive generator and helped identify new weight reduction opportunities that exceeded the original goal of more than 10% from the magnets. The approach identified up to 2.54 kg reduction in magnet mass, which was 35% lighter than the baseline generator. Shaping the back iron in the stator helped further reduce the electrical steel mass by 14.62 kg, which was 20% lighter than the baseline stator. The use of Voronoi tessellations for profiling the conductors helped identify ultralight printed aluminum conductor designs that were 66% lighter than baseline design yet demonstrated higher efficiency despite their lower electrical conductivity. We finally conducted a structural analysis to evaluate an optimized asymmetric rotor design from the point of view of mechanical integrity and air-gap stiffness. The magnetically optimal shape profile was shown as having a positive impact on the radial stiffness, and we discovered an optimal solution to reduce the structural mass by nearly 30 kg, which was 29% lighter than the baseline. The new advanced methods and novel multimaterial designs proposed in this study significantly expand the opportunities to minimize material use, improve material efficiency, and reduce critical material demand by effective use of material only where necessary. With a constantly changing manufacturing landscape and the rapid evolution of large-scale metal printers, these design techniques can help unlock a world of new design possibilities for realizing next-generation, lightweight electric machines with reduced rare earth material without the risks

introduced from geometric complexities. With wind turbine generators operating in one direction for more than 95% of the time, they may be better optimized for unidirectional operation using an asymmetrical approach that allows for more dimensional freedom and more optimal use of rare earth material (Sethuraman, Glaws, et al., Advanced multimaterial shape optimization methods as applied to advanced manufacturing of wind turbine generators 2024).

## 3 Advanced Processes for Multimaterial Printing of Soft and Hard Magnets and Stator Conductors

Additive manufacturing has the potential to produce novel high-performance wind turbine generators because it enables direct printing of complex shapes and simultaneous processing of multiple feedstocks in a single build. The main goal of this project was to identify scalable approach for materials systems and printers for fabricating novel, lightweight designs for stator, electrical conductors, rotor, and permanent magnets that could be used in large turbine generators (15 MW). As part of the process, specific aspects of multimaterial capabilities using different 3D printing techniques were attempted with the primary goal of minimizing the use of critical raw materials without significantly sacrificing functional performance and also minimizing waste during manufacturing. These processes were developed in two parts. The ORNL team focused on stator laminate printing using multiple alloy compositions with the aim of improving the printability of thinner laminates (up to 0.5 mm thickness) as well as improving their saturation flux densities to meet conventional electrical steel laminate. The team also focused on improving the energy product of printed polymer bonded magnets with zero critical rare earth elements, developing a magnetization fixture for post-print field alignment, and multimaterial printing of magnets and electrical steel with the potential to eliminate the magnet bonding process. The NASA Glenn team led the development of multimaterial printing of conductors along with insulation to improve the coil fill factors and achieve higher power densities.

### 3.1 Candidate Materials for Printing Soft Magnets and Performance Characterization

Based on the detailed literature survey, a list of soft magnetic materials that were suitable for wind turbine generators by some of the available 3D printing methods were identified and are presented in Table 18. Based on ORNL's prior research efforts on electrical steel printing (Plotkowski, et al. 2019) and MDF printing capabilities, the team selected the SLM and BJAT methods to print soft magnetic materials. Wind turbine generators employ several types of electrical steel alloys, particularly Fe-Si alloys (silicon  $\leq 6.5$  wt.%), in their framework. The optimal Si content laminate, Fe-6.5wt.%Si (Fe6Si), is preferred for its high resistivity, relative permeability, zero magnetostriction, and moderate saturation magnetization. However, it is highly susceptible to cracking due to its low malleability, which prevents the traditional production of high-Si-content laminates via cold rolling. Fe3Si is another popular soft magnetic alloy due to its higher machinability via cold rolling, moderate electrical resistance, and moderate saturation magnetization. Typically, Fe3Si laminates are made through vacuum arc remelting of the alloy ingots, billet conditioning, surface graining, hot rolling followed by cold rolling, and stress annealing followed by slitting to the required length for stamping, coating, and stacking. 3D printing can reduce the number of steps for processing these alloys by printing the whole stator in bulk and using electrical discharge machining (EDM) to process the laminates. If we are successful with multimaterial printing in including insulating layers along with Fe3Si, we can also eliminate the need for EDM slicing. Hence, ORNL selected Fe3Si and Fe6Si for printing. Based on the selected approach and composition, the team then fabricated small proof-of-concept stator laminates.

**Table 18. List of Soft Magnetic Materials With Saturation Magnetization and Relative Permeability and 3D Printing Methods.**

Lamichhane et al. (2020)

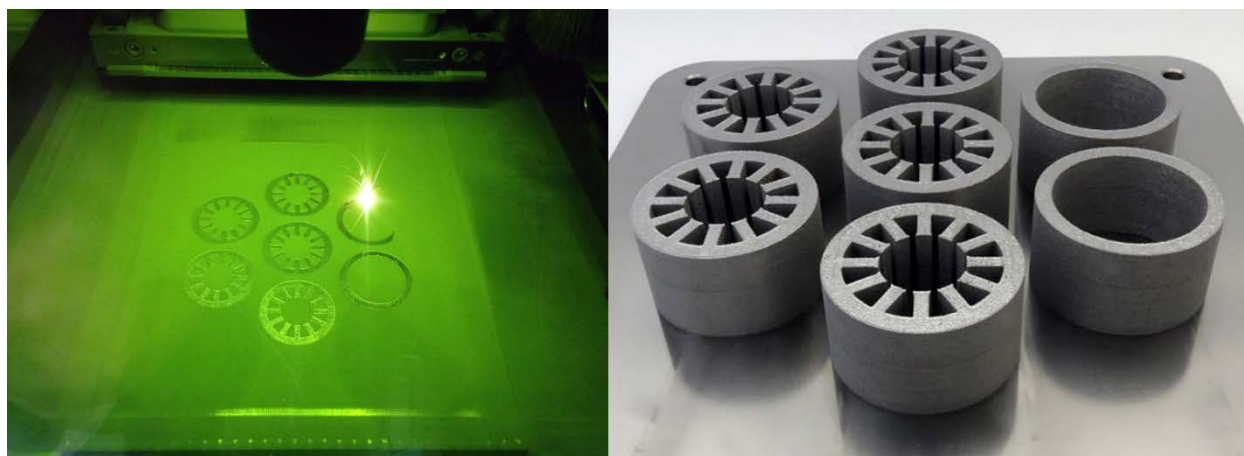
Material Families		Saturation Magnetization $M_s$ (T)	Relative Permeability $\mu_r$	Material Density (g/cc)	Additive Manufacturing Method
<b>Ferrites</b>	MnZnFe <sub>2</sub> O <sub>4</sub>	0.32–0.545	350–20,000	--	--
	NiZnFe <sub>2</sub> O <sub>4</sub>	0.22–0.42	15–2,000	--	FFF
	CoZnFe <sub>2</sub> O <sub>4</sub>	0.103	1.94		--
<b>Fe-Ni based alloys</b>	Molypermalloy (~81% Ni-17% Fe-2% Mo)	0.7	14–550	8.2	--
	High flux (50% Ni–50% Fe)	1.5	14–160	8.2	--
	Permalloy/(Mu-metal) (~80% Ni-20% Fe)	1.08	8,000–120,000	8.2	SLM
	Supermalloy	0.66–0.82	40,000–100,000	8.2	SLM
<b>Fe-Si based alloy</b>	Fe <sub>3</sub> Si	2.15	25	7.34	SLM
	Fe-6.5Si	1.8	10,700	7.3–7.7	BJAT
	Sendust/Super-MSS (Kool M $\mu$ ) 85% Fe- 9% Si-6% Al	1.0	14–125	--	--
<b>Fe-Co based alloy</b>	Permendur (Supermendur)/Hyperco 49% Fe-49% Co-2% V	2.4	20,000–66,000	8.12	SLM
<b>SMC and other soft magnets</b>	Amorphous Iron 20% (Si + B) 80% Fe	1.55		7.18	
	SMC <1% lubrication, Fe balanced	0.71–1.22		7.57	SLM
	FINEMET (glass) ~Fe <sub>73.5</sub> Si <sub>13.5</sub> B <sub>9</sub> Nb <sub>3</sub> Cu 1	0.53–1.24	6,000–100,000	7.18	SLM
	Metglass (Fe <sub>80</sub> Si <sub>9</sub> B <sub>11</sub> )	0.57–.51	20,000–1,000,000	7.29–7.9	*

\*Metglass exhibits ultrahigh permeability due to field annealing.



### 3.1.1 Fabrication of Proof-of-Concept Prototype Stator Laminates Using Fe<sub>3</sub>Si and Performance Characterization

The team initially used SLM to fabricate proof-of-concept prototype stator laminates (as shown in Figure 39). ORNL worked with Arnold magnetics (material supplier) to evaluate printed electrical steel for a small-scale motor design, which was later assembled and tested at Arnold magnetics. This small-scale motor design served as a precursor before evaluating the materials for a larger machine such as the Bergey generator.



**Figure 39. (left) Image of the Fe<sub>3</sub>Si layer being printed during the SLM process and (right) completed build of the seven Fe<sub>3</sub>Si stator samples in a single run**

Fe<sub>3</sub>Si soft magnets were fabricated using a Renishaw AM250 3D printer at ORNL's MDF. Printing was carried out using the CAD models for stator designs of a 12-V motor provided by Arnold Magnetics. The print parameters for the builds are shown in Table 19. The as-printed samples were compressed in hot isostatic pressing at 1,150°C for 2 hours at 200 MPa, with a heating rate of 30°C/min and a cooling rate of 40°C–50°C/min (Plotkowski, et al. 2019). The hot isostatic pressing annealed samples yielded Fe<sub>3</sub>Si parts with densities close to that of conventional parts (7.62 g/cm<sup>3</sup>). The heat treatment relieved the internal stress in the build parts. The stator parts were sliced into thin laminates of 1.4 mm thick using EDM. The team could not go to thinner laminates due to warping. This could be a challenge in printing Fe<sub>3</sub>Si stators using SLM printing.

**Table 19. Nominal Process Parameters for Printing Fe<sub>3</sub>Si Stators Using Renishaw AM250**

Adapted from (Plotkowski, et al. 2019)

Parameters	Values
Power (W)	200
Hatch spacing (μm)	100
Point spacing (μm)	75
Exposure time (μs)	110
Layer thickness (μm)	50

### 3.1.1.1 Mechanical Properties of Printed Laminates

The tensile properties on the SLM-printed Fe<sub>3</sub>Si were measured with an ORNL SS3 standard-sized dog-bone specimen, as shown in Figure 40a, with printed conditions as shown in Figure 40b with average gauge dimensions of 7.62 x 0.889 x 1.651 mm<sup>3</sup>. The mechanical properties were determined at ambient conditions while using a servohydraulic testing machine (MTS Model 810, by Eden Prairie, MN, USA) equipped with hydraulically actuated grips and a clip-on extensometer with a gauge length of 25 mm. All the tensile tests were carried out at a constant crosshead displacement rate of 5 mm/min. The printed Fe<sub>3</sub>Si bulk exhibits a maximum tensile strength of approximately 555.57 MPa, which is comparable to that of conventional parts. The individual yield strength, ultimate tensile strength, and Young's modulus of the samples are presented in Table 20.

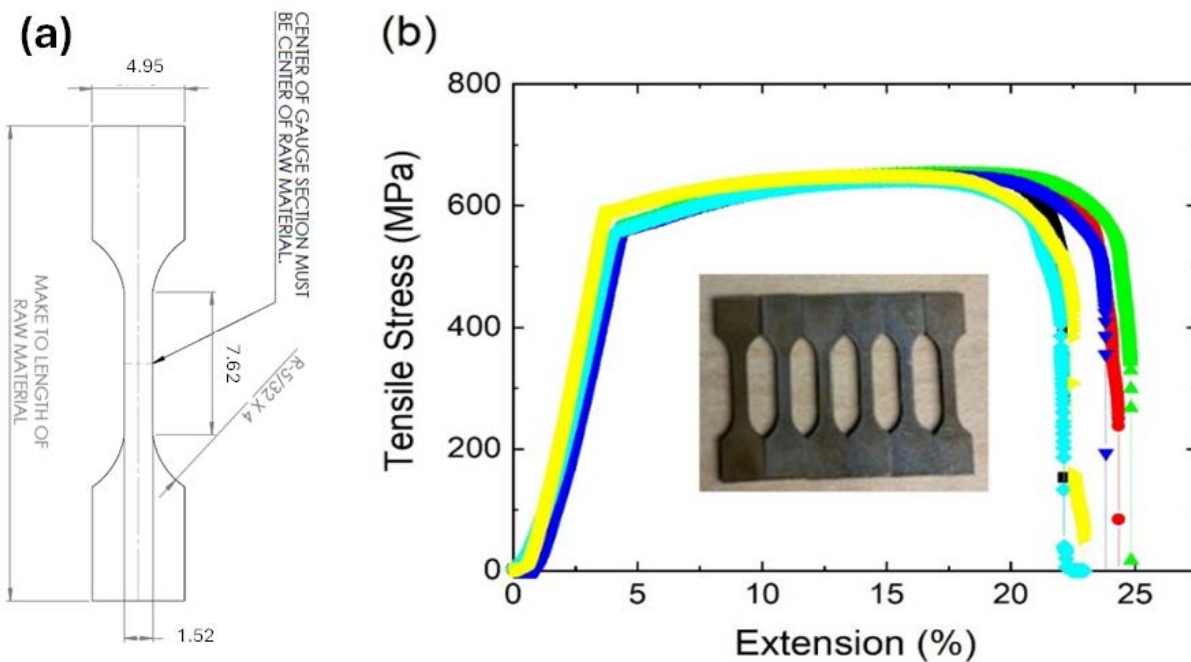


Figure 40. (a) ORNL SS-3 standard sample specification with a thickness of 0.762 mm. for the dog bone samples shown in the inset of (b), and (b) tensile properties of SLM-printed Fe<sub>3</sub>Si

**Table 20. Mechanical Properties of the Fe-3Si Alloy Using ORNL SS-3 Standard Samples**

Sample number	Yield Tensile Strength (MPa)	Yield Tensile Strain (%)	Ultimate Tensile Strength (MPa)	Ultimate Tensile Strain (%)	Young's Modulus (MPa)
1	573.6	2.157	613.5	17.9	29,317.1
2	518.8	2.270	598.7	14.9	25,068.1
3	629.2	2.361	638.3	11.0	29,117.1
4	553.3	2.326	645.5	15.8	26,019.6
5	550.3	2.292	631.9	16.3	26,303.4
6	524.2	2.185	611.5	16.3	26,404.3
7	539.6	2.100	630.5	24.7	27,836.6
<b>Average</b>	555.6	2.200	624.3	16.7	27,152.3

### 3.1.1.2 Electrical Properties of Printed Laminates

The DC and AC magnetic properties of the SLM Fe<sub>3</sub>Si were measured using a superconducting quantum interference device magnetometer at room temperature and compared with data from commercial electrical steel sheets from JFE steel (JFE Steel n.d.). The results are shown in Table 21. Based on the results with SLM Fe<sub>3</sub>Si, 3D printing has the potential to produce stators suitable for wind turbine generators.

**Table 21. Comparison of Magnetic and Electrical Properties of Conventionally Processed Electrical Steel and SLM Fe<sub>3</sub>Si Laminates**

Properties	Units	Conventionally processed steel	SLM-Printed and EDM-cut ring samples
Lamination thickness	mm	0.65	1.4
Measured Induction, B <sub>m</sub> , and Saturation Magnetization, M <sub>s</sub>	T	M <sub>s</sub> : 1.46 to 1.98 (JFE Steel n.d.).	B <sub>m</sub> : 1.72 at 100 Oe field B <sub>m</sub> : 1.57 at 30 Oe field M <sub>s</sub> : 2.1 at higher field
Coercivity, H <sub>c</sub>	Oe	25 to 50 A/m (0.314 to 0.628 Oe) (Eisenforschung 2021)	0.5
Resistivity, ρ	μΩcm	~50 (Bas, Calero and and Dougan 2003)	50
Maximum permeability (nonoriented)	-	3,000 to 9,000 (Iordache and Hug 2009)	7494
AC core loss	(Watts/lb)	4.6 to 9.22 (60 Hz, 1.5 T) at 0.65 mm thickness (JFE Steel n.d.).	~20 (60 Hz, 1.5 T) at 1.4 mm
Tensile strength	MPa	>400	555.57

If the SLM technique is used for individually printing thin laminates, temperature gradients between the different layers can lead to cracking during printing.

### 3.1.2 Evaluation of Multimaterial Printing of Fe<sub>3</sub>Si Steel With Secondary Alloys

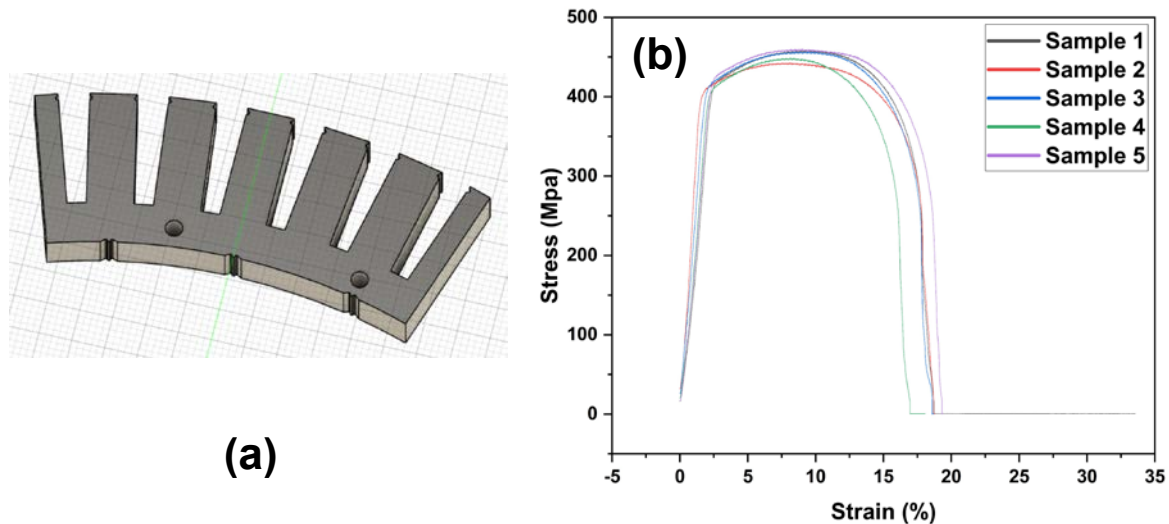
To eliminate the need for EDM slicing and cracking during printing, and reducing the core loss further, the team investigated multimaterial printing of steel with the inclusion of secondary alloys using SLM and using ceramic composites made by the binder jetting technology. Post-annealing of steel fabricated with composite alloys using either approach is expected to reduce the thickness of the laminate significantly, increase the resistivity, and hence reduce the core loss, which can help accelerate the printing process. In addition, this process will also eliminate the need for the conventional stator fabrication process. Multimaterial printing could be achieved in two ways. One way is to premix the feedstock with both conductive Fe<sub>3</sub>Si powders and metal/insulating material powders. This is single-feed multimaterial 3D printing. The other way is to utilize dual-feed 3D printers to print alternating layers of conductive and insulating material. We attempted the first approach using SLM and BJAT using metal and without insulating materials. BJAT was used to fabricate stator laminate using pure Fe<sub>3</sub>Si powders and Fe<sub>3</sub>Si premixed with 1% Al<sub>2</sub>O<sub>3</sub> powders with an ExOne (X-1 lab) machine. This combination is referred to as the ceramic composite and tested on a small coupon (rectangular plate). After printing, the green parts were heat-treated at 200°C for 1 hour in air, then debinded by ramping to 630°C and held at that temperature for 1 hour. Finally, the parts were heated to 900°C for 1 hour in flowing argon gas. These parts were then sintered at 1,300°C for 2 hours under high vacuum. The properties of Fe<sub>3</sub>Si with and without ceramic composites are compared with SLM printed Fe<sub>3</sub>Si samples in Table 22. Nearly full-density Fe<sub>3</sub>Si samples are achieved using SLM. However, 89%–91% dense samples were achieved using BJAT, and the saturation flux density also dropped from 1.8 T to 1.5 T. Further optimization with multimaterial printing is needed to improve these properties.

**Table 22. Magnetic Properties of BJAM Fe-3Si With and Without Al<sub>2</sub>O<sub>3</sub> Composites Compared With SLM Printed Fe<sub>3</sub>Si**

Method	Density g/cc <sup>3</sup> (%)	Saturation Magnetization (T)	Relative permeability, μ <sub>r</sub> at applied field (Oe)	Loss fraction	Laminate thickness achieved
Laser-Fe <sub>3</sub> Si	7.54 (99.28)	2.15	4 (at 305 Oe)	Intermediate	0.35–1.5 mm with EDM
Laser-Fe <sub>3</sub> Si+Al alloy	7.18 (99.0 of multimaterial)	---	---	---	0.5 mm without EDM and post-annealed
Binder jetting Fe <sub>3</sub> Si	6.97 (91.57)	1.6	21 (at 205 Oe)	Lowest	0.5 mm as printed and post-annealed
Binder jetting Fe <sub>3</sub> Si+Al <sub>2</sub> O <sub>3</sub>	6.77 (89.16)	1.5	11 (at 305 Oe)	Highest	0.5 mm as printed and post-annealed

### 3.1.2.1 Fabrication of a Proof-of-Concept Laminate for the 15-kW Bergey Generator

The baseline 15-kW Bergey generator stator laminates were made of electrical steel using vacuum arc remelting of the alloy ingots, billet conditioning, surface graining, hot rolling followed by cold rolling, and stress annealing followed by slitting to required length for stamping, coating, and stacking. The tensile properties on the baseline Bergey stator laminates were measured with an ORNL SS3 standard-sized dog bone specimen. Results are reported in Figure 41. The Bergey generator stator exhibited a maximum tensile strength of approximately 450 MPa. Based on the initial results obtained by SLM for Fe<sub>3</sub>Si premixed with Al alloys, a stator laminate sector was printed for the 15-kW Bergey generator, as shown in Figure 42.



**Figure 41. (a) Image of Bergey generator stator; (b) tensile properties of Bergey generator stator with ORNL SS-3 standard sample specification with a thickness of 0.0185 in. for the dog bone samples**

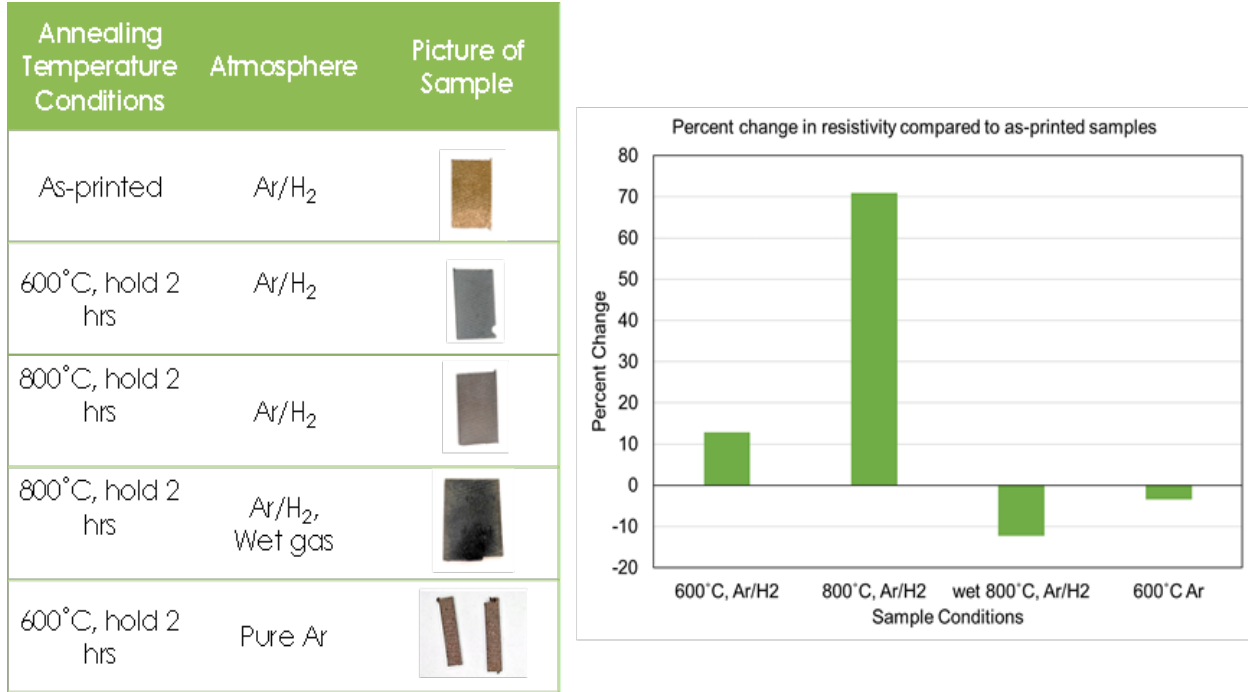


**Figure 42. SLM multimaterial printed Fe<sub>3</sub>Si premixed with Al alloy using the 15-kW Bergey generator stator design.**

Dimensions include the diameter,  $\varnothing = 21.6$ in. and thickness,  $t = 0.508$ mm

After printing, post-annealing was done under low partial pressures of oxygen, and a thickness of 0.508 mm was printed. Preliminary studies indicated that there was some increase in resistivity

(as shown in Figure 43), suggesting that the pre-alloyed Al was partially oxidized to  $Al_2O_3$ . After the success of the proof of concept, further work is needed to reduce the resistivity and improve the saturation magnetization. The printed laminates were sent to NASA Glenn for investigation of conductor printing.

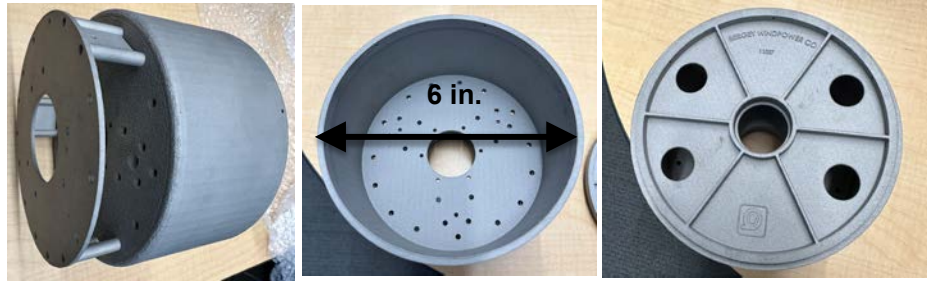


**Figure 43. (left) SLM multimaterial printed Fe<sub>3</sub>Si stator laminate annealed at different temperatures and atmospheres (argon (Ar), hydrogen (H<sub>2</sub>), and wet gas) and (right) the corresponding change in resistivity**

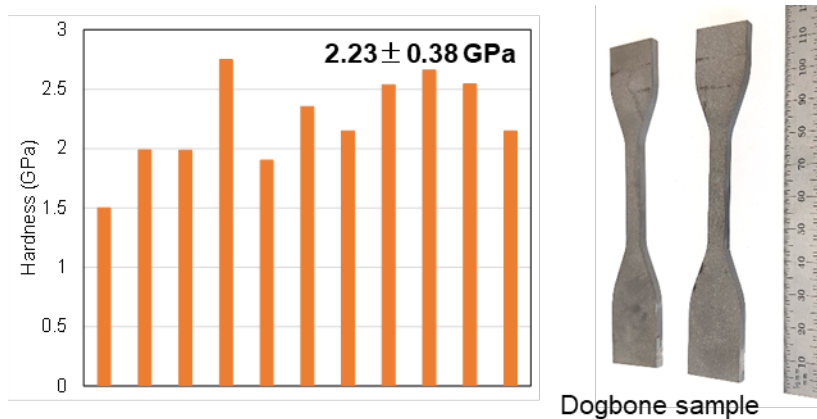
After successful experiments with stator laminate printing, the team proceeded to explore printing of rotor parts for the 15-kW Bergey generator.

### 3.1.3 Fabrication of a Proof-of-Concept Prototype Rotor Can

SLM was chosen for printing the rotor can based on previous successful demonstration with a smaller proof-of concept stator. Stainless steel 316 alloy was chosen based on suggestions from the Bergey team, and the properties were comparable with the 1020 steel that was used in the baseline design. A subscale version of the baseline rotor (measuring 6 in. in diameter and 4.25 in. in length) was printed as shown in Figure 44. A smooth surface finish was achieved. The 6 in. diameter was chosen because of the limitation of the SLM printer that was used. Although the rotor can serve both structural and magnetic functions, it was assumed that the magnetic properties will be consistent with electrical steel that was printed earlier. The mechanical properties of printed steel with ASTM dog bone standard are reported in Figure 45. A typical hardness of 2.23 gigapascal (GPa) was achieved. The Bergey rotor made out of carbon steel had the tensile strength of 400 MPa and yield strength of 221 MPa. The mechanical properties of SLM printed steel rotor met the specifications for the 15-kW Bergey generator.



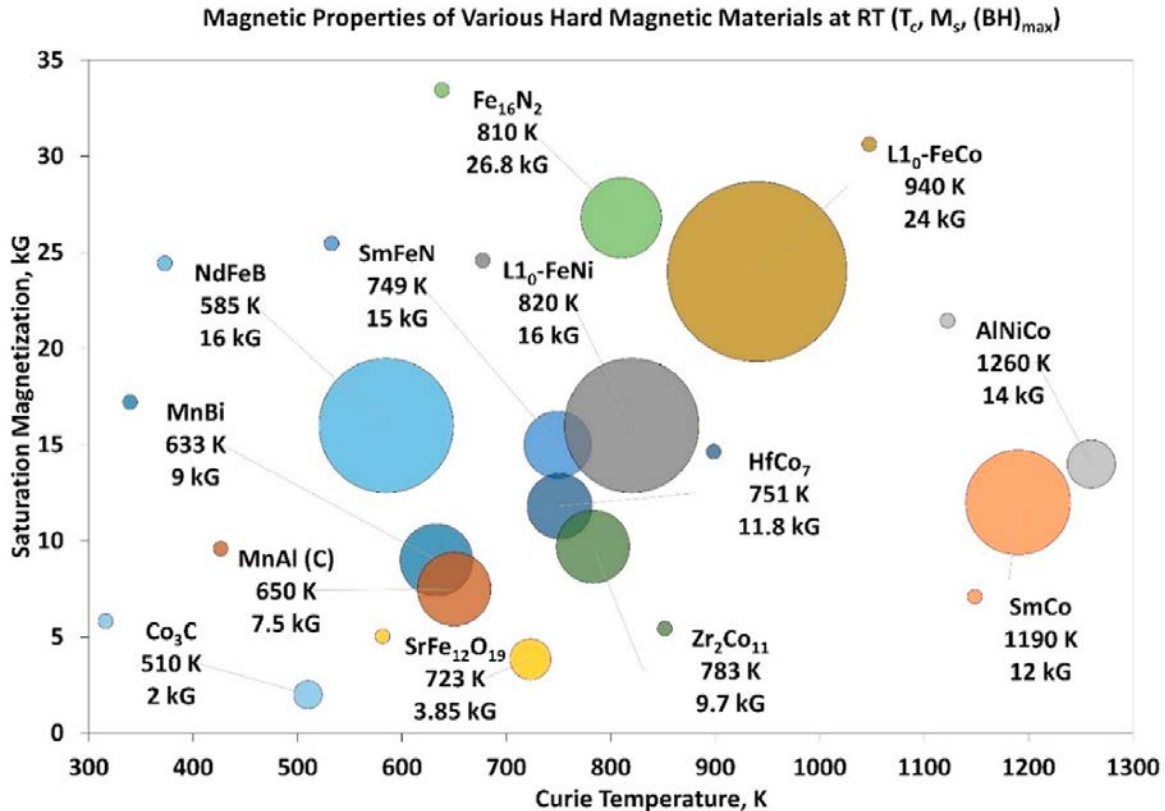
**Figure 44. SLM printed 6-in. reduced version of Bergey rotor can**



**Figure 45. The hardness properties of SLM printed dog bone samples**

### 3.1.4 Candidate Materials for Hard Magnets Chosen for Feasibility Study

The list of permanent magnets with magnetic properties suitable for use in wind turbine generators is shown in Figure 46 (Wang, Lamichhane and Paranthaman 2022). NdFeB with 4%–8% Dy with an energy product,  $BH_{max}$  of 52 MGOe is still considered as the strongest magnet. However, reducing the critical rare earth materials in NdFeB magnets used in wind turbines (i.e., by using aluminum and copper instead of Dy and Tb) has so far been limited by high-temperature operation requirements and the need for special cooling mechanisms. The introduction of small-sized SmFeN particles (critical rare-earth-free) in manufacturing NdFeB magnets with polymers can be a promising alternate for high-temperature operations. BJAT and BAAM FFF methods were used to print anisotropic Dy-free NdFeB magnets. The BJAT method yielded only 50% dense magnets. The magnets also degraded with bronze infiltration at higher temperatures. Alternative methods using post-annealing and low-melting-point eutectic alloys (i.e.,  $\text{Nd}_3\text{Cu}_{0.25}\text{Co}_{0.75}$  (NdCuCo) and  $\text{Pr}_3\text{Cu}_{0.25}\text{Co}_{0.75}$  (PrCuCo)) have been successfully infiltrated at higher temperatures. However, the energy product was lower than 5 MGOe (Li, et al. 2017). Hence, BJAT was not pursued further for printing NdFeB magnets. However, BAAM and/or compression molded magnets yielded energy products of up to 20 MGOe. The properties of BAAM printed magnets are reported in the following subsection.



**Figure 46. Permanent magnets suitable for use in wind turbine generators with saturation magnetization,  $M_s$  (kG) and Curie temperature,  $T_c$  (K). Energy product,  $BH_{max}$  is represented in circle size.**

Image from Wang, Lamichhane and Paranthaman. (2022)

### 3.1.4.1 Printing and Characterization of NdFeB+SmFeN Magnets With Energy Product of up to 20 MGOe

Based on previous printing iterations on polymer bonded magnets, anisotropic Magfine NdFeB powders without Dy (60%) were premixed with SmFeN (40%) in the ratio of 96 wt.% (75 vol%) to 4 wt.% of PPS polymers using a Brabender batch mixer. The extruded pellets were compression molded using a 50-t press at 200°C into 6 in. x 6 in. square plates with the thickness of 0.5 in. The details of the process were published earlier (Mungale, et al. 2021). The density of the compression molded magnets is 6.15 g/cm<sup>3</sup>. After hybrid magnet fabrication, small samples (5 mm<sup>3</sup> or less) were post-magnetic-field aligned at 1.5 T and 317°C. The magnetic properties of the hybrid bonded magnets are measured using a Quantum Design MPMS-3 magnetometer at 27°C. The magnetic properties are shown in Figure 47. To show the uniformity of the compression molded samples, the magnetic properties are reported for three samples in Table 23. Results indicate that remanence, coercivity, and energy product values for all three samples are less than 2%, 0.5%, and 3%, respectively. These results indicate that high-performance bonded magnets can be achieved using compression molding.



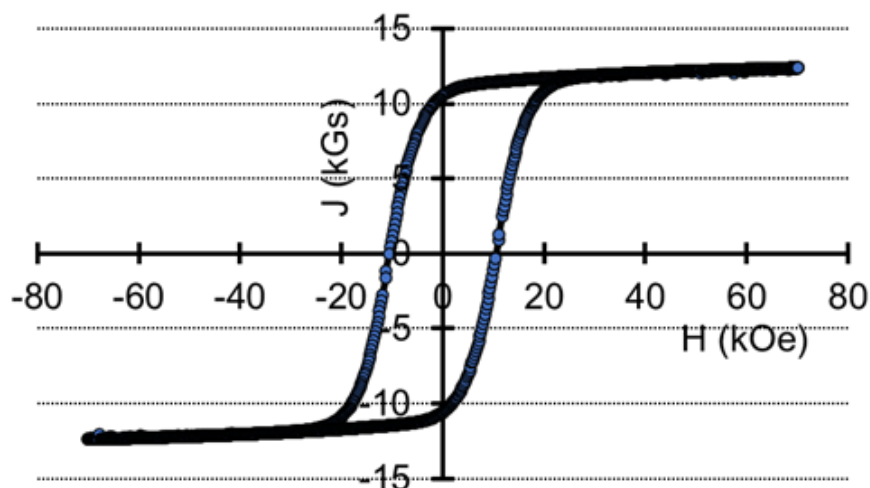


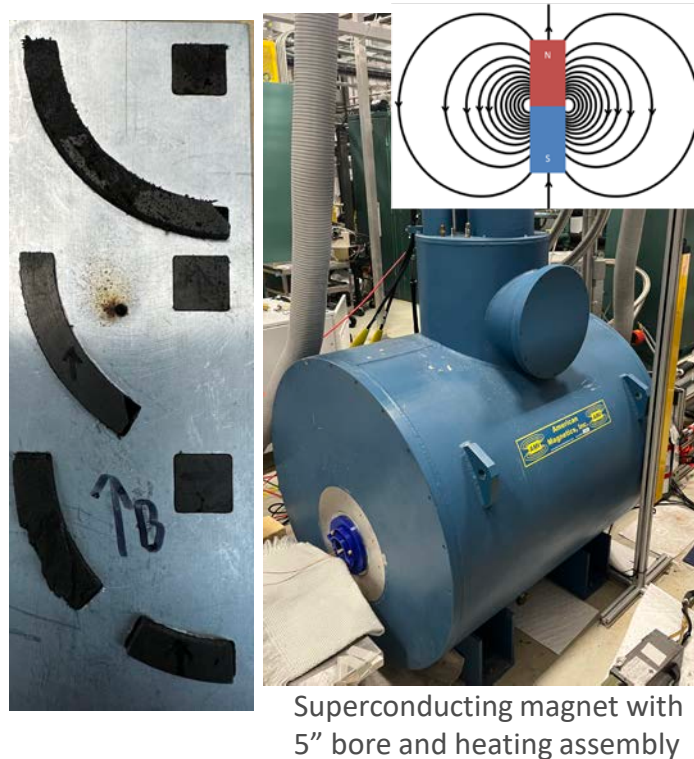
Figure 47. Magnetic properties of NdFeB with zero Dy-SmFeN PPS bonded magnets

Table 23. Magnetic Properties of NdFeB With Zero Dy-SmFeN PPS Bonded Magnets

Sample ID	Remanence $B_r$ (T)	Coercivity $H_{ci}$ (kA/m)	Maximum Energy Product $(BH)_{max}$ (kJ/m <sup>3</sup> )
1	1.04	859.44	159.16
2	1.05	861.03	159.16
3	1.02	856.25	155.18

### 3.1.5 Post-Magnetic Grain Alignment of Printed Magnets

The results from post-magnetic-field annealing studies with smaller printed magnet samples (Figure 47 and Table 23) helped us conclude that higher-energy products will be possible. Hence, these methods were investigated for larger, printed magnets. As shown in Figure 48, larger samples of magnets with different dimensions and curvatures were printed and used for further investigation. To facilitate the study, a larger, aluminum-based alignment fixture (~2 in. x 4 in. x 5 in.) was fabricated for post-magnetic-field annealing studies. Considering the need for a larger volume of magnet material, the team printed 94.6 wt.% of NdFeB+SmFeN (70 vol%) 5.39 wt.% of nylon using BAAM and machined to fit the slots in the aluminum fixture. The aluminum fixture with inserted bonded magnets is shown in Figure 44. Aluminum blocks with magnets were introduced into the superconducting magnet and heated the assembly to ~200°C for 5 minutes through a 2-hour ramp in a static field of 5 T; samples were cooled to room temperature. Magnets with energy product of >14.6 MGOe were achieved. Magnetic measurements indicate that more than 92%–95% grain alignment was achieved. Similar post-magnetic-field annealing is needed for large printed bonded magnets.



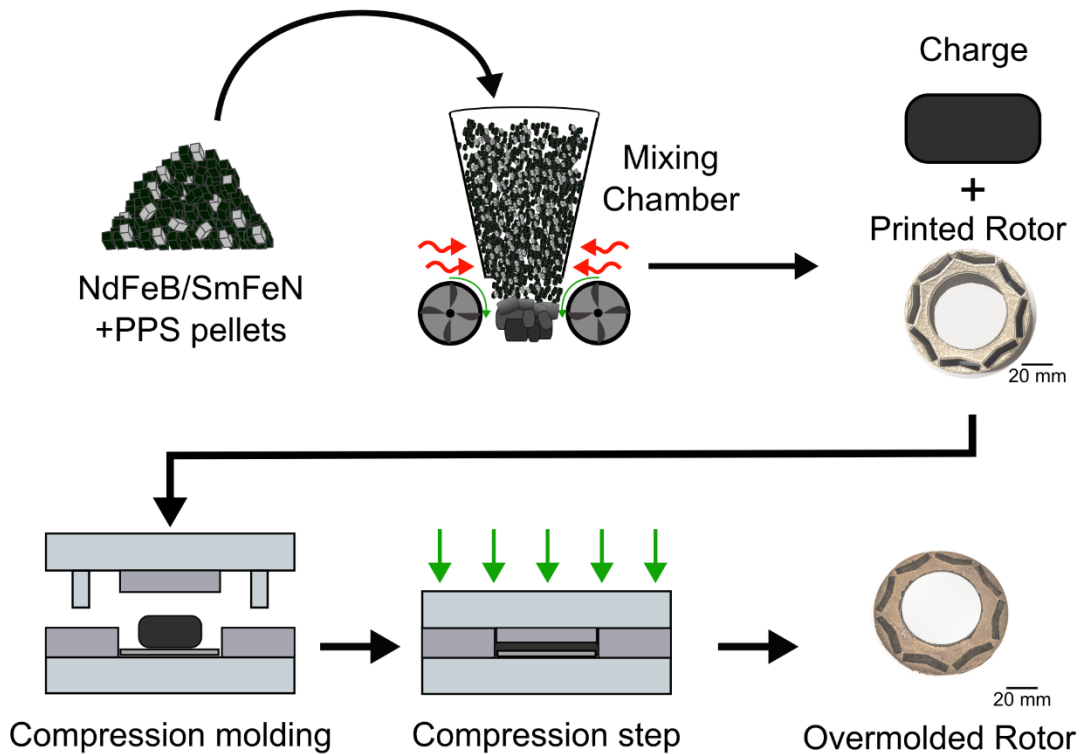
**Figure 48. (left) Image of the Al block that was used for post-magnetic-field annealing with inserted BAAM magnets and (right) superconducting magnet**

The developed post-magnetic-field alignment fixture is scalable for post-magnetization of larger magnets such as those used in large wind turbine generators. Higher magnet-loaded samples (75 vol% or higher) can also be aligned.

### **3.1.6 Overmolding of Printed Magnets With Electrical Steel for a Proof-of-Concept Rotor**

In order to examine a multimaterial fabrication technique for magnets with electrical steel in the rotor, some overmolding techniques were surveyed. FFF is used to print both the magnets and electrical steel in consecutive steps. However, this process may not yield high saturation flux densities for electrical steel and may weaken the strength of the rotor. The second process is additive manufacturing of magnets followed by compression molding (AMCM) into SLM printed electrical steel. This process significantly improves the magnet density, but the interface between the electrical steel and polymer can be weak. We tested the second approach for overmolding hybrid NdFeB-SmFeN PPS bonded magnets onto an SLM printed Fe3Si rotor for a V-shaped IPM rotor design, which was initially investigated by NREL. The extruded 70 vol% NdFeB+SmFeN+nylon composite pellets were compression molded at a pressure of 11.49 MPa with a dwell time of 20 minutes. A 30-t hydraulic press (Carver, Model #3895) was used for the molding. The schematic of the process is shown in Figure 49 for multiple versions of the printed rotor. The charge was placed above the laser additively fabricated Fe3Si part and compressed into the holes for the rotor magnets; excess charge/flash was removed after the compression molding via cutting and machining. The use of precise charge size or advanced manufacturing techniques such as additive manufacturing can minimize any post-processing requirements.

More details of the method and results are available in (Kemp, et al. 2024). Typically, 8.9% porosity is measured with printed magnets; however, with compression molding, the porosity was reduced to 4.7%. Detailed microstructural characterizations were carried out. The interface between the steel and the magnet is clean, as can be seen in the scanning electron microscopy (SEM) images (Figure 50). However, the performance of overmolded magnets degraded slightly due to the surface oxidation of magnets during compression molding. Hence, further optimization of the use of inert gas during compression molding was needed. The printed, grain-aligned polymer bonded magnets can be attached inside the rotor can by warm compaction. This method could help avoid the use of adhesives/thermoset polymers for bonding sintered magnets to the rotor. We demonstrated this step to eliminate the additional bonding step.



**Figure 49. Schematic flowchart of fabricating insert/overmolding of the SLM printed Fe<sub>3</sub>Si rotor**

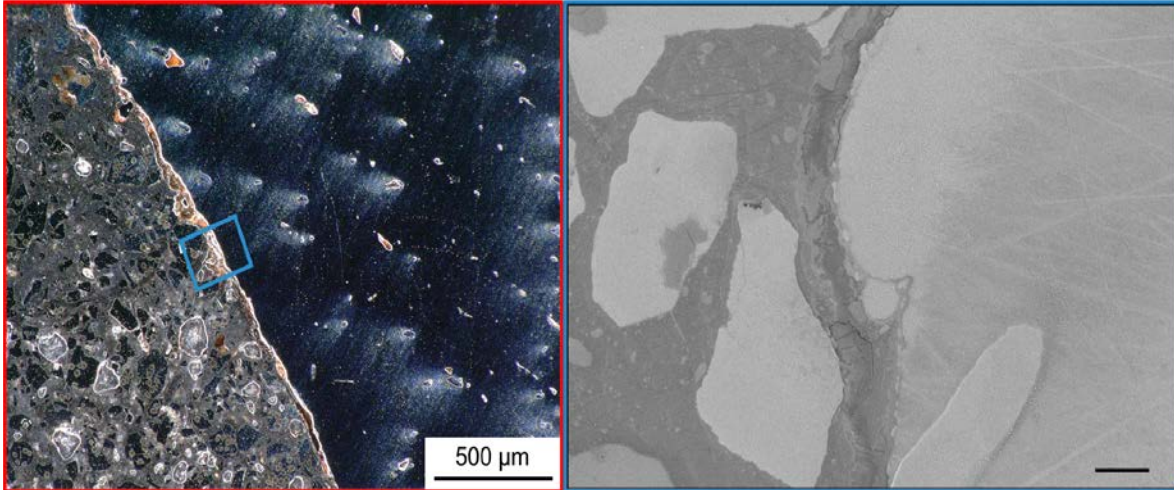
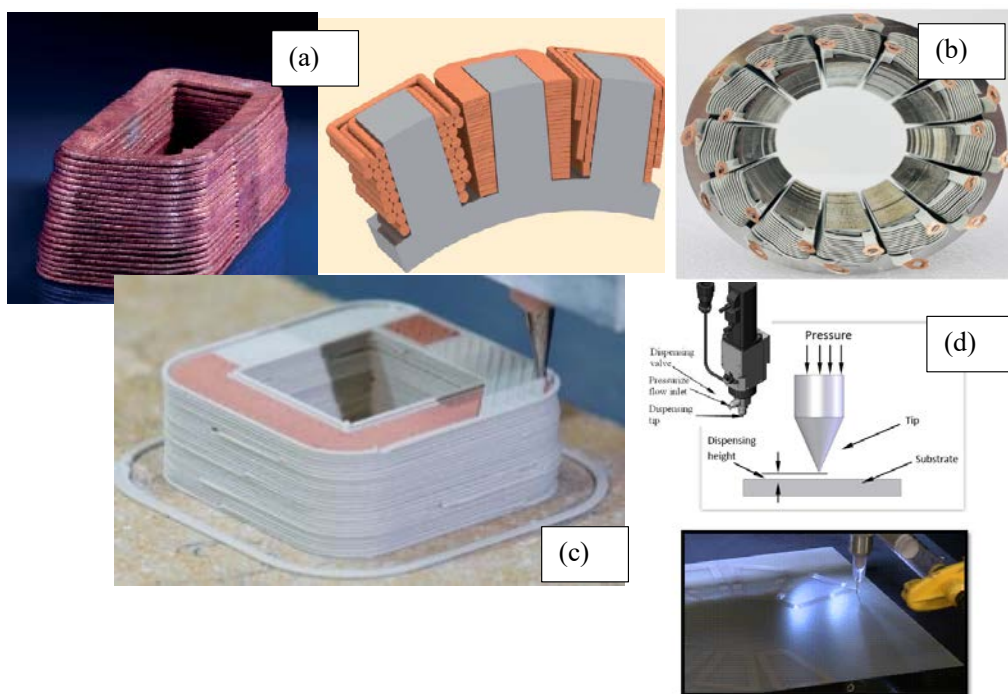


Figure 50. SEM images of overmolded rotor

### 3.1.7 Multimaterial Printing of Stator Conductors With Insulation

In this task, the NASA Glenn team pursued the development of advanced additive manufacturing processes toward the development of a multimaterial stator for the 15-kW Bergey generator. The focus was on optimizing the 3D printing of the key stator elements of conductive windings insulation followed by their integration into a stator sub-element consisting of an insulative sleeve with integrated conductive coils. The main goal of the new manufacturing effort is to achieve high coil space fill factors that are crucial for increasing the energy efficiency and power density in wind turbine generators. This is possible by retaining the slot dimensions and current density and using alternative conductor materials. The team surveyed several new methods of conductor manufacturing that were known to be available during the project, which included casting, LBPF, and FFF. A variable-cross-section coil that was obtained by casting was reported in reference (Busse n.d.) (see Figure 51a). The approach could be limited by geometry constraints and minimum achievable wall thicknesses for insulation. LPBF methods have also advanced to produce coils individually and were shown to achieve fill factors of up to 63% (Selema, Ibrahim and Sergeant 2022); however, multimaterial printing has not been demonstrated to date.



**Figure 51. (a) Cast coils by Fraunhofer Institute with the potential to achieve 90% fill factor, (b) coils produced by Additive Drives, (c) ceramic insulated copper coils produced by extrusion, and (d) direct-ink write by NASA**

Multimaterial printing of ceramic insulated copper coils has been demonstrated using an FFF-based extrusion technique (see Figure 51c). However, so far, lower values of specific electrical conductivity have been reported for the printed copper (71%), and 87% density was reported due to remaining porosity and impurities. The scalability of such a process to the macroscopic scale is a particular challenge due to the high specific coefficient of thermal expansion of copper ( $16.5 \times 10^6 \text{ K}^{-1}$ ) while most engineering ceramics have lower values (Lorenz, Rudolph and Wemer 2018). On this end, the NASA Glenn team has been actively researching the use of multimaterial printing for stators and using the DIW approach to print conductive inks containing materials such as silver or copper nanoparticles for the creation of customized circuits. They have previously successfully printed conductors for aerospace applications achieving up to twofold improvements in power densities in aerospace motors (see Figure 51d) (Halbig and Singh 2019). As part of the MADE3D project, the team extended the processes to investigate the feasibility of several low-resistance conductors for use in wind turbine generators. The baseline Bergrey generator utilized conductor and insulation material as listed in Table 24. Using square wires to achieve high fill factors has been difficult in a limited production shop (as it entails more wire-handling equipment to prevent twisting of the wire during the coil-forming process). Using a slot wedge design and a coil winder allowed for easy wire insertion, but necessitated precisely preformed coils and a lack of winding design flexibility because the single-layer coils must fit in the slots. Therefore, the present effort was aimed at investigating the feasibility of multimaterial printing of conductors with high-temperature insulation material that achieves high fill factors while also achieving high electrical conductivity.

**Table 24. Conductors and Insulation in Baseline Generator**

Conductor	Magnet Wire – Copper
Size	14 AWG
Insulation material	Polyester/Polyamide-imide
Temperature rating	200°C

### 3.1.7.1 Candidate Down-Selection for Conductors

Several conductive pastes were printed and characterized for this study. These included three commercial silver pastes from Heraeus (West Conshohocken, PA), two commercial copper paste formulations from PrintCB (Ness Ziona, Israel), a silver-coated copper paste formulation made from a powder from Ames Goldsmith (South Plainfield, NJ), and four silver-copper hybrid paste formulations made from combining silver and copper pastes. Each paste varied in viscosity, solid loading, curing temperature, and electrical conductivity.

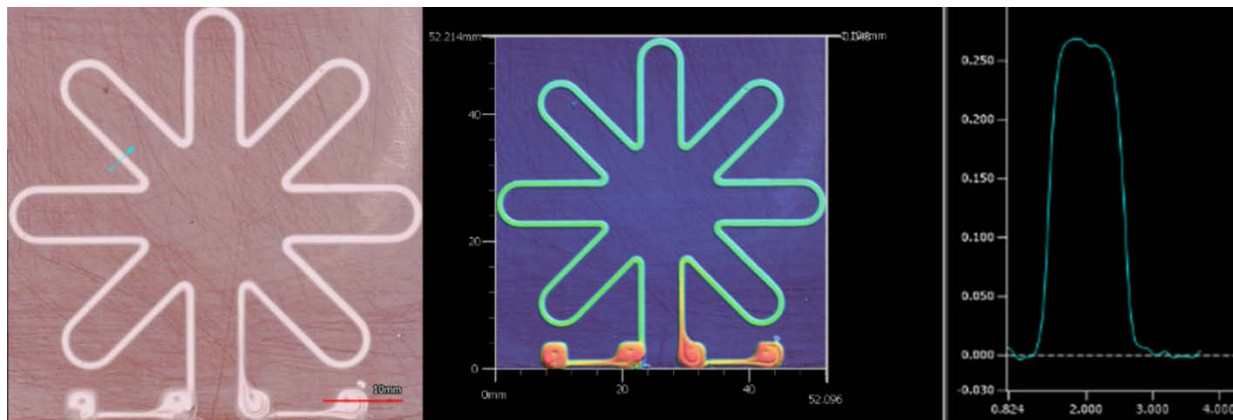
- Three silver pastes from Heraeus were procured and mixed with copper paste with different ratios: Heraeus CL20-1127, Heraeus LTC3650, and Heraeus mAgic sinter paste DA295A.
- The copper pastes were made from the commercial mixture CopPair+2, which is sold as two separate parts—a solid powder MetalX, and a liquid binder ActiveX, meant to facilitate oxidation-free curing. The copper pastes were then formed by mixing the two (MetalX: ActiveX), one at a ratio of 4.5:1 and the other at a ratio of 5.5:1.
- The silver-coated copper paste was prepared in-house by combining silver-coated copper (AgCu0204C) with additional additives and viscosifiers.
- For making silver-copper hybrid pastes, two approaches were pursued: In the first, 3:1 CopPair+2 MetalX paste was mixed with the Heraeus CL20-1127, along with compatible additives. This was done both with and without the hydroxyethyl cellulose (HEC) as additional binder. In the second method, silver-coated copper paste was combined with the Heraeus CL20-1127. This was done in ratios of 3:1 and 2:1, with the leading component being the silver-coated copper paste.

### Printed Samples of Conductors and Performance Characterization

All pastes were printed with the nScript 3dn-300 system (Orlando, FL) using Nordson (Westlake, OH) dispensing tips. Each sample was printed in a circumferential serpentine pattern (Figure 52) on either fiber glass or Meldin (high-temperature thermoplastic). The serpentine pattern was selected to assess printing of a complex shape comparable to the coils of a stator component. The pattern had four pads to facilitate four-point probe resistance measurements. The printing parameters varied based on the paste's rheology. Initial print optimization trials determined the optimal dispensing tip, offset distance between the nozzle and substrate, print speed adjusted for the individual paste viscosity, and the nozzle pressure.

A drying oven was used to thermally cure samples. Each paste had a different curing temperature and time according to the vendor recommendations. The electrical resistance of each cured print was measured using a four-probe micro-ohm meter where a low voltage was applied to the two outer pads while the resistance was measured at the two inner pads. Once resistance values were obtained for a sample, a profilometer (Keyence VR-3200) was used to generate a topological

image and a cross-sectional profile (Figure 53). From these profile traces, the cross-sectional areas were calculated by the trapezoidal rule for integration. The resistivity of each sample was then calculated by  $R = \rho L/A$ , where  $R$  is the resistance of the current-carrying path,  $\rho$  is the resistivity of the material,  $L$  is the length of the current carrying path, and  $A$  is the cross-sectional area of the current carrying path.



**Figure 52. An example serpentine pattern trace imaged on profilometer: (left) optical and (middle) topological images. (right) A cross section of the printed trace taken along the cyan line has been used for the calculation of the resistivity.**

The various conductive pastes that were formulated are shown in Table 25 along with their relative curing temperatures and times. Also included in the table are the measured electrical resistance, the cross-sectional area of the four-point probe pattern, and the resulting resistivity for each paste. The conductivity values expressed as a percentage of IACS with 58.108 mega-siemens per meter (MS/m) as the standard conductivity of annealed copper at 20°C.

**Table 25. Conductive Pastes, Curing Conditions, Electrical Resistance, Cross-Sectional Area, and Resistivity for the Samples Explored in This Work**

Material Category	Paste	Vendor Material	Curing (°C   minutes)	Resistance (Ω)	Area (mm <sup>2</sup> )	Resistivity (Ω m)	Conductivity % IACS
Silver	CL20_1	Heraeus-CL20-1127	250   30	0.214	0.146	4.95E-08	34.83%
	CL20_circa2019	Heraeus-CL20-1127	300   60	N/A	N/A	4.37E-08	39.45%
	LTC3650_1	Heraeus-LTC3650	250   30	0.112	0.498	8.86E-08	19.46%
	LTC3650_2	Heraeus-LTC3650	200   30	0.595	0.116	1.10E-07	15.67%
	LTC3650_3	Heraeus-LTC3650	200   30	0.340	0.198	1.07E-07	16.11%
	DA295a_1	Heraeus-mAgic SINTER DA295A	250   30	0.056	0.678	6.03E-08	28.59%
	DA295a_2	Heraeus-mAgic SINTER DA295A	200   30	0.305	0.119	5.76E-08	29.93%
	DA295a_3	Heraeus-mAgic SINTER DA295A	200   30	0.375	0.096	5.71E-08	30.19%
Copper	Coppair4.5_1	PrintCB-CopPair+2	150   30	0.465	0.74*	5.4E-07*	3.19%
	Coppair4.5_2	PrintCB-CopPair+2	150   15	0.656	0.49*	5.1E-07*	3.38%
	Coppair5.5_1	PrintCB-CopPair+2	150   45	2.828	0.176	7.92E-07	2.18%
	Coppair5.5_2	PrintCB-CopPair+2	150   75	2.657	0.223	9.40E-07	1.83%
	CopCL20_1	PrintCB-CopPair+2/Heraeus-CL20-1127	250   15	63.65	0.635	6.42E-05	0.03%
	CopCL20_2 (HEC)	PrintCB-CopPair+2/Heraeus-CL20-1127	250   30	60	1.07	1.02E-04	0.02%
	CopCL20_3 (HEC)	PrintCB-CopPair+2/Heraeus-CL20-1127	250   30	132.5	0.061	1.28E-04	0.01%
Silver-coated copper	AgCu0204C_1	Ames Goldsmith-AgCu0204C	150   30	3.529	0.243	1.36E-06	1.27%
	AgCu0204C_2	Ames Goldsmith-AgCu0204C	150   60	2.727	0.295	1.28E-06	1.35%

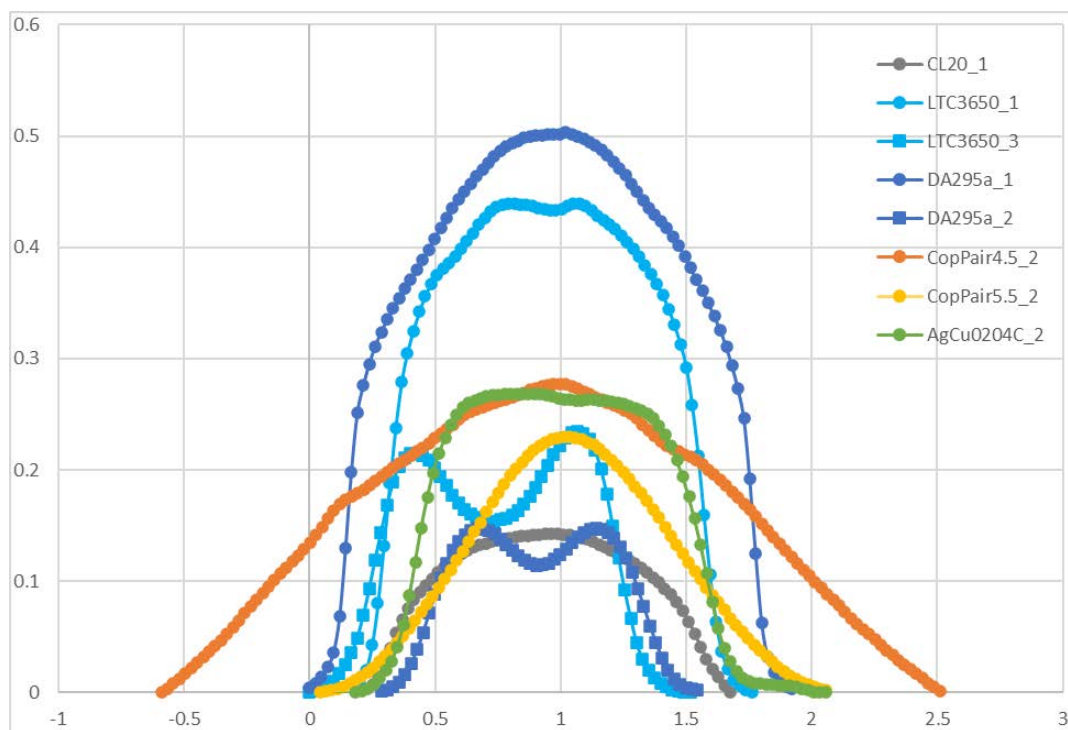


Material Category	Paste	Vendor Material	Curing (°C   minutes)	Resistance (Ω)	Area (mm <sup>2</sup> )	Resistivity (Ω m)	Conductivity % IACS
	AgCu0204C_5	Ames Goldsmith-AgCu0204C	200   30	1.124	0.486	8.67E-07	1.99%
	AgCu0204C_6	Ames Goldsmith-AgCu0204C	200   60	1.150	0.415	7.58E-07	2.27%
	AgCu0204C_3	Ames Goldsmith-AgCu0204C	250   30	4.178	0.386	2.56E-06	0.67%
	AgCu0204C_4	Ames Goldsmith-AgCu0204C	250   60	16.736	0.411	1.09E-05	0.16%
Hybrid silver-copper	AgCuCL20_1 (3:1)	Ames Goldsmith-AgCu0204C/Heraeus-CL20-1127	200   30	0.426	0.787	5.33E-07	3.23%
	AgCuCL20_2 (3:1)	Ames Goldsmith-AgCu0204C/Heraeus-CL20-1127	200   60	0.365	0.889	5.15E-07	3.35%
	AgCuCL20_3 (2:1)	Ames Goldsmith-AgCu0204C/Heraeus-CL20-1127	200   30	0.509	0.520	4.21E-07	4.10%
	AgCuCL20_4 (2:1)	Ames Goldsmith-AgCu0204C/Heraeus-CL20-1127	200   60	0.527	0.464	3.88E-07	4.44%

The conductivities of silver pastes were investigated first, including the effect of varying print shapes. Figure 53 shows the overlapping trace profiles for samples tested. Note that despite the difference in area within both the Heraeus LTC3650 samples and the two Heraeus mAgic SINTER DA295A samples, resistivities were found to be similar, and thus no surface effects occurred for different geometries, which could have potentially skewed the results.

CopPair+2 pastes resulted in wider prints owing to their low viscosity. This can be seen in Figure 53. Overall, both CopPair+2 pastes yielded higher resistivity by about 1 order of magnitude than the silver pastes. The CopPair+2 pastes also were found to have less adhesion than the silver pastes, as observed by their cracking and separation from the substrate surface.

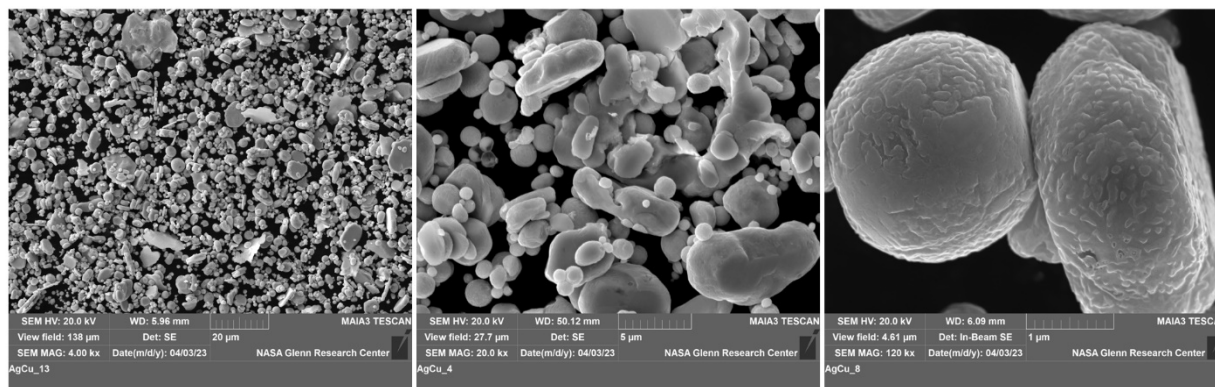
SEM with energy dispersive spectroscopy was conducted on the MetalX powder used for the CopPair+2 pastes. From energy dispersive spectroscopy analysis, it was revealed that MetalX was a compound powder containing traces of bismuth and tin. Attempts were made to combine the Heraeus CL20-1127 with the CopPair+2 MetalX to find an optimal balance between performance and cost (CopPair+2 was lower cost). These silver-copper hybrid pastes were made primarily by mixing CopPair+2 MetalX, Heraeus CL20-1127, glycerol, and defoamer along with HEC to provide additional binding. These hybrid pastes yielded even lower conductivity than each paste individually. From these results, more sophisticated means are clearly necessary to combine the Heraeus CL20-1127 and the CopPair+2 MetalX in an effective way.



**Figure 53. The cross-sectional trace profiles taken of serpentine prints of various pastes. The height and width are in mm.**

An alternative approach to combine silver and copper used silver-coated copper particles, AgCu 0204C-12. AgCu 0204C-12 is a commercialized silver coated copper powder from Ames Goldsmith with a controlled particle size of 2–4- $\mu\text{m}$  flakes. Figure 54 shows SEM images of the silver-coated copper powder. Note the small bimodal particle sizes, ideal for the condensed

packing of particles. The powder was combined with alpha terpineol carrier and oleic acid to form a paste like Heraeus CL20-1127. Because this paste was made fully in-house, a thorough exploration was necessary to determine the ideal sintering parameters. Hence, the temperatures of 150°C, 200°C, and 250°C were investigated for both 30 and 60 minutes. Overall, the printability of this paste was much better than the CopPair+2 pastes and comparable to that of the silver pastes. Optimized curing occurred at 200°C for 60 minutes. The resistivity was found to be comparable to that of the CopPair+2 paste, indicating that the copper is the leading transport mechanism of the paste. This was confirmed with elemental analysis, where energy dispersive spectroscopy revealed about 6 times as much copper than silver was present in the powder (silver serves as a thin coating for copper to hinder oxidation).



**Figure 54. SEM images of the silver-coated copper powder. Note the small bimodal particle sizes, ideal for the condensed packing of particles.**

The AgCu 0204C-12 paste was combined with a smaller amount of the silver Heraeus CL20-1127 paste in a second attempt to balance cost and performance. Unlike the previous hybrid attempts, both these attempts led to an increase in conductivity compared to the AgCu 0204C paste alone; the addition of Heraeus CL20-1127 led to  $\sim 1.5x$  and  $\sim 2x$  increase in conductivity for the ratios of 3:1 and 2:1, respectively. However, these hybrid pastes remained about 1 order of magnitude lower than the pure silver of Heraeus CL20-1127.

Heraeus CL20-1127 showed the highest conductivity of the evaluated pastes at  $\sim 35\%$  IACS. Based on previous work with this paste, it is recommended that it be sintered at 300°C for 1 hour, because those parameters yielded the best conductivity while also providing a higher density. The copper-based pastes provided much lower electrical conductivity than the silver pastes, although at a quarter of the price. Preliminary attempts to enable hybrid pastes using the Heraeus CL20-1127 with the CopPair+2 MetalX to find a balance between performance and cost proved to be unsuccessful. The AgCu0204 paste possessed much greater compatibility with Heraeus CL20-1127, although conductivity was still much less than any of the individual silver pastes. In terms of rheology and printability, the AgCu0204 paste and its hybrids were the better copper pastes compared to the CopPair+2 pastes. Therefore, the silver-coated copper paste, AgCu0204, was down-selected as the conductor material.

### 3.1.7.2 Insulating Sleeve Printing and Design

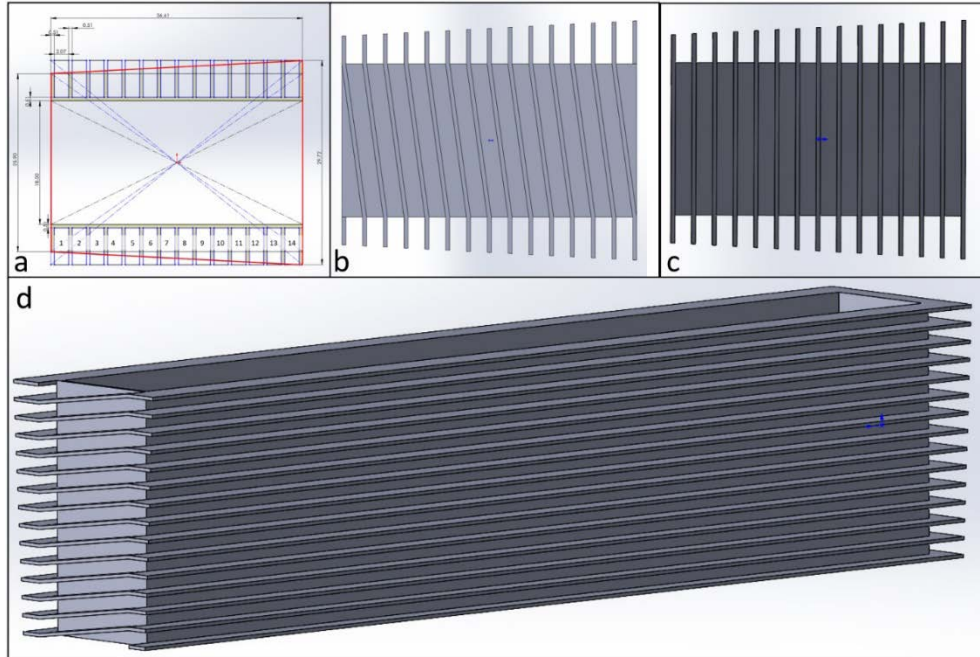
In addition to the 3D printing of the conductive pastes, an insulating sleeve to house the conductors was also 3D printed. Several methods were investigated, including FFF,

stereolithography, selective laser sintering, and multi-jet fusion to print the sleeve as one solid print. The sleeve is inserted onto the stacked laminates of the optimized Bergey stator once conductive paste is integrated into them such that the final product serves as a support and divider for the conductive coils. The most important target specifications for sleeve material were the temperature rating of 200°C and minimum printable wall thickness.

Stereolithography printing was done by Xometry, Inc. (Bethesda, MD) for both their standard resin, Accura 25, and their high-temperature resin, Somos PerFORM, which has a heat deflection temperature of 268°C. While stereolithography printing was able to produce the sleeve as one solid print, resolutions for the channels needed to be revised. These adjustments greatly decreased the fill ratio of conductive paste to insulating sleeve. Both selective laser sintering and multi-jet fusion printing were done by HUBS (New York, NY), both in nylon. These were also printed as single solid pieces. However, neither of these print methods could be conducted with high-temperature materials. Thus, current additive manufacturing technology prevents a full sleeve to be printed that is both (1) capable of enduring the high temperatures required for conductive paste curing and (2) high enough resolution to provide thin features required for large numbers of turn channels. Favoring maximized conductor packing and high-temperature capability, the two-part FFF printed ULTEM 1010 sleeve is the leading candidate for sleeve production. ULTEM 1010 has a heat deflection temperature of 216°C.

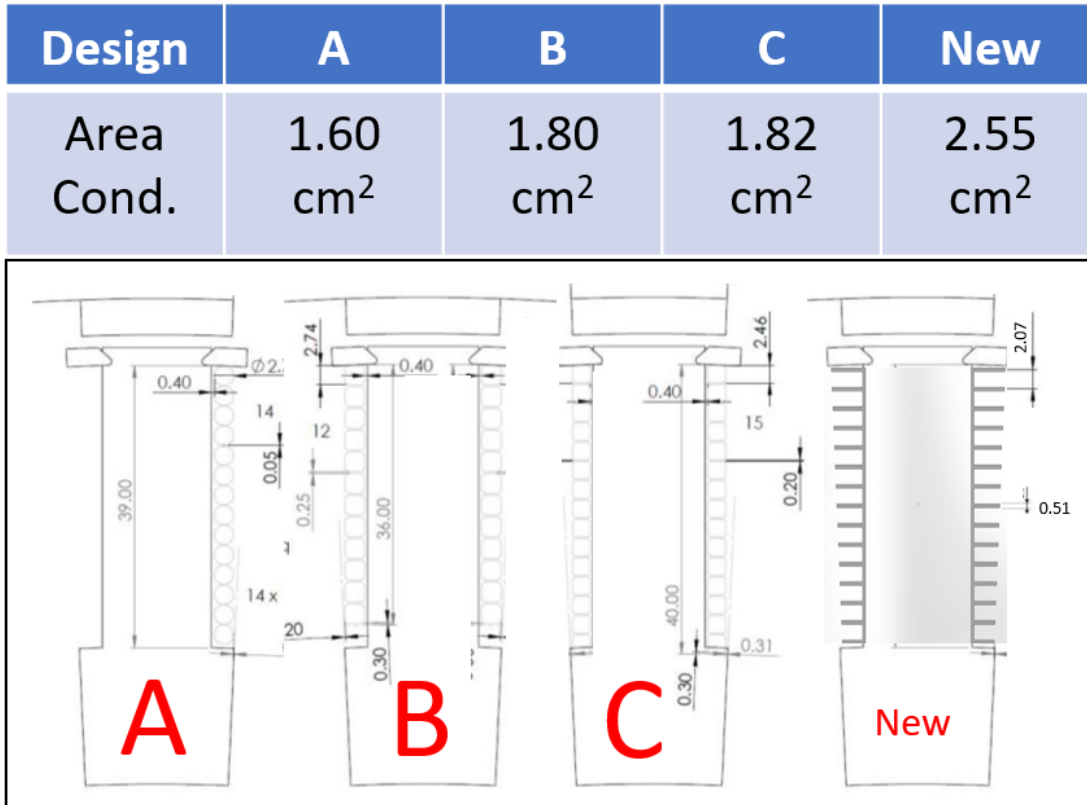
### *3.1.7.3 Sleeve Design*

Figure 55a shows the crucial cross section of the insert design. The outlined area in red indicates the space available for the sleeve such that neighboring sleeves could be inserted on the 18-mm-wide laminate extensions without intersection. The angle of the horizontal red lines is owed to the increasing space surrounding the laminate as it expands outward radially. The resulting sleeve was then composed of 14 turns of ~2.07 mm of varying heights; this was dictated by the FFF printing resolution of the insulator material, ULTEM 1010, which required a minimum thickness of 0.02 in. (~0.51 mm). Figure 55d shows the final three-dimensional stator sleeve as it wraps around the 150-mm-long laminate. Channel turns were designed to take place on one of the short edges (Figure 55b). For the short sides of the sleeve (Figure 55b and c), wall heights were taken to be 4 mm to match the shortest channel height on the long side.



**Figure 55. Insulating sleeve insert: (a) the crucial cross section of the insert design. The outlined area in red indicates the space available for the sleeve such that neighboring sleeves could be inserted on the 18-mm-wide laminate extensions without intersection. The angle of the horizontal red lines is owed to the increasing space surrounding the laminate as it expands outward radially. (b), (c), and (d) Final stator sleeve design from different angles.**

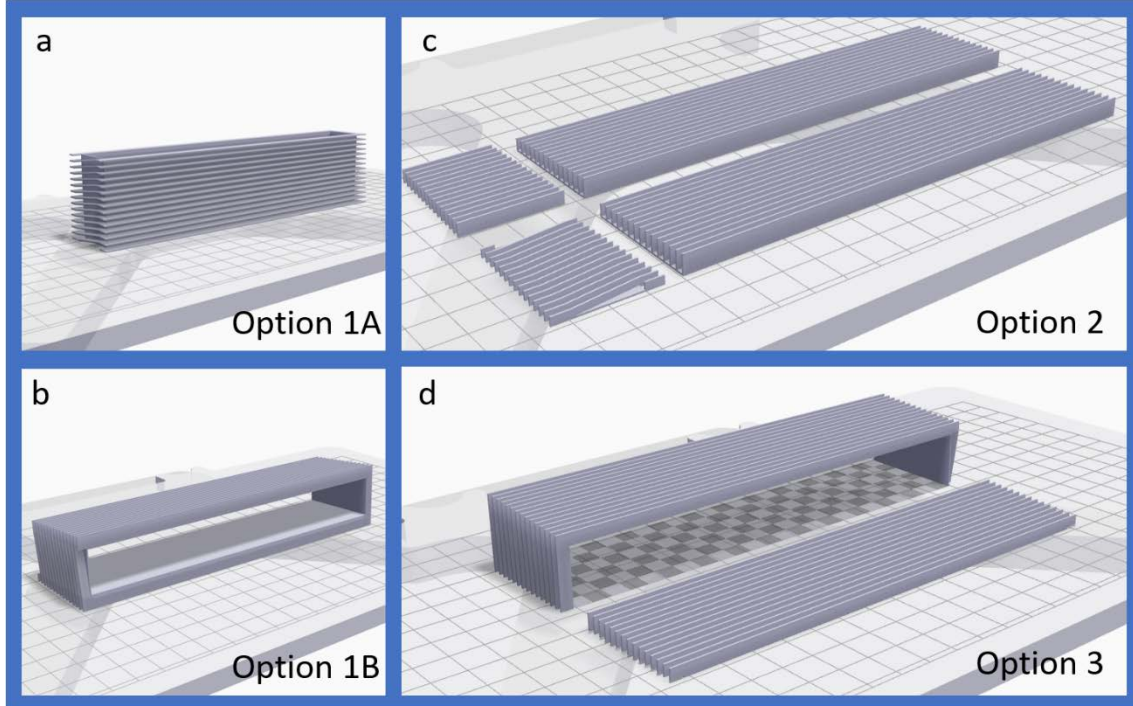
The insert design was optimized for channel wall heights that increase to fill the open sections at the outer diameter of the stator to allow maximum conductor packing. This is a stark contrast to the uniform wrappings of conductive wire found in the traditional stator assembly with square and round conductors (see Figure 56). Comparing three traditional stators to this new additive manufacturing design, there's an increase in conductor area of at least 40%. This equated to fill factors in the range of 70%–80% due to the higher insulator walls and resulting higher coil heights at the outer diameter of the stator sleeve as well as the more optimal filling of the slot. The additive manufacturing processes allow for square, trapezoidal, or rectangular coil cross sections compared to the smaller coil areas achieved with conventional conductors with circular wires.



**Figure 56. Three traditional stator geometries versus the new proposed stator geometry. The area of conductor is calculated at the displayed cross section of each stator.**

With the insulating sleeve designed, it was important to consider print orientation. Print orientation plays a significant factor in FFF because structures that do not directly touch the print bed require support structures to be printed. Support structures support the overhanging structures and are designed to be removed after printing. For particularly thin features, supports can be problematic to remove because the integrity of the thin feature can be comparable to that of the supports. For example, supports in print option 1A (Figure 57a) would fill all 14 channels on all four sides of the sleeve, compromising every channel wall. Print option 1B (Figure 57b), on the other hand, frees up three of the four sides and mainly fills the inner opening, which is more structurally stable. Unfortunately, print option 1B still rendered one of the walls potentially unusable. To address this challenge, alternative print options were considered.

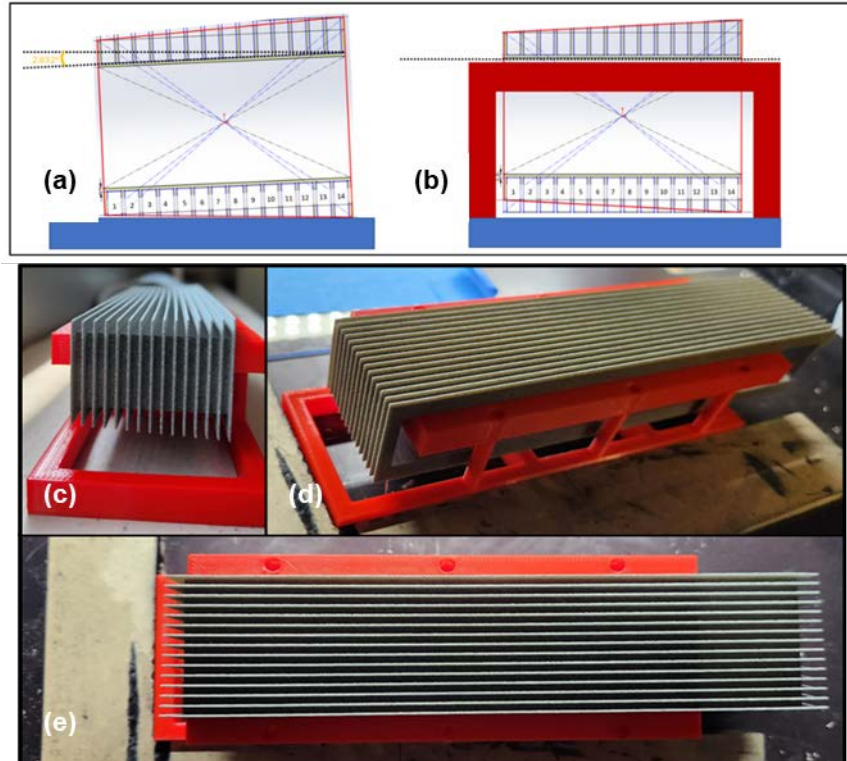
For print option 2 (Figure 57c), each side is printed separately such that no support material is necessary. This option created four clean prints in exchange for cumbersome assembly. Upon comparing the first two options, print option 3 was then designed to combine the easy assembly of option 1 and the clean, low amount of support structures of option 2. Print option 3 (Figure 57d) prints the sleeve as two parts; one part is the two short sides and one long side (like option 1B), and the other part is one individual long side. The two sleeve parts can be adhered together with a nonconducting silicone adhesive and left to dry overnight.



**Figure 57. (a–d) Four possible print configurations that were considered for FFF**

### **3.1.8 Proof-of-Concept Prototype Conductor Printing for Bergey’s Stator Tooth**

Following discussions with NREL team members and a preliminary cost analysis for ink formulations, the silver-coated copper paste was chosen as the prevailing conductive paste since it had the best trade-off in terms of electrical conductivity, thermal stability, and lower costs for integration into the insulating sleeve. Initial print trials were conducted on singular sides of the sleeve (Figure 57, long side of print option 2) to optimize print parameters. Suitable parameters were characterized by even, flat prints that fully encompassed the channel width; this was found for prints at ~690 kPa with a 0.84-mm-diameter nozzle and a print speed of 1.0 mm/s. Channels were able to be filled after 3–5 passes, depending on the wall height.



**Figure 58. Sleeve holder for printing. A sketch depicting printing (a) without the sleeve holder and (b) with the sleeve holder. (c–e) Optical images of the sleeve holder.**

With preliminary paste prints made, the next challenge was to print on a fully assembled sleeve. To facilitate this printing, a sleeve holder was designed and printed using polylactic acid plastic. The holder allowed for an even print plane to be established for the long side such that clearance could be kept constant for each channel of a side. Figure 58 (a) and (b) show the difference between printing with and without the holder on the long side of the sleeve. With the addition of the sleeve holder, the sleeve was able to hover over the print bed such that the print plane was parallel with the print bed and hence perpendicular to the print head. Figure 59 is an image of a sleeve (ULTEM 1010, two-part FFF option) partially filled with the AgCu0204-12 paste. The sleeve was printed at  $\sim 690$  kPa with nozzle diameter 0.840 mm at print speed 1.0 mm/s with 4.0-mm clearance from the bottom of the sleeve channel. The sleeve was filled in 3–5 passes (depending on the channel). Conductivity measurements on the sleeve verified expected conductivity of Table 26, with  $1.08E6$  S/m and  $4.35E5$  S/m, respectively, for three channel laps cured for 1 hour at  $200^{\circ}\text{C}$  and one channel lap cured for 30 minutes at  $200^{\circ}\text{C}$ .





**Figure 59. A sleeve (ULTEM 1010, two-part FFF option) partially filled with the AgCu0204-12 paste**

In summary, several conductive pastes were evaluated for printability, temperature capability, electrical conductivity, and costs. A silver-coated copper powder, AgCu0204, from Ames Goldsmith was down-selected due to its high conductivity and stability in air and the direct write printing method was used. Several insulative materials and processes were evaluated for print resolution and temperature capability. 3D printing of ULTEM 1010 using FFF was down-selected. Feasibility was demonstrated for integrating direct write additively manufactured conductors with an FFF additively manufactured insulative sleeve. Additional architectures can be pursued to optimize the processing parameters and testing as well as to further evaluate the durability and performance of the system.

### **3.1.9 Summary**

The ORNL team had successfully demonstrated a new additive manufacturing scheme for proof-of-concept stator laminates realized by SLM of Fe<sub>3</sub>Si steel followed by EDM slicing and a rotor using SLM. The printed laminate matched conventional steel laminate in terms of functional performance. However, the minimum thickness of laminate was limited by the EDM slicing technique (1.4 mm). A key challenge with using the SLM method and EDM slicing is laminate warping. Further, using SLM to individually print thin laminates would eliminate cracking from the temperature gradients between the different layers during printing. If multimaterial printing of stators using electrical steel with insulation material is made possible, EDM slicing could be eliminated, and even thinner laminations could be realized. The team also demonstrated post-magnetization and overmolding techniques for printed magnets and electrical steel. Magfine (mixture of NdFeB and SmFeN) powders in a PPS matrix were compression molded into a SLM Fe<sub>3</sub>Si steel rotor with the energy product of the overmolded sample reaching 8.324 MGOe after post-magnetic-field annealing. Thus, higher-performance magnets can be manufactured into generator rotors without the need for resin, which is typically used for bonding sintered NdFeB magnets. The performance of the overmolded magnets degraded slightly due to the surface oxidation of the magnets during compression molding. Hence, further optimization of the use of inert gas during compression molding is needed. Also, post-magnetic-field annealing of the overmolded samples is needed for final use.

The NASA Glenn team successfully demonstrated the multimaterial printing of conductors using DIW and FFF. Yet, the best conductivity achieved was with silver conductors demonstrating up to 35% IACS. A cost-versus-performance trade-off was notably observed with silver-coated copper conductors. Direct-ink writing these conductive pastes onto an insulation sleeve allowed for fill factors exceeding 70%. As new high-temperature insulation materials continue to evolve

along with printing techniques, the sleeve wall thicknesses and printing can be further optimized to achieve higher fill factors. The following will further improve electrical conductivity of the pastes: higher solid loading, secondary additions for higher conductivity such as graphene and carbon or boron nitride nanotubes, and advanced curing using photonic sintering. Future work could be conducted to optimize print quality, integrate full sleeves into stator slots, and characterize the performance.

While multimaterial printing was addressed to a limited extent as part of this effort, future rapid advancements in additive manufacturing are expected to enable higher-temperature materials, higher resolutions, and more directly integrated additive manufacturing processes (e.g., multimaterial and all-in-one machine printing).

## 4 Gap Analysis and Future Work

The United States is slated for growth in manufacturing infrastructure for both offshore and onshore wind turbine components across the country (Laura Lightbody and Shane 2023). However, this growth faces several hurdles, including limited flexibility in production, that restrict the innovations in design needed to realize the next generation of lightweight wind turbine generators with reduced demand for critical materials. The MADE3D project sought to address some key challenges by advancing design, materials, and printing processes that not only enable lightweighting and reduce dependence on critical materials but also pave the way for future on-demand manufacturing. While promising, 3D printing for wind turbine generator manufacturing needs additional R&D investment in several areas.

### 4.1 Multimaterial Design for Wind Turbine Generators and Designing for Printability

Limitations in conventional approaches to wind turbine generator design optimization can be attributed to some extent to limited modeling capabilities available in commercial magnetic FEA software. The design tools developed through this project can overcome those limitations by seamlessly integrating with advanced machine learning to explore a wide range of novel features and shapes. These could include bio-inspired or other organic forms that can be more powerful and can lead to significant improvements in generator design and development time. The asymmetrical, multimaterial pole designs investigated through this project demonstrate that a new untapped design freedom exists in wind turbine generators considering their predominantly unidirectional operating conditions. This can be transformational to the future design of wind generators and electric machines to achieve the best material efficiencies and functionality with reduced critical material usage and shall be particularly attractive from a supply chain standpoint. The designs can also be enabled by other advanced manufacturing technologies (injection and compression molding, micromachining and high-power laser cutting as well as spark plasma sintering), should they mature far enough to enable multimaterial integration capabilities.

#### 4.1.1 Opportunities for Designs in Wind Turbines

Some of the advanced designs and design methods that were identified by leveraging 3D printed magnet materials can be integrated into existing production and assembly lines for wind turbine generators and have end-of-life pathways for recycling and reuse. These include minimal topological alterations to existing wind turbine generators that could allow easy retrofitting of some components as well as facilitate reuse and remanufacturing. The proposed design methods can easily lend themselves to include additional functional parameters during the optimization such as controllable magnetization angles to fine-tune the magnetic field distribution to improve efficiency and torque output and to reduce cogging torque.

##### 4.1.1.1 Design for Retrofitting

It is possible to directly retrofit an existing outer rotor radial flux machine with a 3D printed asymmetric optimized rotor with multimaterial magnets with up to 35% less rare earth magnets. Magnets can be directly printed over a layer of sintered magnets, and the magnet stack can be attached to the printed rotor by glue or insert-molding. The different layers can feature different magnet compositions. The method for multimaterial design can be implemented on different configurations of generators including IPM topologies in large direct-drive generators and

surface-mounted permanent-magnet generators such as those used in medium-speed wind turbine generators.

#### 4.1.1.2 Design for Recyclability

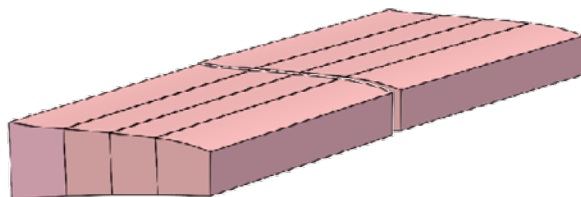
Although these designs were not specifically assessed for recyclability—because the binder used in the magnet serves as the main adhesion mechanism—it may be easier to recover the magnets in the event of a failure or at the end of life. Unlike sintered magnets, the physical separation between NdFeB particles and the binder allows for easier manipulation during the recycling process using methods such as cryogenic milling and remanufacturing new magnets by powder compaction (Gandha, Ouyang, et al. 2019).

#### 4.1.1.3 Design for In Situ Magnetization

In situ magnetization during 3D printing is emerging as a promising area for achieving functional improvements in performance (Suppan, Huber and Mathauer 2022) (Sarkar, et al. 2020) (Paranthaman, Post and Sales 2024). The ability to control the magnetic properties during printing opens doors for more advanced designs. For example, a single printed magnet could have sections with varying magnetic strengths (such as graded magnets) or even different magnetic polarities. The design tools developed in this project can be extended to control and optimize the magnetization orientations.

### 4.1.2 Scalability of Optimized Designs

The designs explored in the present study considered two different power ratings (15 MW and 15 kW), and the applications have different target specifications and design constraints in the process. For instance, the 15-kW Bergey design uses a double-sided support structure for the rotor, whereas the 15-MW baseline generator uses a single-sided support structure for the rotor. From a design perspective, it may be possible to implement an asymmetric pole design on the 15-MW generator as well; however, the optimization process needs to be reevaluated to account for different operating conditions including careful consideration of all loads from the turbine that affect structural design, the demagnetization strength achievable with larger printed magnets, and saturation flux densities for a larger core. To reduce design uncertainty, modularizing printed parts can be considered in the optimization of larger parts. Further, larger direct-drive generators mostly feature laminated or segmented permanent magnets; therefore, the shape optimization should consider the use of multiple smaller segmented magnets instead of a single, large magnet block to allow for more flexibility in design, minimize eddy current losses, and potentially reduce the risk of demagnetization (Figure 60). Modular design optimization can also help overcome the dimensional limitations of 3D printers as identified in Section 4.3.



**Figure 60. Shaped, segmented magnets that can be printed to realize larger dimensions in larger generators**

### 4.1.3 Gaps

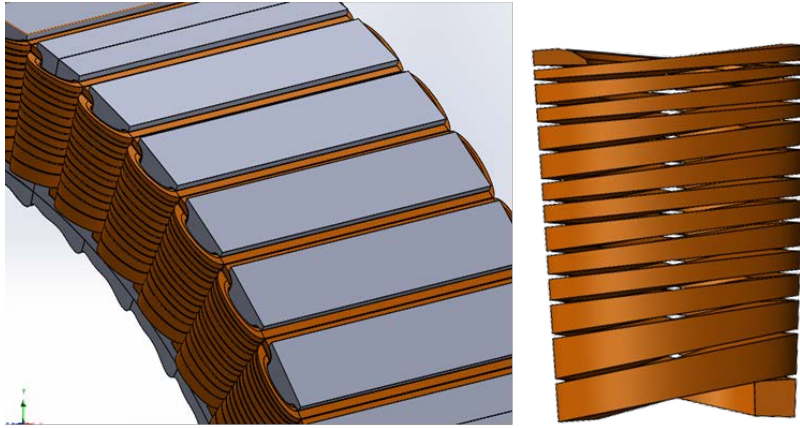
The performance estimates for the optimized designs presented in this work were solely based on 2D modeling with these assumptions:

- The properties of printed materials (based on measurements on test coupons for magnets, a laminate sector for stator, and a cast rotor core) and the properties of final printed magnet poles and lamination stack will be similar.
- Conditions will be ideal during the printing process and will be repeatable.

Assuming uniform material properties can be a significant oversimplification depending on the quality of the printed part. No manufacturing-induced changes in design, for example, deformation from printing (the heating and cooling cycles in 3D printing can introduce residual stresses in the final part) or changes in magnetic flux density or magnetization, were considered during modeling. Processes such as FFF introduce different types of stress because of layer-by-layer buildup and curing mechanisms; stress also depends on the complexity of the geometry with varying thicknesses and orientation. Printing parameters such as cooling rate, infill density, and layer thickness can also significantly impact stress range from a few megapascals to several tens or even hundreds of megapascals. While it is difficult to generalize and quantify the impact of such changes on the design for additive manufacturing, the optimization can be greatly improved by a data-driven design approach, where multiple measurements on printed parts with different print parameter settings can be used and an optimal design can be selected by a sensitivity analysis to changes in material properties and validation by measurements on as-printed parts.

#### 4.1.3.1 3D Modeling and Analysis

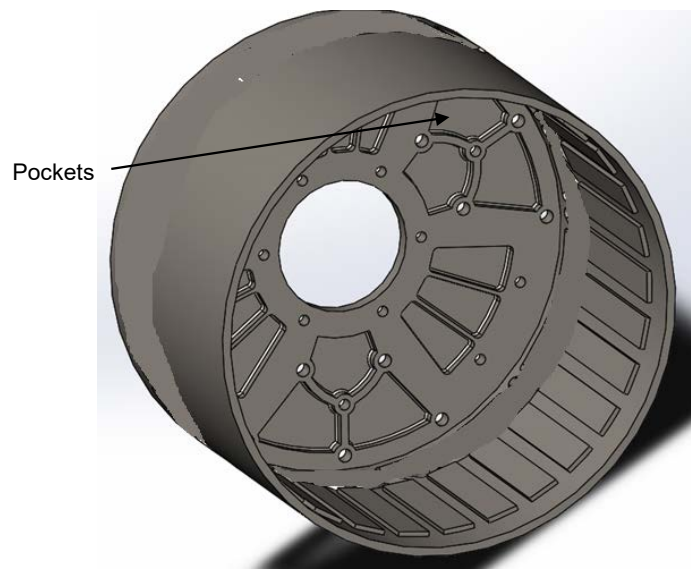
It is also possible that the mechanical and magnetic strength of 3D printed magnets can exhibit a certain degree of anisotropy depending on printing direction, which requires careful consideration. It is important to account for changes in material behavior in printed parts. Particularly for shaped conductors such as those demonstrated in this project (Figure 61), it would be crucial to study the effect of reduced end winding length and change in geometries on torque ripple as well as thermal management. Because 2D modeling typically neglects end effects, 3D modeling is necessary to capture these effects more accurately. 3D modeling can also help analyze and incorporate anisotropic material properties and how the magnetic material behaves differently in different directions. The thermal modeling and analysis of the designs studied in the project were also limited to steady-state 2D simulations. Transient studies along with 3D modeling would also help researchers better understand the thermal behavior with any material anisotropy and also investigate novel heat exchange mechanisms.



**Figure 61. 3D model of shape-optimized conductors**

#### **4.1.3.2 Structural Design Optimization**

The structural optimization of the 15-kW generator design primarily focused on minimal alterations to the existing rotor because of constraints introduced from operation and maintenance. While several new features were studied, these options were later discarded because no holes or openings were allowed in the geometry of the disk (other than the necessary bolt holes) (Sethuraman, Glaws, et al., *Advanced multimaterial shape optimization methods as applied to advanced manufacturing of wind turbine generators* 2024). Thus, standard dimensions such as wall thicknesses were only parameterized and optimized. The inside of the rotor had to be constrained to be as uniform as possible, which limited optimization. However, if such constraints could be relaxed, additional features such as the pockets shown in Figure 62 can be introduced to help shave off more material from the rotor support structure. Such features could be better parameterized through shape optimization and could also be explored through topology optimization with constraints imposed on boundaries for material removal. This study evaluated only the rotor design from a structural stiffness point of view. For the stator with shaped back iron, the lamination stacks are expected to be segmented construction with each segment representing 1/10 of the full machine. A shaped back iron will also need a new support structure design; such a study was not considered for the present scope and can be evaluated as part of a future study using advanced optimization techniques.



**Figure 62. New features that can be introduced for further lightweighting**

#### **4.1.3.3 Thermal Design Optimization**

Although not part of the scope, it may be possible to integrate cooling channels directly within the machine's core or with the windings by printing. New possibilities of magnetically optimal designs with better heat dissipation may be possible at the same time. This can eliminate the need for separate cooling components and make heat transfer more efficient. Further, shape optimization methods can be enhanced to simultaneously handle magnetic materials and thermal materials with high thermal conductivity, and to integrate other thermal management components directly in the machine design.

#### **4.1.3.4 Support Structure Requirements**

Another gap in the advanced optimization of the generator is the consideration for support structures during 3D printing, especially for electrical conductors that could limit geometric freedom. While not always cumbersome, removing support structures is an important post-processing step that can be challenging especially with complex designs and shapes that can leave behind rough surfaces that will need additional finishing, impacting the final design and possibly entailing additional costs. Also, certain printing techniques such as SLM and sand printing require a certain minimum feature size. Very thin walls or tiny details from the optimized design might not be achievable and might introduce constraints when designing for printability. This is particularly true for sand printing and large component casting for larger generators.

## **4.2 Materials**

While 3D printed magnetic materials hold promise, significant improvements to the properties of printed materials are needed (especially for hard magnets and electrical conductors) with performance demonstrated at scale by prototype fabrication and validation. Research efforts on processing powder materials especially suitable for 3D printing in electric machines are gaining momentum with several powder suppliers emerging both in the United States and around the world. Companies such as KBM Advanced materials (KBM n.d.) and Elementum 3D process

specialized copper-based and aluminum alloys. 3DREMAG (3DREMAG n.d.) and soft magnetic alloy projects (3D Printing.com n.d.) are focusing on upscaling and introducing customized hard and soft magnet powders suitable for use in electric machines. VTT Research center in Finland and Siemens in Germany have overseen the production part qualification processes of a soft magnetic steel stator for an electric motor. As of 2024, Elkem is introducing the powder to the market for future commercial production (3D Printing.com 2024). As of yet, achieving consistent powder particle sizes has been the main challenge (Imeson 2024).

#### **4.2.1 Hard Magnet Material**

This project demonstrated NdFeB+SmFeN+PA12 as a promising candidate composite material with zero critical rare earth magnets. It may be noted that of this composition, elements such as samarium and neodymium are rare earth, but dysprosium and terbium are identified as “critical” rare earth materials by the U.S. Department of Energy (U.S. DOE 2023). However, achieving magnetic properties that are comparable to or superior to sintered NdFeB magnets with rare-earth content remains a hurdle because the pellet-based FFF technique requires a high-volume loading fraction of magnet powders during the printing process. Further, the available NdFeB powders used in polymer-bonded or sintered magnets are not designed for direct use in specific 3D printing techniques. For example, the LPBF technique will need strip-casting, hydrogen decrepitation, and jet-milling and plasma spheroidization (Riegg, et al. 2021) for FFF printing, which typically requires precisely controlled particle sizes and microstructure because uneven particles can clog the print nozzle or lead to weak interlayer adhesion in the printed magnet. Further, sintered or bonded NdFeB powders may not flow smoothly through the nozzle, causing feeding issues and inconsistent printing. Powders should also be more resistant to oxidation and require lower processing temperatures and inert gas atmospheres. The highest achieved Curie temperature for printed magnets has been 312°C. The FFF process may also result in uneven grain size and random grain orientation and porosity in printed parts, which can affect the grain alignment. While heat treatments and annealing under magnetic fields of >1 T can help to refine grain size and improve the degree of grain alignment, more R&D is needed in the area of controlling microstructure for a stronger magnetic field. Larger wind turbine generators at temperatures as high as 120°C require magnets with higher coercivity. New methods for improving the magnet powder’s thermal stability, with coating before compounding, are also being investigated to improve overall magnet performance at higher temperatures (Damnjanović, Milošev and Kovačević 2024). Control of grain orientation and alignment during printing are evolving needs as FFF methods mature.

#### **4.2.2 3D Printed Electrical Conductors**

Achieving 100% IACS by printing is still an ongoing research activity. A major difficulty is attributed to the starting compositions of alloys used including copper, aluminum, and silver. Aluminum alloy powders tend to oxidize readily, and maintaining an oxide-free surface in a printed conductor is crucial. Further, aluminum powders are difficult to handle because of their potential for ignition during printing. Achieving high density using powder-based technology for copper has been challenging because of porosity issues. Silver-coated copper conductors that were demonstrated as part of this project required the use of additives such as copper in the ink formulation to prevent oxidation issues. For the DIW method developed by NASA Glenn, higher solid loading may be achieved using secondary additions for higher conductivity such as graphene and carbon or boron nitride nanotubes, and advanced curing using photonic sintering.



Achieving both printability and the mechanical strength needed for wind turbine generators is a research challenge with the best printed conductors because they experience high operational mechanical loading as well.

### **4.2.3 Soft Magnet Materials**

Fe<sub>3</sub>Si- and Fe<sub>6</sub>Si-based soft magnetic materials have been successfully printed near net shape, crack-free, and with full density using an indirect additive manufacturing process as part of this project. Similarly, SLM has been used to print near-net-shape Fe<sub>3</sub>Si stators. However, further work is needed with multimaterial printing where ceramic insulation layers can be introduced into Fe<sub>3</sub>Si layers. This will eliminate the need for EDM slicing and post-processing of additive manufacturing-fabricated electrical steel. The SLM process had no coarse grain orientation or texture formation in electrical steel. Soft magnetic materials with nanocrystalline structures can possess substantially higher permeability (2–10 times) and much lower core loss (5–10 times) than the current state-of-the-art, coarse-grained electrical steel (Willard and Kniping 2012). This would provide high-power generation efficiency and low heat loss, enhancing the performance of the electric motors and generators. However, the state-of-the-art manufacturing methods typically involve either melt-spinning or intense cold rolling followed by high-temperature consolidation (Babuska, et al. 2019), which requires significant post-processing and is 5–10 times costlier than the conventional cold-rolled silicon steel. Moreover, nanocrystalline materials are so brittle that currently there is no viable way of deploying nanocrystalline materials for motor applications. New additive methods and strategies for processing nanocrystalline soft magnetic materials are needed. It is necessary to develop print conditions to orient grains or texture formation in Fe<sub>3</sub>Si and Fe<sub>6</sub>Si that can reduce the losses significantly. Also, new powder production methods are an ongoing area of research for both Fe<sub>3</sub>Si and Fe<sub>6</sub>Si powders used for printing the core. They shall allow for good flowability and deposition during printing with the help of additives or surface modifications to the powders could potentially improve their printability without compromising the final magnetic properties.

## **4.3 Lab-Scale Printing Demonstrations Versus State-of-the-Art Industrial 3D Printers and R&D Needs**

The team interviewed at least 15 printer OEMs both domestically and overseas to assess the current commercial printing capabilities and their technical readiness to advance the design, materials, and manufacturing that have been developed through this project. We also assessed the methods developed by ORNL for transferability to commercial printers and required process optimization needs by comparing the properties of printed parts against conventionally manufactured parts for the Bergey generator. We also considered the potential for scaling to larger wind turbine generators. A summary of the state-of-the art commercial printers and lab-developed printing processes is presented in Table 29.

The dimensions of key components for a 15-kW generator are provided in Table 26. Printing a round cylindrical part would require a build envelope of ~611.58 mm x 611.58 mm x 200 mm. CAD models of optimized stator laminate and rotor with shaped magnets were shared with some of the printer OEMs to solicit feedback on printability, challenges, and opportunities. We investigated both direct and indirect additive manufacturing methods to print the optimized components of the 15-kW generator with the potential to scale to parts in large generators such

as the IEA 15-MW generator (Gaertner, et al. 2020), whose main dimensions are also listed in Table 27. Such a larger generator would entail a build envelope of at least 11 m x 11 m x 2.3 m.

**Table 26. Dimensions of Main Components in 15-kW and 15-MW Direct-Drive Generators**

Dimensions of the Main Components	15-kW Generator	15-MW Generator
Rotor outer diameter and thickness	~612 mm	10,400 mm
Axial length	200 mm	2169 mm
Magnet dimensions (W x H x L)	25 mm x ~5 mm x 150 mm	129 mm x 59 mm x 2169 mm (made in multiple segments)
Stator outer diameter (mm)	570.4	10,100
Stator inner diameter (mm)	455	9,120
Coil length, single turn	2 mm x 150 mm + 30 mm end turn (2 times 10% of stack length)	2169 mm + 434 mm (2 times 10% of stack length)

### 4.3.1 Challenges With Scaling Lab-Scale Printing Processes for Large Generator Manufacturing

#### 4.3.1.1 Stator Laminates and Rotor Core

As was discussed in Section 3, the main challenges with printing stator laminate parts using laser-based additive processes included handling temperature gradients and cracking as the laminates got thinner. Although material printing using composite feedstock partially offset the challenge, further optimization is needed to improve the saturation flux densities and minimize the lamination thicknesses further. We found the properties of the SLM printed 6-in. rotor can and stator laminate for a sector to be comparable to that of conventionally manufactured rotor and stator. We identified the following gaps for printing rotors for megawatt-class wind generators:

- Although FFF-based printing of large electrical steel parts may be possible with a BAAM printer, the magnetic properties of the steel parts can be weaker. Printed large rotor parts using laser-based approaches can crack parts because of stress formation during printing. This could limit the printable size and type of materials. Currently, SLM printing is limited to 1 m x 1 m x 2 m in terms of build volume. With lab-scale laser printing, energy consumption is typically of the order of  $5.7 \text{ E}+8 \text{ J/kg}$  (Faludi, et al. 2017). Printing larger rotor parts can lead to high power consumption, which can increase the costs of printing using laser printing.
- Spherical particles are needed as the feed. This requirement could lead to difficulty in accommodating nonspherical geometries for the laser additive process. Also, the laser printing process is slower than both the binder jetting and sand mold casting processes. These alternate methods do not require spherical particles for printing. Therefore,

alternate methods such as indirect additive manufacturing methods will be needed to print large rotors suitable for megawatt-class wind generators.

#### 4.3.1.2 *Permanent Magnets*

The main gap associated with BAAM-printed permanent magnets is their weak energy product (up to ~23 MGOe versus 52 MGOe with sintered magnets). The primary cause is the need for significant quantities of thermoplastic polymers such as nylon during printing. However, the printed magnets have several favorable properties such as high corrosion resistance, high resistivity (almost zero eddy current losses), thermal stability of up to 175°C with polyphenylene sulfide polymers, and lower mass density compared to sintered NdFeB magnets. Scaling up the BAAM process for larger magnets can be challenging for the following reasons:

- Large volumes of the pellets (NdFeB powder and binder) need to be handled. Consistent material flow and quality throughout the large prints and consistency in repeatability are the main challenges and are crucial for magnet performance. Further research is needed on material characterization (particle size distribution), homogeneity of binder and magnet distribution, and material rheology. Large-volume pellet production, material feeding systems, powder bed management, and improved quality control are needed to address these challenges.
- Post-magnetic-field annealing is challenging with larger printed magnets because of their scale and the difficulty in ensuring uniformity in magnetization using high magnetic fields. In situ magnetic field annealing during printing would be needed, which can increase costs.
- **Strength and Anisotropy:** Large printed magnets may not yet achieve the same level of strength and magnetic anisotropy (directional alignment of magnetic properties) as traditionally manufactured magnets, and strength and anisotropy are crucial for wind turbine performance. The mechanical properties of coupon-sized printed magnets in the lab are low in the build direction (20–30 MPa versus 65 MPa for sintered magnets). That strength may not be adequate for medium-speed permanent magnet synchronous generators. Further research is needed to improve the mechanical properties through suitable additives such as carbon fibers.
- Scaling insert or overmolding of bonded permanent magnets onto rotors presents several challenges. These include achieving precise placement of magnets within the rotor while maintaining a uniform air gap, achieving uniform magnetic field distribution, and achieving robust adhesion.

#### 4.3.1.3 *Electrical Conductors and Insulation*

The NASA Glenn team demonstrated the feasibility of integrating conductor printing with insulation materials with fill factors exceeding 70% using DIW and FFF. Although silver conductors were demonstrated to have the highest conductivity with 35% IACS, comparable to aluminum, high costs could be a major impediment. The approach is identified as TRL 3 (low) and needs further optimization to improve the electrical conductivity of conductors with higher solid loading and advanced curing techniques. While aluminum was not specifically pursued because of oxidation risks, successfully multiprinting aluminum with high-temperature insulation materials with thin sleeve wall thicknesses can enable the advanced designs that the NREL team investigated. Developing low-cost conductive pastes that meet the demanding electrical and

mechanical properties needed for large electric machines will be necessary. Finally, current DIW systems such as those used by the NASA Glenn team are designed for smaller workspaces. Creating a large-scale printing platform integrating high-temperature treatment will be needed along with research and development efforts to achieve true multimaterial printing production of conductors and insulation.

#### **4.3.2 The Potential for Stator Lamination Manufacturing and Rotor Core Manufacturing Using Commercial LPBF Systems**

The Bergey design uses segmented lamination stacks that are assembled to form the stator, but production of the individual laminations requires tight tolerances. We assessed some commercial printers for their ability to handle different materials or material compositions, dimensional form and positional tolerance and repeatability that are needed to achieve the required electrical, magnetic, and mechanical properties for electrical steel. Conversations with Beehive Industries and FreeFORM Technologies who specialized in LPBF systems informed us that the largest print bed dimensions available were 400 mm x 330 mm x 250 mm. Renishaw and ADDMAN handled the largest LPBF machines with dimensions of 250 mm x 250 mm x 250 mm. One major reason for the printer industry's slowness in scaling the print beds is the lack of demand and their increased focus on smaller specialty parts made from high-value metals such as titanium, versus electrical steel, which is relatively cheap. The minimum layer thickness possible was 50  $\mu\text{m}$ , which is thicker than 0.35 mm thickness needed for stator laminates. A solution that was discussed was to print the entire stack of laminates as a solid block and then use EDM to make it the required thickness, but the main challenge they anticipate is distortion of the printed laminate from the stress of heating the wire during machining. Further, heat treatment (hot isostatic pressing) would be needed to achieve 95% density and achieve material properties that are comparable to traditionally manufactured materials. The main challenges were broadly identified as follows:

**Material inexperience:** These printer OEMs had no prior experience in printing the AISI-1020 steel used in the 15-kW generator; therefore, we could not ascertain the printability for rotor core using their commercial printers. It may be possible to test the process using stainless steel 316 alloy powders such as those demonstrated by the ORNL team, but the process needs further optimization.

**High capital costs:** Scaling up the printing to larger parts for larger direct-drive generators with a build envelope of 11 m x 11 m x 2.3 m can entail capital expenditures on the order of \$3 million.

**Polymer-metal incompatibility:** Printing polymer-bonded magnets may not be feasible because of thermal expansion issues between metals and polymers. Mixing powders increases the costs and reduces the recovery of powders.

**Powder-related issues:** Because the powder bed fusion process will need abundant raw materials (steel powder), this can translate into high raw material costs. Handling large quantities of steel powders can also be a challenge because steel powders can oxidize and form condensates that will become unsuitable for printing. Large quantities of metal powders also pose significant fire hazards. The challenges of printing large-scale parts are optimizing laser controls and energy

consumption and internal stresses in the parts. Therefore, the team reached out to other commercial laser-based printing technologies.

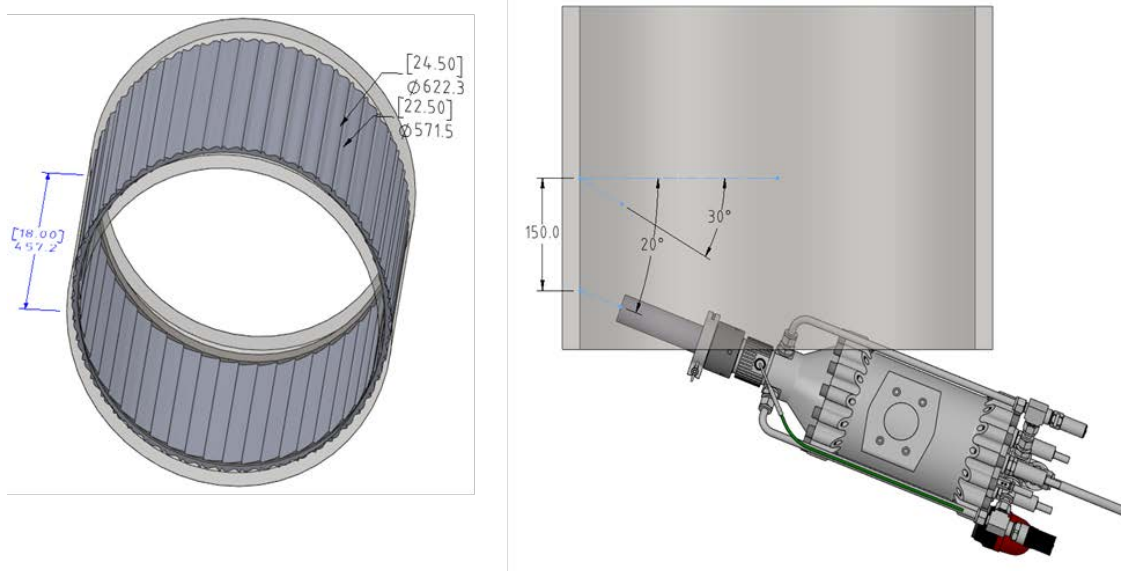
Mitigating these challenges will need a carefully phased approach to scale up, allowing for learning and optimization through a feasibility study. For example, investing in a modular system or a slightly larger build envelope to experiment with different process parameters can help systematically minimize risks and costs associated with scaling up and integrating energy-efficient laser systems. Collaboration with powder metallurgy experts and powder manufacturers is also needed to develop and integrate safety protocols for handling and storing large quantities of metal powders.

Considering these challenges, the team also investigated alternative laser-based approaches, including direct energy deposition. Although no formal quotes were available, ADDMAN's estimate to print the core using direct energy deposition was \$65,000 with magnets. The team reached out to Sciaky Inc., a company that makes one of the largest direct energy deposition printers. The largest work envelope is 5.8 m x 1.2 m x 1.2 m, and the feedstock is wires. This technique had the fastest deposition rate and could be considered a replacement for rough forging or casting. The team learned that highly weldable low-alloy steels work well for the process. However, the method itself necessitates extensive machining and will also need heat treatment to reach the final dimensions. The final properties of the printed part are expected to be similar to fully annealed structure. The OEM had no experience in printing AISA-1020 grade steel, but their estimated costs to print the shaped rotor core was \$20,000 with the majority of costs going toward R&D efforts needed to print the shape to the final dimensions with the required tolerance. The costs are expected to progressively come down with time, with an estimate of \$2,200 per rotor can. A major challenge to scaling the direct energy deposition process to 9 m and larger was the energy needed to maintain an inert argon atmosphere in a large chamber. A summary is presented in Table 29.

#### **4.3.3 Using Large Commercial Cold Spray Additive Technology for Printing Both 15-kW and 15-MW Electrical Steel Cores**

The team reached out to Titomic, an Australian-based cold spray printer OEM. The largest print envelope is 9 m x 1.2 m x 1.2 m, which is still smaller than the typical dimensions needed for printing rotors for large direct-drive generators (see Table 26). However, the OEM perceived that scaling to larger platforms may not be a challenge. They mentioned the possibility of using carbon-reduced iron powder for printing the rotor, and the process can be thought of as a replacement for rough forging or casting but cannot reach the dimensions of the finished part and would still require heat treatment and machining. They estimated ~\$20,000 for printing the rotor, excluding machining costs and project costs (assuming batched heat treatment). Further testing will be required.

Titomic thinks that cold spray is more economical for high-value metals. Cold spray is a solid-state process, and no microstructural changes of the material are anticipated. A team of researchers at National Research Council Canada has demonstrated the potential to print magnets using cold spray printing (Fabrice Bernier, et al. 2022). The process can print metal matrix composites and can include insulation between layers. For the Bergey machine, building in-to-out is preferred. For internal coating, the reach is limited to 20° for the nozzle angle as shown in Figure 63.



**Figure 63. Optimized rotor can and reach possible by internal spray coating**

#### **4.3.4 Indirect Additive Manufacturing of Rotor Core**

The team interviewed engineers at Humtown Additive and International Casting Corporation on the possibility of sand printing a mold of the shape-optimized rotor followed by traditional casting of 1020 steel. The work envelope for their sand printers is 1.8 m x 1.0 m x 0.7 m. The engineers advised the team to reconsider the material choice because the large diameter of the Bergey rotor core presents challenges with freezing (solidification) during the casting process for 1020 steel. Further, the printed mold can shrink by 1/8 in. The alternative raw materials they suggested included ductile iron or cast iron that allows for easier curing and better flow. Separate mold analysis would be necessary to determine gating requirements from solidification modeling. This method was the cheapest at \$3,500 for engineering time involved in mold analysis and the cost to cast the material. In terms of scalability, GE Renewable Energy is already pursuing this method for manufacturing hub and generator support structures for their Haliade-X offshore wind turbines under the Advanced Casting Cell project (reNEWS.BIZ 2021). Additive molds for optimized designs also help reduce machining time and material costs. Using 3D printing technologies means that molds can be produced on site, which reduces transport costs and improves the CO<sub>2</sub> balance of wind turbine production. Voxeljet (Voxeljet n.d.) is leading the development of BJAT-based sand 3D printing to produce sand cast molds with a diameter of up to 9.5 m. They are working with Hodge Foundry, Inc. (Foundry n.d.) to optimize mold printing to speed up production times, minimize binder and activator use, and improve thermal and mechanical behavior during casting.

#### **4.3.5 Magnet Manufacturing Using Commercial FFF Printers**

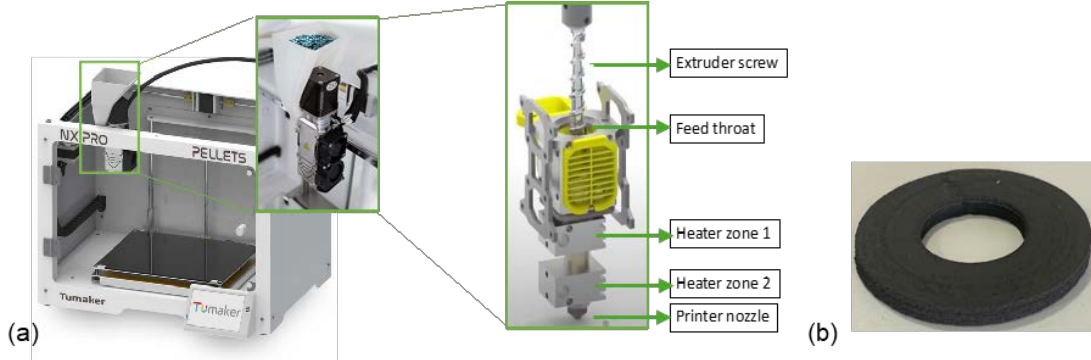
While several commercial FFF printer manufacturers are available (Schwaar 2024), a select few use pellet-based feedstocks similar to ORNL's BAAM printer. The largest FFF printer is made by the Swedish company Industry, whose MAGNUM printer has a build envelope of 1.5 m x 1.2 m x 1.2 m (Industry n.d.). The printer features an air-cooled nozzle with print speeds of up to 600

mm/s depending on the material. Colorado-based 3D Systems is another FFF printer manufacturer with their Titan printer. Conversations with both these OEMs helped us learn that neither OEM has prior experience with printing magnet-like material and will require a separate R&D effort to optimize print parameters and reengineer their printers. However, considering the available build envelopes, if feasibility can be established similar to the BAAM printer by Cincinnati Inc., it may be possible to fit multiple magnets on the print bed while reducing the production time. As a trial process, composite pellets of SmFeN + NdFeB + Nylon pellets were sent to Tumaker, a Spanish printer OEM, and to Industry. The Tumaker Pellets Pro printer, shown in Figure 64, is a desktop-scale machine with a three-axis gantry system and a build volume of 290 mm x 180 mm x 200 mm. Industry was not able to process the pellets as feedstock. The magnet pellets were much harder than they had handled in the past and had a lower polymer loading (~95 vol% magnet loading with ~5 vol% polymer). However, Industry's MAGNUM printer comes with a minimum requirement of 50 vol% polymer in the composite feedstock. ORNL's BAAM system made by Cincinnati Inc. had no such limitations. Considering the high vol% loading of metal and thus a high mass density, MAGNUM's feedstock pumping mechanism could not handle heavy compounds. Furthermore, the pellets were of uneven sizes and there was a possibility that the extruders could be damaged from abrasion and clogging. Therefore, such a large FFF printer may have to be reengineered to be able to print magnets similar to what has been implemented on the BAAM printer. On the other hand, Tumaker did successfully print samples of bonded magnets and sent them to ORNL for characterization. Several print parameters were optimized to achieve optimum printability, and performance characterization of the printed samples helped independently verify the results from the BAAM printer. The print head on the Pellets Pro printer consisted of a NEMA 23 stepper motor attached to a single screw extruder system with two heater zones and replaceable nozzles. Printer settings were optimized in the following order:

- **Nozzle size:** A 2-mm nozzle was selected.
- **Heater temperature:** Because the magnet composite had only 7% weight fraction binder, the heater temperatures were set much higher than the melting point of the polymer to extrude consistently without clogging. The optimized temperatures were 230°C at the feed throat and 325°C at the nozzle.
- **Feed rate:** The feed rate (linear gantry speed) and extrusion multiplier parameters were interdependent. If the feed rate is too high, the printed sample would have unfilled gaps; if the rate is too low, overextrusion can lead to nozzle blockage and excessive flash on the printed sample. The feed rate was fixed at 500 mm/minute, and extrusion inconsistencies were adjusted using the extrusion multiplier parameter. A consistent width was extruded at the nozzle at the beginning of each print.
- **Print bed temperature and first layer height:** The print bed temperature was set at 70°C, and first layer height was set at 0.1 mm higher than layer height to encourage first layer adhesion.
- **Post-alignment:** Printed samples were post-aligned in the vibrating sample magnetometer at 300 K (room temperature). Figure 65 shows the hysteresis plots of the as-printed magnet with randomly oriented particles along with the post-aligned magnet under an applied magnetic field of 1 T. The density of the magnet is 5.207 g/cm<sup>3</sup>. As expected, after alignment, the remanence value increased almost twofold. The saturation magnetization was attained at a lower field strength as well. These results helped

independently verify the results from the BAAM printer. Tumaker-printed magnet properties are compared with that of BAAM-printed magnets in Table 27.

A key challenge of the Tumaker printer was the size limitation. The print volume was 295 x 185 x 200 mm<sup>3</sup>.



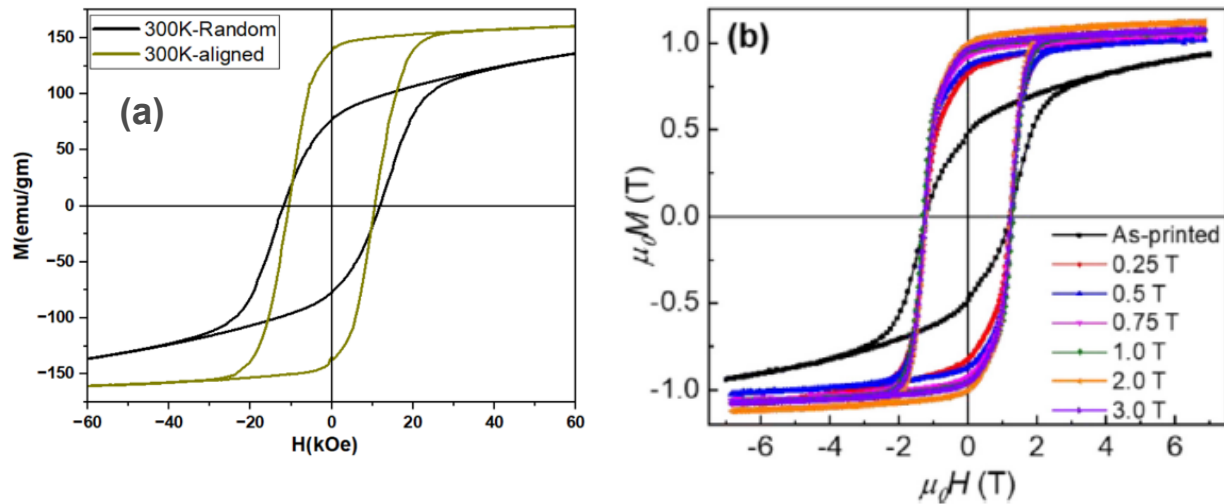
**Figure 64. (a) Small-scale pellet printer with exploded view of the print head extruder assembly. Print head has two heater zones, one close to the feed throat and the other close to the nozzle. (b) Sample magnet printed by Tumaker: 2-in. (50.8 mm) outer diameter, 0.75-in. (19.5 mm) inner diameter, and 4-mm thickness**

**Table 27. Optimized Print Parameters and Results on the Magnetic Strength Measurements**

Printer Settings for Tested Samples	Sample 1	Sample 2	BAAM Setting
Feed rate (mm/minute)	500	500	1,524
Extrusion rate (steps/mm)	E550*	E550*	Not applicable
Extrusion rate (mm/second)	-	-	25.4
Layer height (mm)	0.20	0.25	5.08
Extrusion multiplier	1.35	1.40	1
First layer speed (relative to default)	100%	100%	100%
<b>Measured properties</b>			
	<b>Average of samples</b>		
Mean remanence ( $B_r$ ) kG	9.48		9.4
Mean intrinsic coercivity, $H_{ci}$	10.65		10.34
Mean $BH_{max}$ , kJ/m <sup>3</sup>	124.14		140
Alignment	89%		>90%

\* E550: The extrusion rate of 550 steps/mm, measured in motor steps/minute was optimized using E-step calibration, where amount extruded by the controller is compared with actual amount extruded, followed by adjustment in extrusion rate as needed. The feed rate (linear gantry speed) and extrusion multiplier parameters are interdependent.

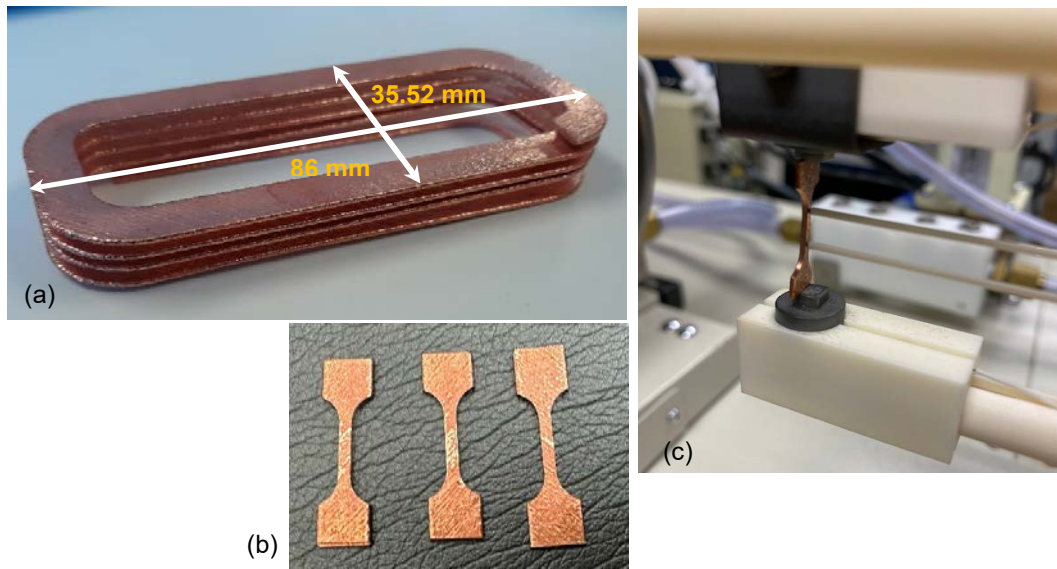




**Figure 65. (a) Hysteresis loop of as-printed (300 K as-printed) using Tumaker printer and post-aligned (300 K aligned) small-scale hybrid NdFeB SmFeN PA12 magnets and (b) hysteresis loop of BAAM-printed magnets of the same composition**

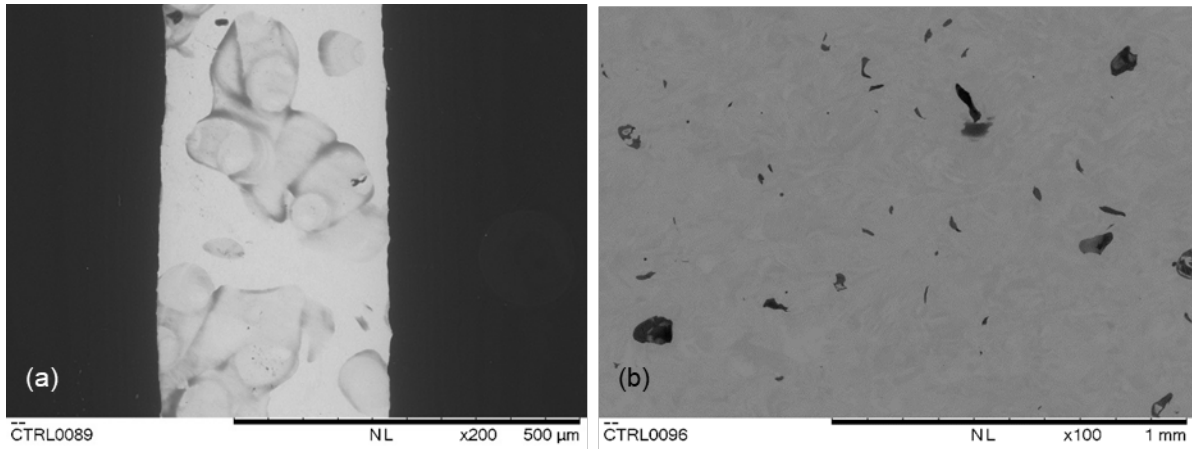
#### 4.3.6 The Potential for Printing Electrical Conductors Using Commercial Printers

The team reached out to printer OEMs Beehive Industries and Additive Drives to inquire about the feasibility of copper coil printing. Additive Drives make larger SLM printers with a build volume of 1 m x 1 m x 2 m that has been exclusively used for printing electrical conductors (pure aluminum and copper). Stack lengths greater than 1 m are possible with such a large build envelope. A print resolution of 50  $\mu\text{m}$  was possible. A sample CAD model was sent to both printer OEMs to ascertain the quality and the properties of printed copper. Beehive Industries used GrCop-42 as the conductor material, which was found to be not as conductive as pure copper. Oxidation issues exist because the print happens in an argon environment, and warping also occurs. Conductivities as high as 85% IACS were demonstrated. The printed coil might need post-processing with hot isostatic pressing to minimize porosity. The main limiting factor was the overhang angle:  $<45^\circ$  or greater relative to vertical. Additive Drives used a proprietary copper alloy that was marginally more expensive than regular copper wire (Figure 66a). For insulation, they needed to develop a custom forming technique and methods to verify performance by testing. To scale printing coils for larger machines, a big challenge is anticipated from the costs to fill the print bed with large quantities of copper powder. The costs are expected to scale linearly into production.



**Figure 66. (a) Sample coil printed by Additive Drives, (b) samples machined from printed coil, and (c) dog bone specimen being tested using ULVAC ZEM-3**

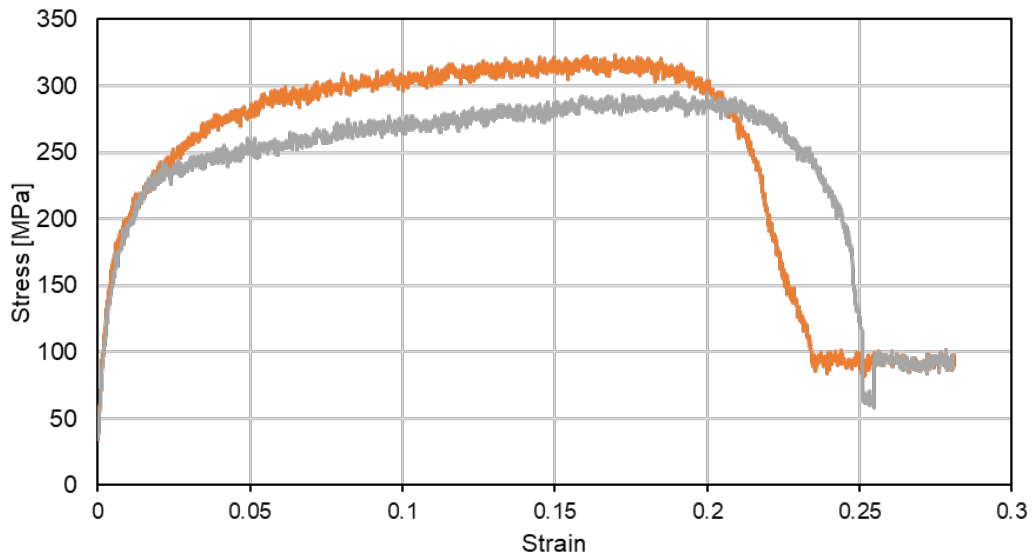
To measure electrical conductivity, the ORNL team machined a few samples from the printed coils (Figure 66b) and used the electric resistance measurement system ULVAC ZEM-3 (Figure 66c). The sample measured 75.31% IACS. A closer look at the microstructure on the top surface and the side edge revealed porous microstructures that may be responsible for the reduced conductivity. In terms of mechanical strength, achieving 100% IACS with SLM needs optimization to minimize porosity. The SEM images of both the surface and as well cross-sectional image of SLM copper is shown in Figure 67. SEM images indicate the presence of porosity. This could account for observing lower IACS copper values with SLM copper. The mechanical properties of SLM copper are reported in Table 28, and stress versus strain measurements on the dog bone samples (as shown in Figure 66b) are reported in Figure 68. The typical tensile strength of copper conductors is 200–360 MPa. The tensile strength of SLM copper is 295–323 MPa. Reducing the porosity in SLM copper in the future could lead to higher IACS values and improved tensile strength and approach that of conventional copper.



**Figure 67. SEM images of the microstructure of printed coils: (a) surface and (b) coil side**

**Table 28. Tensile Strength Measurements on Machined Samples**

Sample #	Tensile Strength (MPa)	Tensile Modulus (GPa)
1	323.75	235.78
2	295.41	211.23



**Figure 14. Stress versus strain measurements on machined samples**

**Table 29. A Summary of State-of-the-Art Commercial Printers**

AM Process	Materials	Part	Current Costs to Fabricate 15-kW Generator Components by Traditional Manufacturing	Costs to Fabricate Using Additive Manufacturing	Current Build Envelope and the Potential to Scale to Large Direct-Drive Generators Requiring Maximum Build Envelopes of (L x W x H) 11 m x 11 m x 2.3 m	Post processing	Material Properties	Source
FFF	Pellet and filaments of composites	Magnets	\$20/magnet pole for 15-kW generator	Unknown	1.5 m x 1.5 m x 1 m Maximum length ~4 m Dimensional accuracy is limited to nozzle diameter		Up to 10 MGOe	Industry (Sweden) 3D Systems, Stratasys Tumaker (Spain)
ORNL's BAAM FFF printer	Pellets	Magnets	\$20/pole for 15-kW generator	\$9/pole based on BAAM processing times	6 m x 2.3 m x 1.8 m Envelope suitable for magnet printing.		Up to 23 MGOe	BAAM
			~60/kg of NdFeB magnets for 15-MW generator	\$530.35 per four 300-mm blocks based on BAAM processing times				
Cold spray additive	Weldable metals	Rotor core and magnets	\$2,033 \$590 for can shell \$1,000 for magnets	~\$25,000 (rotor can—R&D)	~9 m x 2 m x 1 m Scaling is not a challenge for large direct-drive generators	Cannot reach final dimensions	Weaker for magnets (10 MGOe and 0.49 T based on literature)	Titomic
Direct energy deposition (electron beam)	Weldable metals	Rotor core	Estimates based on (Bergey 2021)	\$20,000 (R&D) ~\$2,200 (production)	Diameter up to 2.5 m. Scaling limited by costs and challenges with inert chamber	Annealing, heat treatment, and machining to final dimensions	Comparable to cast material	Sciaky, Inc.
BJAT for sand core followed by casting	Ductile iron	Rotor core		\$3,500/mold + casting cost	1.8 m x 1.8 m x 1 m 1020 steel unsuitable for casting cylinder	Machining	Comparable to cast metals	Humtown Additive, ICC, Trumbull Foundry

AM Process	Materials	Part	Current Costs to Fabricate 15-kW Generator Components by Traditional Manufacturing	Costs to Fabricate Using Additive Manufacturing	Current Build Envelope and the Potential to Scale to Large Direct-Drive Generators Requiring Maximum Build Envelopes of (L x W x H) 11 m x 11 m x 2.3 m	Post processing	Material Properties	Source
LPBF	Meltable metals	Stator lamination	\$2,769, includes cost of 412 stator laminations and assembly cost	No cost data (no prior experience). High capital expenditure and material costs	~0.254 m x 0.254 m x 0.350 m Scaling limited by inert atmosphere chamber	Heat treatment and possibly machining	Comparable to sheet laminations obtained by punching	Addman Group, Renishaw
LPBF	Proprietary copper alloy and aluminum	Copper conductor	\$740	\$3,900 per coil	~1 m x 1 m x 2 m	Heat treatment	75% IACS achievable for copper	Additive Drives (Germany)
BJAT of metals	GrCop	Copper conductor		\$21,000 per coil	Not known	Can result in warping	Inferior to conventional copper conductor	Beehive Industries, FreeFORM Technologies

## 4.4 Multimaterial Printing and Printing Costs

True multimaterial printing capabilities with most commercial printing methods are nonexistent and come with new challenges. For electrical conductors with SLM, a main challenge is in the material incompatibility between insulation materials and metals and in melting the different materials. As a result, printing copper conductors will still entail a multistep process of first printing the conductors and then completing a secondary process such as coating. Likewise, integrating thin laminations with interlayer coating is challenging because of the inherent heat involved in the process, minimizing the distortion with proper bonding between steel and the desired coating material. The insert molding technique developed in this project may be feasible for FFF of magnets on SLM printed electrical steel; however, challenges remain because insert-molded magnets yielded greatly reduced (as much as 39%) magnet properties. Further optimization of using an inert gas such as argon during insert molding is needed to eliminate magnet degradation. While design optimization can help minimize material use, it may not always translate to lower printing costs for large, complex geometries. Much focus has been on developing large-format printers as needed on high-value metals such as titanium alloys for use in the space industry. The exception to that is few efforts focused on advancing large-component manufacturing for generators, including the most recent Advanced Casting Cell project by GE Vernova (Voxeljet n.d.) that entailed the U.S. Department of Energy investing \$15 million to develop a large-scale sand printer and foundry. Integrating metals such as Fe<sub>3</sub>Si and Fe<sub>6</sub>Si and hard magnets as composite feed in commercial printers will require additional R&D and engineering investment to customize them for printing electric machine parts with the required functionality and acceptable or superior levels of performance compared to traditionally manufactured parts. The major cost-contributing elements for printing come from their capital costs, energy consumption, and post-processing. Table 30 lists some of the challenges in lowering the printing costs for some of the processes.

**Table 30. Challenges in Reducing Printing Costs for Some of the Investigated Technologies**

Cost-Contributing Element	FFF (Magnets)	SLM (Electrical Steel Laminations)	SLM (Copper)	Indirect Additive Manufacturing
<b>Capital expenditures</b>	Specialized extruders needed to handle the abrasive nature of magnetic filaments (often containing ceramic or metallic particles) Advanced control system and calibration procedure needed to ensure consistent magnetic properties	Large build volumes necessitate larger gas chambers to maintain inert gas environment to prevent oxidation, which can lead to higher gas consumption	High initial setup costs and time for first coil High reflectivity of copper necessitates specialized high-powered lasers	Robust material handling and control system; high-precision printing head Build platform Material handling (sand silos and storage)
<b>Energy consumption</b>	Optimizing temperature, extrusion pressure, and printing speed	Optimizing laser power and scan speed for achieving the best magnetic properties Heat treatment from post-processing to achieve desired properties	Optimizing laser power and scan speed	Creating large, complex sand molds can be time-consuming, resulting in significant energy consumption
<b>Material costs</b>	Potentially lower (uses support structures)	Specific grain structures are needed; powders need to be processed	Need of specialized copper powder alloy	Developing cost-effective, high-performance binders specifically designed for large generators
<b>Postprocessing</b>	In situ alignment and post-annealing with a magnetic field might be needed to improve alignment Printed magnet might require surface finishing (e.g., grinding or polishing) to achieve the desired dimensional accuracy Testing the strength, polarity of the printed magnet part	Support structure removal	Need for machining and polishing; stress-relief annealing Intricate coil designs will require more support structures, the removal of which can increase costs	Automation to remove printed sand molds from build platform for high-volume production

Cost-Contributing Element	FFF (Magnets)	SLM (Electrical Steel Laminations)	SLM (Copper)	Indirect Additive Manufacturing
	might involve specialized equipment			
<b>Suitability for large-scale production</b>	Low print speed	Low printing speed can translate to high energy costs	Printing multiple coils within the same build volume needed to achieve economies of scale	Developing high-speed printing heads or optimized layer thicknesses are essential for achieving high-throughput production Optimizing sand mixes for printability and reusability



## 4.5 Future Work

At the same time as this project, the following projects had already started in the area of 3D printing for wind turbine generators and electric machines:

- (2023) The Advanced Casting Cell project led by GE and Voxeljet (Advanced Materials and Manufacturing Technologies Office (AMMTO) 2024) for developing an end-to-end suite of tools for advanced casting of wind turbine nacelle components.
- (2021–2023) The EU-funded SOMA project (lightweight solutions for e-mobility by additive manufacturing for soft magnetic alloys) (EIT Raw Materials n.d.) and (2022–2205) MultiMag project led by VTT Research Center and Siemens AG Finland (Puukko n.d.) are aimed at 3D printing multimaterial structures for lightweight electric machines by optimizing topology and economizing the use of REEs in magnets.
- (2024–2027) The MagNeO project (MagNEO n.d.) (Europe 2024) is aimed at 3D printing novel magnet compositions based on AlNiCo and high-entropy alloys with higher coercivity for low-speed permanent magnet generators in wind turbines.

Considering these developments and the gaps identified in this project, as well as to better demonstrate the advantages of the advanced design and manufacturing capabilities developed through the project, we identified a few key activities as near-term, medium-term, and longer-term goals. These goals will systematically de-risk the processes to enable the MADE3D technology, transition it to higher TRLs, and encourage its industry adoption and market uptake both of which are needed to ultimately transform U.S. manufacturing of offshore wind turbines.

### 4.5.1 Advancing Design, Materials, and Additive Manufacturing for Wind Turbine Generators

The primary challenges in multimaterial optimization of generator designs for additive manufacturing are accurate representation of printed material properties in the design, modeling printing-induced changes, and including constraints imposed by the additive manufacturing process itself, such as support structure requirements and residual stresses. Further, considering that the different printing processes are at different stages of technological maturity, and the growing emphasis on measures to secure the supply chain for critical materials; it will be prudent to phase out the development process with a continued focus on rotor design. This should include reducing the use of rare earth magnets in the near term with a parallel development in de-risking and scaling up the technologies in rotor and magnet manufacturing. Additionally, extending multimaterial manufacturing of stator laminations along with conductors will help transform the manufacturing infrastructure needed for the next generation of lightweight wind turbine generators with fully domestically sourced raw materials.

#### 4.5.1.1 Near-Term Goals (2025–2027)

##### Design

- **Enhance performance accuracy by 3D modeling and analysis of shape-optimized generators:** A dedicated 3D modeling effort with increased focus on material definitions that are truly representative of as-printed magnetic parts is needed to accurately and fully functionally characterize the performance of the optimized generator design. This will help address any undesirable or unintentional anisotropy in printed magnets.

- **Ability to retrofit optimized rotor design:** Printing a full-scale, proof-of-concept rotor with shape-optimized magnets for a 15-kW generator and assembling the rotor in a generator production facility is needed to verify the ability to retrofit the redesigned rotor for the baseline generator. This step will also de-risk various aspects of printed asymmetric rotor pole design including any challenges in meeting dimensional tolerances of the optimized design and achieving perfect concentricity of the rotor with magnetized magnets.

## Materials

- **Increasing energy product of reduced rare earth/rare-earth-free magnets:** Investigate magnet materials with higher starting energy product (>45 MGOe) to achieve up to 25 MGOe energy product. This will have a significant effect on properties such as cost and efficiency of the prototype wind turbine generator.

## Manufacturing

- **Additive manufacturing of prototype rotor:** Direct efforts toward the indirect additive manufacturing technique that involves sand-printing the mold-shape-optimized rotor followed by conventional casting in a foundry. Mold analysis will be needed in tandem with methods to achieve optimal curing of carbon steel material.
- **Additive manufacturing of magnets:** Efforts shall be used to fabricate all pole pieces to achieve 25 MGOe energy product. Post-magnetic-field anneal all additively manufactured magnets to achieve high magnetic alignment. Optimize the printing parameters and magnetic alignment to ensure repeatability in terms of achieving the dimensional tolerances with consistent mechanical and magnetic properties for all magnets. Design suitable magnetization fixtures post-magnetize the magnets after assembly.

## Performance validation of optimized rotor design by dynamometer testing

- The fabricated prototype rotor will need to undergo rigorous performance validation through dedicated dynamometer testing to verify the full functionality of the printed rotor including structural, magnetic, and thermal behavior under various operating conditions and compared against model predictions. Electrical measurements (power and voltage), temperature measurements, and torque measurements will be compared against model predictions and used to improve materials definition, modeling, and design. This will de-risk all the processes in design, materials, and rotor printing for direct-drive generators at 15-kW scale.

### 4.5.1.2 Medium-Term Goals (2025–2030)

#### Design

- **Design for in situ magnetization and analysis:** Extend the shape optimization tools to include controllability of magnetization direction to leverage the new and emerging in situ magnetization capabilities for magnet printing. These capabilities will significantly improve the flexibility in exploring design freedom with additive manufacturing with the potential to investigate multiple magnet materials with multiple magnetization features.

- **Data-driven design optimization:** Print and test a sample magnet design with multi-angle magnetization feature then use the experimental data for material properties to guide the optimization process and improve the printing process at the same time. Develop advanced simulation tools to predict magnetic field distribution, optimize magnet arrangement, and guide and adjust the magnetic field parameters needed for magnetization. Also focus on efficient cooling strategies for larger rotors to prevent overheating because of weaker magnets. Perform FEAs to assess stress distribution and identify potential weak points considering the measured properties and mechanical strength of printed magnets.
- **Advance multiphysics optimization and LCOE analysis for a large-scale wind generator with a focus on magnets:** Extend the proposed shape optimization study on larger direct-drive generators to increase the understanding and scalability of asymmetric rotor designs with multiple magnet materials and assess their true technoeconomic benefits at a larger scale. Fully integrating structural, thermal, and magnetic optimization can be done more holistically considering modular approaches for machines of larger dimensions.
- **3D modeling and analysis for stator shape-profiled windings:** The laser-based printing processes for conductor printing are expected to significantly advance in the next 5 years, and build envelopes are constantly evolving. Therefore, the coil dimensions needed for large wind turbine generators could be realized in the near future. As higher conductivities are demonstrated, it would be practical to investigate the effect of reduced end-winding lengths with shape-profiled conductors through a dedicated 3D modeling effort for stator windings. The results would help us understand the impact on power density and efficiency.

## Materials

- **Conductors:** Investigate the inclusion of graphene layers in copper printing to achieve 100% IACS conductivity and reduce the risk of oxidation. Develop novel vacuum and nonvacuum methods to produce and handle the larger quantities of copper-graphene composites required to manufacture larger coils (>2 m long). Optimize the alloying ratios to allow for high mechanical strength and ductility in printed coils. Develop post-printing insulation techniques.
- **Gap magnets with higher energy product:** Investigate magnet materials that are free of critical rare earth elements and have a higher starting energy product (>52 MGOe) to achieve up to 30 MGOe energy product. Large-scale extruders (with up to a few tons capacity) will be required to produce homogenous composite pellets of consistent shapes, sizes, and microstructure needed for printing large magnets. At the same time, investigate lower polymer loading with no additives. Also investigate spray pyrolysis techniques to produce spherical particles of magnets of desired size and microstructure suitable for metal additive printing.

## Manufacturing

- **Manufacturing larger segmented magnets for multimegawatt wind turbine generators:** Demonstrate printability of larger magnets with the same level of strength and magnetic anisotropy as traditionally manufactured magnets. Typical dimensions that

could be targeted would be multiple segments of 43 mm (width) x 59 mm (height) x 723 mm (length) to form one magnet for a 15-MW generator. Improve the printing process to ensure consistent material flow and quality throughout the large prints.

- **Scaling up overmolding processes assembling larger magnets:** Scale the overmolding technique that was demonstrated in this project to ensure precise magnet placement. Optimize injection pressure, temperature, and cycle time to improve performance and efficiency.
- **Stator lamination printing:** Pursue thinner laminations with high saturation flux densities ( $>2$  T) by improving the printing processes developed during this project. These include premixing aluminum alloy with Fe<sub>3</sub>Si and printing the laminate via SLM followed by post-annealing; and premixing alumina with Fe<sub>3</sub>Si and printing via BJAT. Optimize print speeds significantly to speed up the printing processes for stator laminations. Fabricate a proof-of-concept segmented, shape-optimized stator for demonstrating the processes for the 15-kW generator.
- **Enhanced alignment techniques:** Develop innovative alignment techniques to achieve even higher degrees of particle alignment in bonded magnets using both ex situ and in situ magnetic field techniques. This could involve exploring magnetic field-assisted alignment methods or surface treatment techniques to minimize particle-particle interactions and optimize magnetic properties. Optimized study of process parameters for use in additive manufacturing done in Section 3 paves the way to develop in situ particle alignment techniques while printing the magnet, eliminating the need to post-align the material.
- **Additive manufacturing of conductor coils for larger generators:** Advance SLM techniques to print shape-profiled windings measuring more than 2 m in axial length. Optimize print parameters substantially optimized to achieve high packing density, reduced porosity, and no oxidation. Increase print speeds to demonstrate faster, cost-effective fabrication.

### **Performance validation of optimized stator design by dynamometer testing**

- Perform dedicated dynamometer testing on the proof-of-concept prototype stator with shape-optimized windings to verify the full functionality of the printed stator along with previously printed rotor. Compare electrical measurements (power and voltage), temperature measurements, and torque measurements against model predictions and use them to improve materials definitions, modeling, and design. This will de-risk all the processes in design, materials, and stator and conductor printing for direct-drive generators at 15-kW scale.

#### **4.5.1.3 Long-Term Goals (2027 and Beyond)**

##### **Design**

- **Detailed design for fully 3D-printed 15-MW prototype:** With different components of the generator individually fabricated to achieve desired functional performances at required dimensions, direct efforts toward the detailed design of larger generators with optimal printed materials.

- **Realize fully printed design and manufacturing:** Develop digital twins of the generator design and manufacturing processes to enable design and manufacturing optimization throughout the life cycle.
- **Achieve autonomous design and optimization:** Use artificial intelligence to automate the design process, from material selection to final product, based on performance requirements and manufacturing constraints.
- **Establish design optimization guidelines:** Use the results from the various efforts on optimization to establish standardized design guidelines based on extensive experimental and simulation data to refine, improve, and accelerate the design process for 3D printing functional magnetic materials.
- **Design for recycling:** Assess the recyclability of printed magnets, electrical steel, and conductors and feed that back into a wholistic process for design and printing that will facilitate easy reuse of printed materials.

## Materials

- **Large-scale soft magnet powder production for 3D printing:** Current methods to produce iron-silicon powders suitable for 3D printing have used the atomization process (3D Printing.com 2024) (melting the iron-silicon alloy and then rapidly cooling it into tiny droplets, which solidify into powder particles), with capacities of up to 200 kg/batch (Imeson 2024). Printing large rotor cores and stator laminations will need significant investments in larger-scale atomization equipment to increase production capacity. Research process optimization to achieve consistent particle size distribution, shape, and chemical composition. This likely will include refining parameters such as gas pressure, temperature, and die design. Larger, more efficient induction furnaces will be needed for increased production capacity while maintaining precise temperature control. Focus efforts on minimizing impurities and oxygen content that will improve powder flowability and packing density. Implement robust quality control measures along with safety measures for powder handling and storage systems for large-scale operations.
- **Materials database:** Create a detailed materials database of printed magnetic, structural, and thermal materials to help inform future design processes and material development for electric machines.

## Multimaterial manufacturing for full-scale generator production

- **Rotor fabrication technology:** Coordinate a collaborative effort involving industry OEMs to leverage large-scale printing platforms, such as the Advanced Casting Cell platform, that are currently under development for cost-effective production of generator rotor at scale on-site. Develop automation processes for magnet placement, overmolding, and inspection to improve quality control and reliability of the final magnet assembly. Develop suitable magnetization fixtures to facilitate post-assembly magnetization.
- **Stator fabrication technology:** Increase the build volumes of the SLM process to print larger dimensions of segmented, modular stator laminations (10 m in diameter). Combine printing of electrical steel with a second insulating material to minimize eddy current losses and eliminate the need for laminating the electrical steel core. This strategy saves capital and time in the lamination process, allowing single-piece solid electrical steel cores, thereby expanding the design possibilities of electric machines. Pursue two main

processes. First, distribute the insulating material evenly within the conducting material. Second, employ a dual-feed additive manufacturing to print alternating layers of conducting and insulating material. Both methods are discussed in Section 3. Develop a layer-by-layer dual-feed approach: Employ existing 3D printers with dual-feed capability to print alternating layers of conducting and insulating material. The first feed could be the conducting material such as silicon steel. The second feed could be insulating material such as alumina or other insulating materials. This process prints insulating layers between conducting layers, eliminating the need for laminations. Also develop processes for inserting printed conductors into stator slots.

- **Fabrication of full-scale prototype:** Use the developed infrastructure and capabilities to fabricate a larger proof-of-concept optimized, lightweight wind turbine generator with reduced critical materials.
- **Testing and certification of 3D printed materials:** Establish certification and testing guidelines for quality control and manufacturing standardization for print part qualification suitable for large-scale generator manufacturing.

#### **Performance validation of optimized, fully 3D printed, large-scale prototype generator**

- Pursue dynamometer testing of large-scale prototype to accurately characterize its power curve, efficiency, and torque output across a wide range of operating speeds and power levels. This will enable fine-tuning of the design and help identify potential performance bottlenecks, facilitate the assessment of generator components under extreme conditions, and ensure the reliability of printed components.

Led by national laboratories, this multi-phased RD&D program is envisioned to be coordinated and timed to support the U.S. offshore wind infrastructure investments led by the U.S. Department of Energy with support from private industry funding and engagement from key stakeholders, including major wind OEMs, for de-risking the supply chain. Strong collaboration among material suppliers and printer manufacturing companies will make it possible to set up advanced generator manufacturing facilities by integrating, step by step, the design and printing processes in the existing generator production lines. This will require a highly skilled workforce, and universities will play a critical role in developing the next generation of designers, materials scientists, and 3D printing professionals.

## References

- 3D Printing.com. n.d. *Elkem Develops Iron-Silicon Powder for Electric Motors*. Accessed June 23, 2024. <https://3dprinting.com/news/elkem-develops-iron-silicon-powder-for-electric-motors/>.
- 3D Printing.com. 2024. *Elkem Introduces Soft Magnetic Powder for 3D Printing Electric Motors*. February 29. <https://3dprinting.com/news/elkem-introduces-soft-magnetic-powder-for-3d-printing-electric-motors/>.
- 3DREMAG. n.d. *3D printing of rare-earth permanent magnets*. Accessed June 23, 2024. <https://3dremag.eu/>.
- Additive drives GmbH. n.d. *Development for the future*. <https://www.additive-drives.de/en/development-for-the-future/>.
- Advanced Materials and Manufacturing Technologies Office (AMMTO). 2024. *Funding Selections: Domestic Large Component Manufacturing to Enable a Clean and Competitive Economy*. <https://www.energy.gov/eere/ammto/funding-selections-domestic-large-component-manufacturing-enable-clean-and-competitive>.
- Africa, Green Building. 2019. *Wind Insustry is Copper Intensive*. September 2. Accessed Jun 30, 2024. <https://www.greenbuildingafrica.co.za/wind-industry-is-copper-intensive/>.
- ALTAIR. 2024. April 30. <https://www.altair.com/flux-applications>.
- ALTAIR. n.d. *Design of experiments with hyperstudy—a study guide*. Accessed February 4, 2024. <https://altairuniversity.com/thank-you-free-ebook-design-of-experiments-with-hyperstudy-a-study-guide/?submissionGuid=0fae75dd-bc8f-4087-8d70-dc3763e0b519>.
- Babuska, T.F., M.A, Johnson, K.L Wilson, S.R. Whetten, J.F. Curry, J.M. Rodelas, C., Lu, P Atkinson, and M. and Krick, B.A. Chandross. 2019. "Achieving High Strength and Ductility in Traditionally Brittle Soft Magnetic Intermetallics Via Additive Manufacturing." *Acta Materialia* 149-157.
- Barter, G.E., L. Sethuraman, P. Bortolotti, J. Keller, and D.A. Torrey. 2023. "Beyond 15 MW: A cost of energy perspective on the next generation of drivetrain technologies for offshore wind turbines." *Applied Energy* 344. Accessed January 08, 2024. doi:<https://doi.org/10.1016/j.apenergy.2023.121272>.
- Bas, J.A., J.A. Calero, and M.J. and Dougan. 2003. "Sintered soft magnetic materials. Properties and applications." *J. Magn. Magn. Mater* 254-255: 391-398. doi:10.1016/S0304-8853(02)00934-4.
- BDT magnets. n.d. *Grain Boundary Diffusion—Conserving HREE in NdFeB Magnets*. <https://idealmagnetsolutions.com/knowledge-base/grain-boundary-diffusion/>.
- Bensalah, A., G. Barakat, and Y. Amara. 2022. "Electrical Generators for Large Wind Turbine: Trends and Challenges." *Energies* 15 (18). doi:<https://doi.org/10.3390/en15186700>.
- Bergey, M. 2021. "2021 Distributed Wind Turbine Competitiveness Improvement Project: Value-Engineered PM Alternator for the Excel 15."
- Bernier, F., M. Ibrahim, M. Mihai, Y. Thomas, and Jean-Michel Lamarre. 2022. "Additive manufacturing of soft and hard magnetic materials used in electrical machines,." *Metal Powder Report* 75 (6): 334-343.
- Busse, M. n.d. *Coils produced by casting*. Fraunhofer Institute for Manufacturing Technology and Advanced Materials IFAM. Accessed July 9, 2024. [https://www.additiv.fraunhofer.de/content/dam/rapidprototyping/en/documents/euromold/szenario1/1\\_coils\\_by\\_casting\\_ifam.pdf](https://www.additiv.fraunhofer.de/content/dam/rapidprototyping/en/documents/euromold/szenario1/1_coils_by_casting_ifam.pdf).

- Cramer, C. L., P. Nandwana, Y. Jiaqiang, S. F. Evans, A.M. Elliott, C.Chinnasamy, and M.P. Paranthaman. 2019. "Binder jet additive manufacturing method to fabricate near net shape crack-free highly dense Fe-6.5 wt.% Si soft magnets." *Heliyon* 5 (11). doi:<https://doi.org/10.1016/j.heliyon.2019.e02804>.
- Damnjanović, A, I Milošev, and N. Kovačević. 2024. "Enhanced mechanical properties and environmental stability of polymer-bonded magnets using three-step surface wet chemical modifications of Nd-Fe-B magnetic powder." *Heliyon*. doi:<https://doi.org/10.1016/j.heliyon.2024.e26024>.
- De Vries, E. 2019. *Exclusive: The inside story of Vestas' ground-breaking new platform*. Accessed June 29, 2024. <https://www.windpowermonthly.com/article/1523702/exclusive-inside-story-vestas-ground-breaking-new-platform>.
- EERE Office of Energy Efficiency & Renewable Energy. 2019. *Distributed Wind Competitiveness Improvement Project Helps Manufacturers Develop, Certify Next-Gen Technologies*. 11 19. <https://www.energy.gov/eere/articles/distributed-wind-competitiveness-improvement-project-helps-manufacturers-develop>.
- Eisenforschung, Max-Planck Institut für. 2021. *Fe-Si steel, transformer steel, electrical steel, soft magnetic, inhibition, Goss texture, microstructure, EBSD, texture*. July 3. <http://www.dierk-raabe.com/electrical-steels-fe-3-si/>.
- EIT Raw Materials. n.d. *SOMA: Lightweight Solutions for E-Mobility by AM of Soft Magnetic Alloys (SOMA)*. <https://eitrawmaterials.eu/project/soma/>.
- Elementum. n.d. <https://www.elementum3d.com/>.
- Europe, Horizon. 2024. *MagNEO: Advanced additively manufactured permanent Magnets for New Energy and MObility Applications*. April 18. doi:<https://doi.org/10.3030/101130095>.
- Faludi, J., M Baumanns, R Hague, and I. Maskery. 2017. "Environmental impacts of selective laser melting: Do printer, powder, or power dominate?" *Journal of Industrial Ecology* S144-S156.
- Ferris, N. 2023. <https://www.energymonitor.ai/renewables/data-insight-the-cost-of-a-wind-turbine-has-increased-by-38-in-two-years/?cf-view&cf-closed>. Energy Monitor. April 25. <https://www.energymonitor.ai/renewables/data-insight-the-cost-of-a-wind-turbine-has-increased-by-38-in-two-years/?cf-view&cf-closed>.
- Fluxtrol. n.d. *Fluxtrol 100 data sheet*. Accessed February 8, 2024.
- Foundry, Hodge. n.d. *Power generation*. Accessed June 23, 2024. <https://www.elyriafoundry.com/hodge-foundry/markets/power-generation/>.
- Gaertner, E., J. Rinker, L. Sethuraman, and and others. 2020. *Definition of the IEA 15-Megawatt Offshore Reference Wind*. National Renewable Energy Laboratory, Golden, CO: National Renewable Energy Laboratory. <https://www.nrel.gov/docs/fy20osti/75698.pdf>.
- Gandha, K., G. Ouyang, S. Gupta, V. Kunc, M. P. Paranthaman, and I. C. Nlebedim. 2019. "Recycling of additively printed rare-earth bonded magnets." *Waste Management* 94-99.
- Gandha, K., I. C. Nlebedim, V. Kunc, E. Lara-Curzio, R. Fredette, and P Paranthaman M. 2020. "Additive manufacturing of highly dense anisotropic Nd-Fe-B bonded magnets." *Scripta Materialia* 183: 91--95. doi:<https://doi.org/10.1016/j.scriptamat.2020.03.012>.
- Gandha, K., M. P. Paranthaman, H. Wang, X. Liu, and I. C. Nlebedim. 2022. "Thermal stability of anisotropic bonded magnets prepared by additive manufacturing." *Journal of the American Ceramic Society*. doi: <https://doi.org/10.1111/jace.18609>.



- Gangl, P. 2018. *Sensitivity-Based Topology and Shape Optimization with Application to Electric Motors*. Vol. 163, in *The IMA Volumes in Mathematics and its Applications*. New York: Springer.
- Global Wind Energy Council and Boston Consulting Group. 2023. "Mission Critical: Building the Global Wind Energy Supply Chain for a 1.5C."
- GreenSpur. n.d. *The Solution to Rare Earth Free Energy*. Accessed April 24, 2024. <https://www.greenspur.co.uk/>.
- Halbig, M.C, and M Singh. 2019. "Additive Manufacturing of Multi-Material Systems for Aerospace Applications." *Materials Science & Technology 2019* . Portland. Accessed July 8, 2024. <https://ntrs.nasa.gov/api/citations/20190032205/downloads/20190032205.pdf>.
- Imeson, N. 2024. *Soft Magnetized Powders for 3D Printing Offer Boost for Electric Motors*. Accessed July 27, 2024. <https://www.asme.org/topics-resources/content/soft-magnetized-powders-for-3d-printing-offer-boost-for-electric-motors>.
- Industry. n.d. *MAGNUM*. Accessed June 19, 2024. [https://assets-global.website-files.com/64f4fa15abdac3bc7545e5fc/65250343899ba8b775c5f165\\_Folder.pdf](https://assets-global.website-files.com/64f4fa15abdac3bc7545e5fc/65250343899ba8b775c5f165_Folder.pdf).
- Iordache, V., and E. Hug. 2009. "Effect of mechanical strains on the magnetic properties of electrical steels." *J Optoelectron Adv Mater*.
- Jaen-Sola, P., and Mc Donald, A. S., and Oterkus, E. 2020. "Design of direct-drive wind turbine electrical generator structures using topology optimization techniques." *Journal of Physics: Conference Series* 1618. doi:<https://doi.org/10.1088/1742-6596/1618/5/052009>.
- JFE Steel, JFE. n.d. *JFE's Electrical Steel sheets*. JFE Steel Corporation. Accessed April 14, 2023. <https://www.jfe-steel.co.jp/en/products/electrical/index.php>.
- KBM, Advanced Materials. n.d. Accessed June 23, 2024. <https://kbmadvanced.com/>.
- Kemp, J.W., K. Mungale, H. Wang, B.C. Sales, U. Vaidya, and M.P. and Paranthaman. 2024. "Novel Method for Overmolding of NdFeB Bonded Magnets Into a 3-D Printed Rotor." *IEEE Transactions on Magnetics* 60 (9). doi:<https://doi.org/10.1109/TMAG.2024.3>.
- Labuschagne, C. J. J., L. Sethuraman, T. Hanley, M.P. Paranthaman, and L.,J Fingersh. 2023. "An Assessment of Additively Manufactured Bonded Permanent Magnets for a Distributed Wind Generator." *2023 IEEE International Electric Machines & Drives Conference (IEMDC)*. San Francisco.
- Lamichhane, T. N., H. Wang, C. Chinnasamy, L. Sethuraman, F. A. List, P. Nandwana, B. Andrews, J. Yan, Z. Gai, and M.P Paranthaman. 2023. "Additively manufactured Fe-3Si stator for high-performance electrical motor." *Submitted*.
- Lamichhane, T.N., L. Sethuraman, A. Dalagan, H. Wang, J. Keller, and Paranthaman, M.P and. 2020. "Additive manufacturing of soft magnets for electrical machines - a review." *Materials Today Physics* 15. doi:10.1016/j.mtphys.2020.100255.
- Laura Lightbody, L, and Courtney Shane. 2023. *Offshore Wind Industry in U.S. Needs Supply Chain Investments*. 12 12. <https://www.pewtrusts.org/en/research-and-analysis/articles/2023/12/12/offshore-wind-industry-in-us-needs-supply-chain-investments>.
- Lee, D. 2022. *Asymmetric Design in Electric motors: Enhancing performance and efficiency*. 11 7. <https://www.emworks.com/blog/motor-design/asymmetric-design-a-way-for-optimizing-electric-motors-performance>.
- Li, L., A. Tirado, B. S. Conner, A. M. Elliott, O. Rios, H. Zhou, and and M. P. Paranthaman. 2017. "Densification and coercivity enhancement of a binder jet printed NdFeB bonded

- magnet through low-melting eutectic alloy infiltration." *Journal of Magnetism and Magnetic Materials* 438: 163--167. doi:<https://doi.org/10.1016/j.jmmm.2017.04.066>.
- Lorenz, F., J. Rudolph, and R. Wemer. 2018. "Design of 3D printed high performance windings for switched reluctance machines." *In Proceedings of the 23rd International Conference on Electrical Machines (ICEM 2018)*. Alexandroupoli, Greece.
- Ma, B.,. 2020. "Advanced Design and Optimization Techniques for Electrical Machines." *PhD Thesis*. University of Technology Sydney.
- MagNEO. n.d. *MagNEO: Advanced additively manufactured permanent magnets for New Energy and MObility Applications*. doi:<https://doi.org/10.3030/101130095>.
- magnets, BDT. n.d. *Grain Boundary Diffusion- Conserving HREE in NdFeB Magnets*. <https://idealmagnetsolutions.com/knowledge-base/grain-boundary-diffusion/>.
- McGarry, C., A. McDonald, and N. and Alotaibi. 2019. "Optimisation of Additively Manufactured Permanent Magnets for Wind Turbine Generators." *2019 IEEE International Electric Machines & Drives Conference (IEMDC)*. San Diego. 656-663. doi:<https://doi.org/10.1109/IEMDC.2019.8785119>.
- McKinsey & Company. 2023. *Renewable-energy development in a net-zero world: Disrupted supply chains*. February 17.
- Mungale, K., T.N. Lamichhane, H. Wang, B.C. Sales, M. P. Paranthaman, and U.K. and Vaidya. 2021. *Materialia* 19: 101167.
- National Renewable Energy Laboratory[NREL]. n.d. *WISDEM: GeneratorSE*. Accessed June 30, 2024. <https://github.com/WISDEM/GeneratorSE/tree/dev>.
- Paranthaman, M. P., B. K. Post, and B. C. Sales. 2024. "Alignment system for magnetic particulate material used for additive manufacturing". U.S. Patent Patent 11,980,939 B2. May 14.
- Paranthaman, M.Parans., Volkan Yildirim, Tej Nath Lamichhane, Benjamin A. Begley, and B. K. Post. 2020. "Additive manufacturing of." *Materials* 13 (15). doi:<https://doi.org/10.3390/ma13153319>.
- Paviot, T. 2022. *pythonocc (7.7.2)*. Edited by Zenodo. Accessed April 25, 2024. <https://github.com/tpaviot/pythonocc-core>.
- Plotkowski, A., J. Pries, F. List, P. Nandawana, B. Stump, K. Carver, and R.R. Dehoff. 2019. "Influence of scan pattern and geometry on the microstructure and soft-magnetic performance of additively manufactured Fe-Si." *Additive Manufacturing* 29. doi:<https://doi.org/10.1016/j.addma.2019.100781>.
- Puukko, P. n.d. *MultiMag project Objectives*. <https://multimag-project.eu/project/#technology>.
- reNEWS.BIZ. 2021. *GE to use 3D printing in Haliade X production*. September 16. <https://renews.biz/72309/ge-to-use-3d-printing-to-speed-up-haliade-x-production/>.
- Riegg, S., J. Reijonen, O. Tosoni, J. Gassmann, L. Schaefer, and O. Gutfleisch. 2021. "Production of Nd-Fe\_B based powders for Laser-Powder-Bed-Fusion - the 3DREMAG Project." Accessed September 5, 2024. <https://underline.io/lecture/22121-production-of-nd-fe-b-based-powders-for-laser-powder-bed-fusion-the-3dremag-project>.
- Sarkar, A., M.A. Somashekara, M. P. Paranthaman, M. Kramer, C. Haase, and I.C. Nlebedim. 2020. "Functionalizing magnet additive manufacturing with in-situ magnetic field source." *Additive Manufacturing*.
- Schwaar, C. 2024. *The Best Large-Format 3D Printers in 2024*. All3dp. March 1. Accessed June 19, 2024. <https://all3dp.com/1/large-format-3d-printer-large-scale/#modix>.

- Selema, A., M. Beretta, M.V. Coppenolle, H. Tiismus, A. Kallaste, M. N. Ibrahim, M. Rombouts, J. Vleugels, L. A.I. Kestens, and P. Sergeant. 2023. "Evaluation of 3D-Printed Magnetic Materials For Additively-Manufactured Electrical Machines." *Journal of Magnetism and Magnetic Materials* 569.  
doi:<https://doi.org/10.1016/j.jmmm.2023.170426>.
- Selema, A., M.N. Ibrahim, and P Sergeant. 2022. "Additively Manufactured Ultralight Shaped-Profile Windings for for HF Electrical Machines and Weight-Sensitive applications." (IEEE TRANSACTIONS ON TRANSPORTATION ELECTRIFICATION) 4313-4324.
- Sethuraman, L., A. Glaws, M. Skinner, and M. P. Paranthaman. 2023. "Advanced permanent magnet generator topologies using multimaterial shape optimization and 3D printing." *12th International Conference on Power Electronics, Machines and Drives (PEMD 2023)*. Brussels, Belgium. 478-485.
- Sethuraman, L., A. Glaws, M. Skinner, and M.P. Paranthaman. 2024. "Advanced multimaterial shape optimization methods as applied to advanced manufacturing of wind turbine generators." *Wind Energy*.
- Sethuraman, L., and G. Vijayakumar. 2022. "'A new shape optimization approach for lightweighting electric machines inspired by additive manufacturing,'" *Joint MMM-Intermag Conference (INTERMAG)*. New Orleans, LA, USA. 1-7.  
doi:<https://doi.org/10.1109/INTERMAG39746.2>.
- Sethuraman, L., G. Vijayakumar, S. Ananthan, and others. 2021. "MADE3D: Enabling the next generation of high-torque density wind generators by additive design and 3D printing. 85, 287–311 (2021)." *Forsch Ingenieurwes*. doi:<https://doi.org/10.1007/s10010-021-00465-y>.
- Sher, Davide. 2021. *ACC, a new era for AM sand casting in Haliade-X offshore wind turbines*. September 16. Accessed January 16, 2024. <https://www.voxelmatters.com/acc-a-new-era-for-am-sand-casting-in-haliade-x-offshore-wind-turbines/>.
- Shields, M., J. Stefek, F. Oteri, S. Maniak, M. Kreider, E. Gill, R. Gould, C. Malvik, S. Tirone, and E. Hines. 2023. "A Supply Chain Road Map for Offshore Wind Energy in the United States."
- Simpson, N, D. J. North, and S.M and Mellor, P.H Collins. 2020. "Additive manufacturing of shaped profile windings for minimal AC loss in electrical machines." 2510-2519.  
doi:<https://doi.org/10.1109/TIA.2020.2975763>.
- Suppan, M., C. Huber, and K. et al. Mathauer. 2022. " In-situ alignment of 3D printed anisotropic hard magnets." *Sci Rep*. doi:<https://doi.org/10.1038/s41598-022-20669-8>.
- Tiismus, H., A. Kallaste, T Vaimann, and A. Rassõlkin. 2022. "State of the art of additively manufactured electromagnetic materials for topology optimized electrical machines." *Additive Manufacturing* 55.
- U.S. DOE. 2023. "Notice of Final Determination on 2023 DOE Critical Materials List." <https://www.energy.gov/sites/default/files/2023-07/preprint-frn-2023-critical-materials-list.pdf>.
- Voxeljet. n.d. *Develop world's largest sand binder jetting 3D printer*. Accessed June 23, 2024. <https://www.voxeljet.com/press-releases/develop-worlds-largest-sand-binder-jetting-3d-printer/>.
- Vries, Eize de. 2023. *Stator segments: the golden triad of modularity, scalability and simplicity*. July 12. <https://www.windpowermonthly.com/article/1829671/stator-segments-golden-triad-modularity-scalability-simplicity>.

- VTT Research, Center. 2021. *3DREMAG : 3D printing of rare-earth permanent magnets*. 03 25. <https://3dremag.eu>.
- Wang, H, T.N. Lamichhane, and M. P. Paranthaman. 2022. "Review of additive manufacturing of permanent magnets for electrical machines: A prospective on wind turbine." *Materials Today Physics* 100675. doi:10.1016/j.mtphys.2022.100675.
- Willard, M., and K. Kniping. 2012. "Nanocrystalline Soft Magnetic Materials at High Temperatures: A Perspective." *Scripta Materialia* 554-559.
- Williams, R., F. Zhao, and J. Lee. 2022. "Global Offshore Wind Report 2022." Accessed December 2023. <https://gwec.net/wp-content/uploads/2022/06/GWEC-Global-Offshore-Wind-Report-2022.pdf>.
- Wood McKenzie. 2019. *Global wind turbine fleet to consume over 5.5Mt of copper by 2028*. October 02. <https://www.woodmac.com/press-releases/global-wind-turbine-fleet-to-consume-over-5.5mt-of-copper-by-2028/>.
- Wooley, D., and J Matos. 2023. *Offshore Wind Supply Chain Development and Investment Analysis*. University of California, Berkeley.
- YASKAWA. 2024. *Wind Electrical Drivetrains*. June 30. [https://www2.theswitch.com/1/500181/2020-10-05/47fbwb/500181/1601914679gTsagM5W/Wind\\_brochure.pdf](https://www2.theswitch.com/1/500181/2020-10-05/47fbwb/500181/1601914679gTsagM5W/Wind_brochure.pdf).